Powder atomic layer deposition for precise interface engineering in thermoelectric materials

Von der Fakultät Maschinenwesen der Technischen Universität Dresden
zur Erlangung des akademischen Grades
Doktoringenieur (Dr.-Ing.)
angenommene

Dissertation

M.Sc. Shiyang He
geb. am: 03.08.1995 in Henan, China

Tag der Einreichung:	20.7.2023
Tag der Verteidigung:	1.12.2023
Gutachter:	Prof. Dr. Kornelius Nielsch Prof. Dr. Christophe Detavernier

Shiyang He

Powder atomic layer deposition for precise interface engineering in thermoelectric materials

TECHNISCHE UNIVERSITÄT DRESDEN

Leibniz Institute for Solid State and Materials Research Dresden

念奴娇·过洞庭

宋·张孝祥

洞庭青草，近中秋，更无一点风色。
玉鉴琼田三万顷，着我扁舟一叶。
素月分辉，明河共影，表里俱澄澈。
悠然心会，妙处难与君说。

应念岭表经年，孤光自照，肝胆皆冰雪。
短发萧骚襟袖冷，稳泛沧溟空阔。
尽挹西江，细斟北斗，万象为宾客。
扣舷独啸，不知今夕何夕。

Niannujiao Theme: Crossing Lake Dongting

Song Dynasty· Zhang Xiaoxiang

The green grass at Lake Dongting,
when it's near Mid-Autumn Festival,
shows no effect of blowing wind.
In a spacious field under jade-like moon,
only one little boat of mine is here.
The silvery moon showers its light.
Milky way aside is complementing.
Sky high up and lake below are limpid.
In carefree mood, I can appreciate these.
Sharing such wonders in words is hard.

I recall years in areas south of the mountains,
the moon has been shining all alone by itself.
My integrity has been untainted like icy snow.
With hair thinning and clothes not warm enough,
I calmly drift boat in this vast stretch of waves.
Let me scoop out all the water in westside river,
and pour it out slowly from the Big Dipper jug,
Then I invite all things of Nature to be guests.
Beating time aboard and crooning alone,
I've lost track of what day of the year it is now.

Abstract

Manipulating grain boundaries to pursue favorable physical or chemical properties is essential in materials design. As a prominent candidate for direct heat-to-electricity conversion applications, the performance of thermoelectric (TE) materials is strongly affected by the chemical compositions and physical properties of grain boundaries. As a layer-by-layer deposition technique, atomic layer deposition (ALD) is recognized as a unique method for depositing highly uniform films in a controlled manner. This gives us fresh insight into applying ALD approaches on a powder surface to realize a uniform coating on each particle with a specific thickness and composition of ALD layers. Powder ALD also provides a new way to construct complex layer structures, such as multiple layers, with precision layer composition control. In this thesis, a strategy of interface modification based on powder ALD is introduced in various TE materials (Bi, CuNi, and Zn_4Sb_3) to accurately control and modify the phase boundaries by oxide layer coating.

For elemental bismuth, as the first discovered TE material, ultrathin layers of Al_2O_3, TiO_2, and ZnO are typically deposited on powders via 1–20 cycles. All of the oxide layers significantly alter the microstructure and suppress grain growth. The hierarchical interface modifications aid the formation of an energy barrier by the oxide layer, resulting in a substantial increase in the Seebeck coefficient that is superior to that of most pure polycrystalline metals. Conversely, taking advantage of strong electron and phonon scattering, an exceptionally large decrease in thermal conductivity is obtained. A maximum figure of merit (zT) of 0.15 at 393 K and an average zT of 0.14 at 300–453 K were achieved in 5 cycles of Al_2O_3-coated Bi. Additionally, newly developed Sb_2O_5 thin films produced from $SbCl_5$ and H_2O_2 were formed on the surfaces of Bi powders. Because of the high Kapitza resistance generated by Sb_2O_5 layers on Bi particles, a substantial decrease in total thermal conductivity from 7.8 to 5.7 W/m·K was obtained with just 5 cycles of Sb_2O_5 layer deposition and a 16% reduction in lattice thermal conductivity. Because of strong phonon scattering, the maximum zT values increased by approximately 12% and were relocated to 423 K.

For CuNi, first, single-type ZnO and Al_2O_3 layers were deposited on the surface of CuNi powder, and their effect on the TE performance of the bulk was thoroughly investigated. The enhancement of the Seebeck coefficient, caused by the energy filtering effect, compensates for the electrical conductivity deterioration due to the low electrical conductivity of the oxide layers. Furthermore, the oxide layers may significantly

increase the phonon scattering. Therefore, to reduce the resistance of phase boundaries, a multiple-layer structure was constructed by inserting Al_2O_3 into ZnO. Atom probe tomography shows that the Al atoms diffused into ZnO and realized the doping effect after pressing. Al diffusion has great potential to increase the electrical conductivity of coating layers. In comparison to pure CuNi, zT increased by 128% as a result of the decrease in resistance and stronger phonon scattering at the phase boundaries.

The oxide layer coating not only yields a significant enhancement in the TE performance but also behaves as an energy barrier to suppress the migration of Zn ions in Zn_4Sb_3. With increasing ZnO layer cycle numbers, the layer thickness can be precisely tuned, and Zn migration can be effectively blocked with an oxide barrier. In the 100 cycle ZnO-coated sample, there was little deterioration of the power factor due to increasing resistivity. However, the decrease in total thermal conductivity results in similar zT values compared with pure Zn_4Sb_3, indicating that the TE performance of the 100 cycle ZnO layer-coated sample did not degrade. Additionally, 100 cycles of ZnO layers result in significantly enhanced thermal stability and effectively block Zn atom movement after 10 thermal cycling tests. The study demonstrates that ALD-based interface modification is a versatile method for decoupling TE parameters and precisely modifying phase boundaries, which is practical for other TE materials.

Kurzfassung

Die Manipulation von Korngrenzen zur Erzielung günstiger physikalischer oder chemischer Eigenschaften ist bei der Materialentwicklung von entscheidender Bedeutung. Als prominenter Kandidat für Anwendungen zur direkten Umwandlung von Wärme in Elektrizität wird die Leistung thermoelektrischer (TE) Materialien stark von der chemischen Zusammensetzung und den physikalischen Eigenschaften der Korngrenzen beeinflusst. Als schichtweise Abscheidungstechnik gilt die Atomlagenabscheidung (ALD) als einzigartige Methode zur kontrollierten Abscheidung sehr gleichmäßiger Filme. Dies gibt uns neue Einblicke in die Anwendung von ALD-Ansätzen auf einer Pulveroberfläche, um auf jedem Partikel eine gleichmäßige Beschichtung mit einer spezifischen Dicke und Zusammensetzung der ALD-Schichten zu erzielen. Pulver-ALD bietet auch eine neue Möglichkeit, komplexe Schichtstrukturen, wie z. B. mehrere Schichten, mit präziser Steuerung der Schichtzusammensetzung aufzubauen. In dieser Arbeit wird eine Strategie zur Grenzflächenmodifikation auf Basis von Pulver-ALD in verschiedenen TE-Materialien (Bi, CuNi und Zn_4Sb_3) eingeführt, um die Phasengrenzen durch Oxidschichtbeschichtung genau zu steuern und zu modifizieren.

Bei elementarem Wismut, dem ersten entdeckten TE-Material, werden typischerweise ultradünne Schichten aus Al_2O_3, TiO_2 und ZnO über 1–20 Zyklen auf Pulvern abgeschieden. Alle Oxidschichten verändern die Mikrostruktur erheblich und unterdrücken das Kornwachstum. Die hierarchischen Grenzflächenmodifikationen unterstützen die Bildung einer Energiebarriere durch die Oxidschicht, was zu einem erheblichen Anstieg des Seebeck-Koeffizienten führt, der dem der meisten reinen polykristallinen Metalle überlegen ist. Umgekehrt wird unter Ausnutzung der starken Elektronen- und Phononenstreuung eine außergewöhnlich starke Verringerung der Wärmeleitfähigkeit erzielt. In 5 Zyklen von Al_2O_3-beschichtetem Bi wurde ein maximaler Gütefaktor (zT) von 0,15 bei 393 K und ein durchschnittlicher zT von 0,14 bei 300–453 K erreicht. Darüber hinaus wurden neu entwickelte Sb_2O_5-Dünnfilme aus $SbCl_5$ und H_2O_2 auf den Oberflächen von Bi-Pulvern gebildet. Aufgrund des hohen Kapitza-Widerstands, der durch Sb_2O_5-Schichten auf Bi-Partikeln erzeugt wird, wurde mit nur 5 Zyklen der Sb_2O_5-Schichtabscheidung eine erhebliche Verringerung der Gesamtwärmeleitfähigkeit von 7,8 auf 5,7 W/m·K und eine 16-prozentige Verringerung der Gitterwärmeleitfähigkeit erzielt. Aufgrund der starken Phononenstreuung stiegen die maximalen zT-Werte um etwa 12% und wurden auf 423 K verschoben.

Für CuNi wurden zunächst einzelne ZnO- und Al_2O_3-Schichten auf der Oberfläche von CuNi-Pulver abgeschieden und ihre Auswirkung auf die TE-Leistung der gepressten Probe gründlich untersucht. Die durch den Energiefiltereffekt verursachte Erhöhung des Seebeck-Koeffizienten gleicht die Verschlechterung der elektrischen Leitfähigkeit aufgrund der geringen elektrischen Leitfähigkeit der Oxidschichten aus. Darüber hinaus können die Oxidschichten die Phononenstreuung deutlich erhöhen. Um den Widerstand der Phasengrenzen zu verringern, wurde daher eine Mehrschichtstruktur durch Einfügen von Al_2O_3 in ZnO konstruiert. Die Atomsondentomographie zeigt, dass die Al-Atome in ZnO diffundierten und nach dem Pressen den Dotierungseffekt realisierten. Die Al-Diffusion hat ein großes Potenzial, die elektrische Leitfähigkeit von Beschichtungsschichten zu erhöhen. Im Vergleich zu reinem CuNi erhöhte sich zT aufgrund des geringeren Widerstands und einer stärkeren Phononenstreuung an den Phasengrenzen um 128%.

Die Oxidschichtbeschichtung führt nicht nur zu einer deutlichen Verbesserung der TE-Leistung, sondern fungiert auch als Energiebarriere, um die Migration von Zn-Ionen in Zn_4Sb_3 zu unterdrücken. Mit steigenden Zyklenzahlen der ZnO-Schicht kann die Schichtdicke präzise abgestimmt und die Zn-Migration mit einer Oxidbarriere effektiv blockiert werden. Bei der mit 100 Zyklen ZnO beschichteten Probe kam es aufgrund des zunehmenden spezifischen Widerstands zu einer geringen Verschlechterung des Leistungsfaktors. Die Abnahme der Gesamtwärmeleitfähigkeit führt jedoch zu ähnlichen zT-Werten im Vergleich zu reinem Zn_4Sb_3, was darauf hindeutet, dass sich die TE-Leistung der mit einer ZnO-Schicht beschichteten 100-Zyklen-Probe nicht verschlechtert hat. Darüber hinaus führen 100 Zyklen von ZnO-Schichten zu einer deutlich verbesserten thermischen Stabilität und blockieren effektiv die Bewegung von Zn-Atomen nach 10 thermischen Zyklentests. Die Studie zeigt, dass die ALD-basierte Grenzflächenmodifikation eine vielseitige Methode zur Entkopplung von TE-Parametern und zur präzisen Modifikation von Phasengrenzen ist, die für andere TE-Materialien praktisch ist.

Contents

1

Chapter 1 Introduction

Thermoelectric (TE) materials are promising candidates for direct thermal-to-electrical energy conversion applications and sustainable energy solutions owing to their combined heat and electricity attributes.

The energy conversion efficiency (η) of TE materials in conventional TE generators is determined by the dimensionless figure of merit (zT)[1,2], which can be presented by $zT=S^2\sigma\varkappa_{tot}^{-1}T$ (S: Seebeck coefficient, σ: electrical conductivity, $\varkappa_{tot}$: total thermal conductivity, T: absolute temperature). The key challenge for enhancing the performance of TE materials is establishing a balance between electrical and thermal properties. Although enhancing the temperature gradient (T_h-T_c) benefits the improvement of the conversion efficiency, different TE materials exhibit optimum TE performance in different temperature ranges; therefore, the desired TE materials should be selected within a given temperature range. To realize higher η values, higher zT values are generally required for various temperature ranges. Overall, TE materials with zT values greater than 1 are preferred for TE generators. If a TE material with a zT value exceeding 3 is used, then the corresponding η would be high enough to replace traditional power generators/refrigerators with TE generators[3].

However, optimizing TE performance is a relatively complex task due to the intercorrelation between the transport parameters[4], making obtaining a zT value of 3 challenging. Notably, the S, σ, and $\varkappa_{tot}$ parameters are intercorrelated. Therefore, decoupling PF and $\varkappa$ is still a challenge in the TE field. In recent decades, numerous strategies have been applied to investigate the rational design and development of TE materials. The main concepts for optimizing the zT value converge toward two approaches: i) enhancing the PF in terms of electrical properties by point-defect engineering[5–7], band engineering[8–10], texturing[11–13], and energy filtering[14–16]; and ii) decreasing the independent lattice thermal conductivity via nanostructuring[17–19], phonon engineering[20–22], interfacial modifications[23–25], or searching for new TE materials with intrinsically low thermal conductivity[26–28].

Manipulating the grain boundaries to pursue favorable transport properties is an essential issue in the design of TE materials[29,30]. The chemical compositions and physical properties at the grain boundaries have a substantial effect on the performance of the materials made with them. A single phase of TE materials usually does not favor all requirements with respect to properties[2,31]. Thus, the introduction of new materials

into the matrix to form multiphase composites is another prominent approach attracting major scientific interest[32–34]. In TE materials, two approaches[35] are introduced to construct multiphase composites: i) forming precipitates under nonequilibrium conditions during the melting and solidification of the parent compound[36,37] and ii) artificial second phase additions by dispersing the nanoparticles or forming a core-shell structure[38,39]. The approaches mentioned above enable the combination of different dispersions and matrices in such a way that two or more constituents can be gathered in one system, endowing the final system with their advantageous characteristics[40–43]. However, to achieve better functional performance, the composition and content of the second phase must be precisely controlled, even at the atomic scale, which is challenging to achieve using existing approaches[35].

Atomic layer deposition (ALD) is recognized as a unique layer-by-layer deposition technique for creating highly homogenous films in a controlled manner[44,45]. Unlike chemical vapor deposition (CVD), the precursors in ALD are always separated and alternatively pulsed into reactors to achieve layer-by-layer growth[46,47]. Because of the self-limiting nature of the chemical reactions in an ALD process, not only can film thickness be controlled down to the atomic level, allowing for the deposition of extremely thin films (even only a few atoms thick)[39,48] but also a highly conformal coating can be expected, as the deposition process is restricted to the surface of the substrate, rather than building up layers on top of one another[38,49]. Furthermore, the separated pulsing process allows for the formation of multiple-layered structures, which can be used to accurately tune the compositions of films[50]. These characteristics enable ALD to precisely deposit a specific thickness of selected materials on the surface of TE powders to manipulate the transport properties of the substrate material. Powder ALD has already demonstrated unprecedented success in improving the TE performance of various TE materials, such as Bi[51,52], Bi_2Te_3 alloys[53,54], $CoSb_3$[55], and ZrNiSn-based materials[56]. Different oxides, such as Al_2O_3[52], TiO_2[57], and ZnO[55], are mainly used as coating layers due to their developed deposition process and good thermal stability.

The research carried out in this thesis can be categorized into two distinct fields of contemporary scientific interest: i) powder ALD and ii) TE materials. The main concept of the thesis is not only to develop new materials and precision composition control by ALD but also to explore the effect of ALD coating layers on TE performance.

This thesis implements the ALD technique as a novel approach for grain boundary engineering in TE materials with the aim (Figure 1-1) of manipulating the charge carrier/phonon/ion transport to realize the following:

i) The enhancement of S by the energy filtering effect to maintain or increase $S^2\sigma$.

ii) Suppressing lattice thermal conductivity ($\varkappa_{lat}$) by stronger phonon scattering.

ii) Blocking ion migration by constructing an energy barrier.

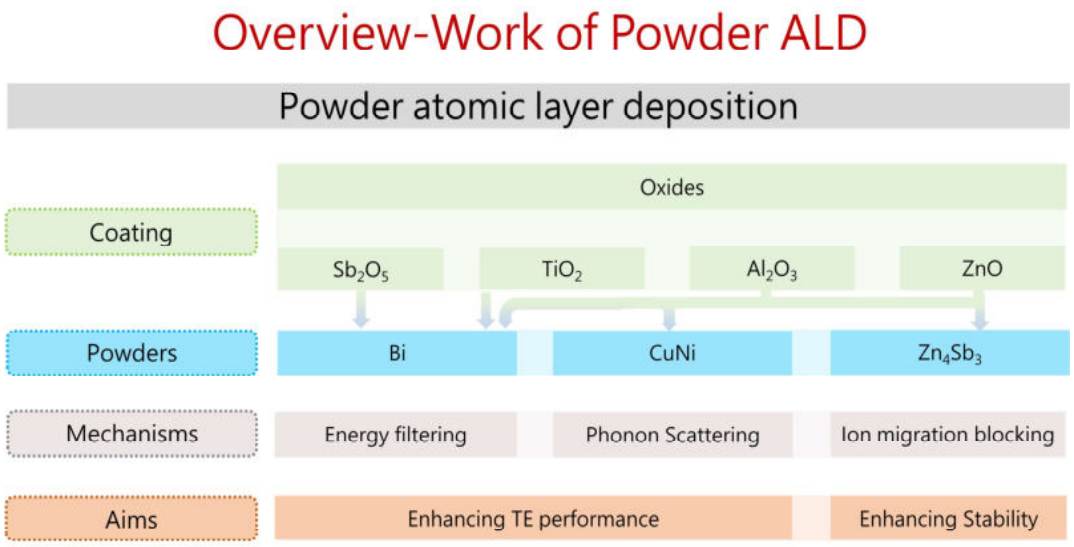

Figure 1-1 *The overview of powder ALD in this thesis.*

The state of the art of interface modification in the TE field was summarized in our review publication as an important part of Chapter 2. The powder ALD works in this thesis have led to four original research papers, which are contained in Chapters 4–6. The following list summarizes the contents of each paper and the advancements made therein:

- Review: *Current State-of-the-Art in the Interface/Surface Modification of Thermoelectric Materials (**Advanced Energy Materials**, 11(37), 2101877, 2021)*

Extensive efforts to improve the TE efficiency of single-/multiphase composites comprising nano/microscale second phases are being made. The artificial decoration of second phases into the thermoelectric matrix of multiphase composites, which is distinguished from the second-phase precipitation occurring during the thermally equilibrated synthesis of TE materials, can effectively enhance their performance. Theoretically, the interfacial manipulation of phase boundaries can be extended to a wide range of materials. High interface densities decrease the thermal conductivity when nano/microscale grain boundaries are obtained, and certain electronic structure modifications may increase the power factor of TE materials. Based on the distribution of the second phase at the interface boundaries, the strategies can be divided into discontinuous and continuous interfacial modifications. The discontinuous interfacial modifications section in this review discusses five parts chosen according to their dispersion forms, including metals, oxides, semiconductors, carbonic compounds, and MXenes. Alternatively, gas- and solution-phase process techniques are adopted for

realizing continuous surface changes, such as changes in the core-shell structure. This review offers a detailed analysis of the current state of the art in the field while identifying possibilities and obstacles for improving the performance of TE materials.

- Paper I: *Effect of powder ALD interface modification on the thermoelectric performance of bismuth (**Advanced Materials Technologies**, 7(5), 2100953, 2022)*

In this paper, single kinds of layers of Al_2O_3, TiO_2, and ZnO are typically deposited on Bi powder for 1–20 cycles. All of the oxide layers significantly alter the microstructure and suppress grain growth. These hierarchical interface modifications aid the formation of an energy barrier by the oxide layer, resulting in a substantial increase in the S that is superior to that of most pure polycrystalline metals. Conversely, taking advantage of strong electron and phonon scattering, an exceptionally large decrease in thermal conductivity is obtained. A maximum figure of merit, zT, of 0.15 at 393 K and an average zT of 0.14 at 300–453 K were achieved in 5 cycles of Al_2O_3-coated Bi.

- Paper II: *Surface Modification of Bismuth by ALD of Antimony Oxide for Suppressing Lattice Thermal Conductivity (**ACS Applied Energy Materials**, 5(4), 4041-4046, 2022)*

Using the powder ALD method, newly developed Sb_2O_5 thin films produced from $SbCl_5$ and H_2O_2 were formed on the surfaces of Bi powders. Because of the high Kapitza resistance generated by Sb_2O_5 layers on Bi particles, a substantial decrease in $\varkappa_{tot}$ from 7.8 to 5.7 W/m·K was obtained with just 5 cycles of Sb_2O_5 layer deposition and a 16% reduction in $\varkappa_{lat}$. Because of strong phonon scattering, the maximum zT values increased by approximately 12% and were relocated to 423 K.

- Paper III: *Precision interface engineering by ALD in CuNi alloys toward high thermoelectric performance (**Advanced Functional Materials** (Under reviewed))*

In this article, multilayers with sandwich-like structures ($ZnO/Al_2O_3/ZnO$) were constructed on every single particle to reduce the electrical resistance at the boundaries. In the high-cycle number coating ($>$ 50 cycles), this multiple-layer coated structure sustained the intrinsic high $S^2\sigma$ while also yielding a significant reduction in thermal conductivity. In 44 cycles ZnO/11 cycles Al_2O_3/44 cycles ZnO multilayer-coated samples, a maximum zT of 0.22 was achieved at 673 K. Due to decoupling TE parameters by ALD, the zT value increased 128% when compared to pristine CuNi and is nearly as high as that previously reported.

- Paper IV: *Blocking ion migration in Zn_4Sb_3 by powder ALD (under preparation)*

Herein, a powder ALD strategy is introduced to accurately control and modify the grain boundaries of Zn_4Sb_3, which could block the migration of Zn ions and enhance the thermal stability of the compound during performance. To demonstrate the effectiveness of this strategy, ultrathin interlayers of ZnO (typically 10–100 cycles) are uniformly deposited on the surface of Zn_4Sb_3 particles. With ZnO coating layers, these hierarchical interface modifications contribute to the creation of a barrier for charge carriers and ions. Although there is little deterioration in electrical conductivity, the $\varkappa_{tot}$ suppression for 100 cycles of ZnO-coated samples compensated for the loss and resulted in almost the same zT values as that of the pristine sample. Additionally, the 100-cycle ZnO-coated samples show excellent thermal stability, indicating an effective blocking effect on Zn atom migration.

The research results are based on a wide array of experimental characterization methods, some of which might be unfamiliar to the reader. For this purpose, Chapter 3 provides short introductions to the theory behind (and the practical use of) each technique. Finally, Chapter 7 provides general conclusions and outlooks that can be drawn from those works.

2

Chapter 2 Background and motivation

This chapter begins with an introduction to the fundamental knowledge of TE materials and the background of ALD. Then, as an important subfield of ALD, powder ALD method used to uniformly deposit layers on the surfaces of the powders is generally introduced and presented. After that, the state-of-the-art of powder ALD to modify the grain boundaries in TE materials is summarized in the following section. Finally, the current development of three representative TE materials (Bi, CuNi, and Zn_4Sb_3) studied in this thesis is introduced and discussed.

The interface/surface modification of thermoelectric materials has been summarized and published in the following publication:

Shiyang He, Sebastian Lehmann, Amin Bahrami*, Kornelius Nielsch* (2021). Current State-of-the-art in the Interface/surface Modification of Thermoelectric Materials. ***Advanced Energy Materials***, 11(37), 2101877. (Chapter 2.2 and 2.4)

2.1 Fundamental knowledge of thermoelectricity

2.1.1 Thermoelectric effects

The TE effects of energy conversion can be mainly categorized into three types: i) the Seebeck effect, ii) the Peltier effect, and iii) the Thomson effect. The above three physical effects constitute a complete description of the direct conversion of heat and electricity[58].

i) Seebeck effect

The Seebeck effect can be tracked back 200 years and was first discovered by German physicist Thomas Johann Seebeck[58]. As shown in Figure 2-1, when the temperature difference (T_{hot}-T_{cold}) was applied to the joint of materials A and B, a voltage U_{AB} could be generated, which can be expressed by Equation 2-1:

$$U_{AB}=S_{AB}(T_{hot}-T_{cold}) \quad (2\text{-}1)$$

In Equation 2-1, S_{AB} is the differential Seebeck coefficient between materials A and B, and the unit is μV/K. Additionally, the direction of the potential difference U_{AB} is determined by the direction of the temperature gradient. For instance, when the current generated in conductor A is transmitted from the higher to the lower temperature, S_{AB} is defined to be positive.

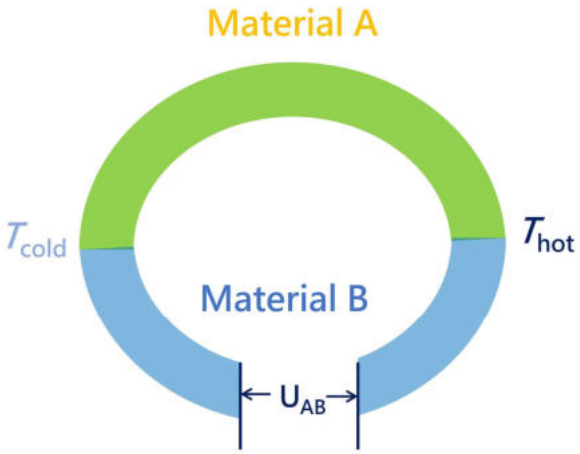

Figure 2-1 *Schematic diagram of the Seebeck effect*[58].

As described in the process of voltage induced by the temperature difference, the absolute Seebeck coefficient for the single materials can be defined by Equation 2-2:

$$S = -\lim_{\Delta T \to 0} \frac{U}{\Delta T} \tag{2-2}$$

Thus, the relationship between the absolute Seebeck coefficient for the single materials (A and B) and the differential Seebeck coefficient can be expressed as

$$S_{AB} = S_A - S_B \tag{2-3}$$

It is noted that the absolute Seebeck coefficient for a single kind of material is independent of the direction of the temperature difference and is only related to the nature of the material.

ii) Peltier effect

The Peltier effect refers to the direct generation of a temperature difference by current, which can be recognized as the reverse process of the Seebeck effect. After connecting two different materials (C and D) and applying current, a temperature difference is formed between the two joints, as shown in Figure 2-2.

The relation between the heat flow (Q) generated by the Peltier effect and the current (I) can be expressed as

$$Q=\pi_{CD}I \tag{2-4}$$

where π_{CD} is the differential Peltier coefficient between materials C and D.

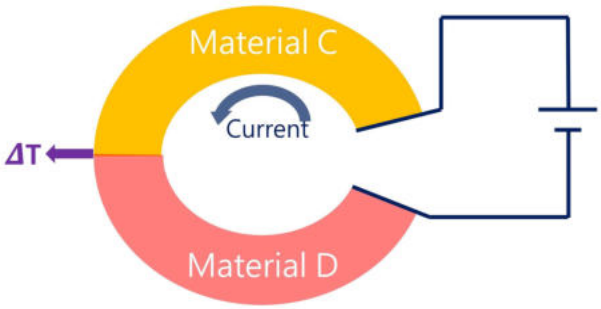

Figure 2-2 *Schematic diagrams of the Peltier effect*[58].

Similarly, the Peltier coefficient (π) is directional and depends on the current direction. The relationship between the absolute Peltier coefficient for the single materials (C or D) and the differential Peltier coefficient can be expressed as

$$\pi_{CD}=\pi_C-\pi_D \tag{2-5}$$

The Peltier effect and Seebeck effect are connected, and the Peltier coefficient π is related to the Seebeck coefficient S by the following equation:

$$\pi=S\times T \tag{2-6}$$

iii) Thomson effect

The Seebeck effect and Peltier effect often occur in joints composed of two different materials. However, the Thomson effect occurs in one specific homogeneous material, and the Thomson coefficient (β) is related to heat flow and current. If the current (I) and temperature difference (ΔT) are simultaneously applied, then the inverse of the evolution or absorption of heat occurs in addition to Joule heating caused by its resistance. The heat current can be positive or negative and is linear with respect to the electrical current and the temperature gradient, which can be expressed as

$$Q=\beta\Delta TI \tag{2-7}$$

When the current is in the same direction as the temperature gradient, β is positive. Notably, the contribution of the Thomson effect in whole energy conversion is small and is often ignored compared with the other two TE effects.

iv) The efficiency of the device and zT values

Energy conversion efficiency plays an important role in practical applications for replacing traditional generators with TE devices[59]. The primary goal of achieving large-

scale commercial applications of TE devices is to improve the energy conversion efficiency of the devices. The typical π-shape TE generator[60] is composed of *n*- and *p*-type material legs, as shown in Figure 2-3(a). The conversion efficiency of the TE device can be obtained as

$$\eta=\frac{P}{Q_{\mathrm{h}}} \tag{2-8}$$

where η is the conversion efficiency, P is the output power, and Q_{h} is the heat absorbed at the hot side. Here, we omit the derivation process[36,61,62] of the intermediate from Equation (2-8), and the details can be found in the references[59]. The efficiency η of the TE generator can be expressed as

$$\eta=\frac{P}{Q_{\mathrm{h}}}=\frac{I^2R_{\mathrm{ex}}}{S_{\mathrm{np}}T_{\mathrm{h}}I-\frac{I^2R_{\mathrm{np}}}{2}+\varkappa(T_{\mathrm{hot}}-T_{\mathrm{cold}})}=\frac{S_{\mathrm{np}}^2(T_{\mathrm{hot}}-T_{\mathrm{cold}})R_{\mathrm{ex}}}{\frac{S_{\mathrm{np}}^2(T_{\mathrm{hot}}-T_{\mathrm{cold}})R_{\mathrm{np}}}{2}+S_{\mathrm{np}}^2T_{\mathrm{hot}}R_{\mathrm{ex}}+\varkappa(T_{\mathrm{hot}}-T_{\mathrm{cold}})} \tag{2-9}$$

where I, R_{ex}, R_{np}, S_{np}, and $\varkappa$ are the current in the circuit, external resistance, total resistance of *n*-/*p*-type legs, differential Seebeck coefficient of *n*-/*p*-type legs, and total thermal conductivity of legs, respectively. We can further define $z=\frac{\sigma S_{\mathrm{np}}^2}{\varkappa}$, $\sigma=\frac{A_{\mathrm{n}}}{l_{\mathrm{n}}\sigma_{\mathrm{n}}}+\frac{A_{\mathrm{p}}}{l_{\mathrm{p}}\sigma_{\mathrm{p}}}$, and $\varkappa=\frac{A_{\mathrm{n}}}{l_{\mathrm{n}}}\varkappa_{\mathrm{n}}+\frac{A_{\mathrm{p}}}{l_{\mathrm{p}}}\varkappa_{\mathrm{p}}$ (σ, $\varkappa$, A, and l are the electrical conductivity, thermal conductivity, cross-sectional area, and effective length of *n*-/*p*-type legs, respectively). Thus, Equation (2-9) can be simplified as

$$\eta=\frac{T_{\mathrm{hot}}-T_{\mathrm{cold}}}{T_{\mathrm{hot}}}\ \frac{R_{\mathrm{ex}}/R_{\mathrm{np}}}{(1+R_{\mathrm{ex}}/R_{\mathrm{np}})-\frac{T_{\mathrm{hot}}-T_{\mathrm{cold}}}{2T_{\mathrm{hot}}}+\frac{(1+R_{\mathrm{ex}}/R_{\mathrm{np}})^2}{zT_{\mathrm{hot}}}} \tag{2-10}$$

When $\frac{R_{\mathrm{ex}}}{R_{\mathrm{np}}}=\sqrt{1+z\overline{T}}$ ($\overline{T}$ is the average temperature over the legs), the maximum efficiency $\eta_{\max}$ of the TE generator can be expressed as

$$\eta_{\max}=\frac{T_{\mathrm{hot}}-T_{\mathrm{cold}}}{T_{\mathrm{hot}}}\ \frac{\sqrt{1+z\overline{T}}-1}{\sqrt{1+z\overline{T}}+T_{\mathrm{cold}}/T_{\mathrm{hot}}} \tag{2-11}$$

From Equation (2-11), $\eta_{\max}$ is only related to the zT value and the temperature difference applied on the device.

Additionally, the zT value is dimensionless and determined by the material itself, which is called the figure of merit and is expressed as

$$zT=\frac{\sigma S^2}{\varkappa}T \tag{2-12}$$

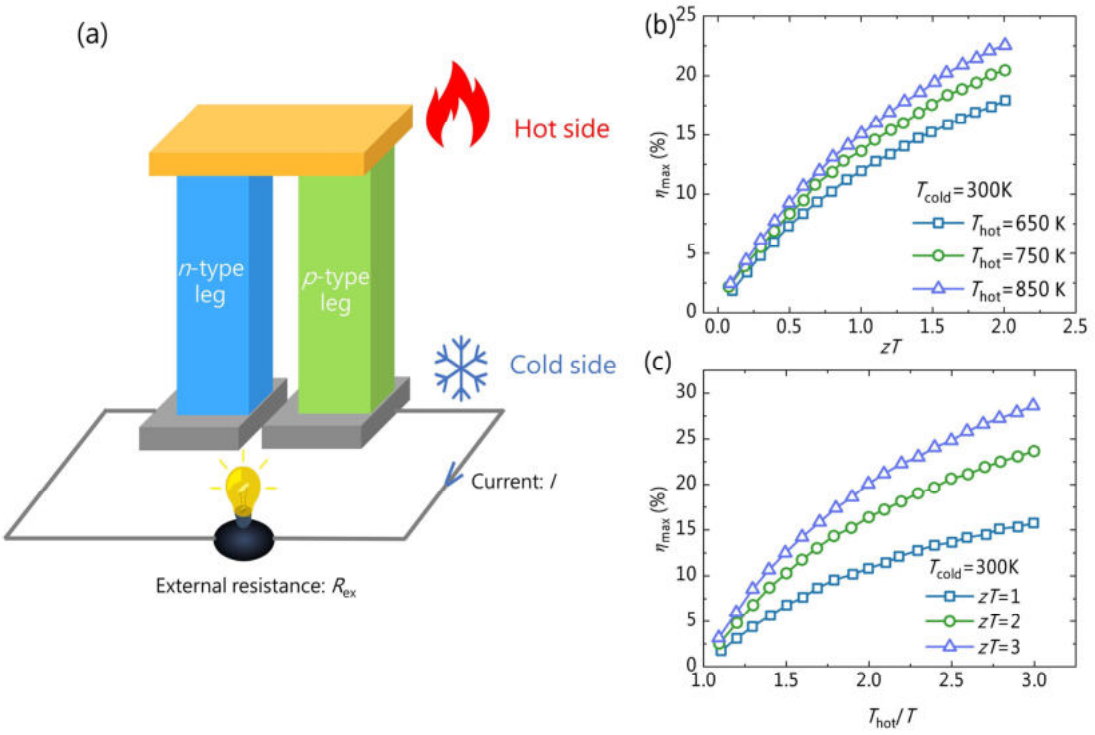

Figure 2-3 *(a) Schematic diagram of a π-shape TE generator. (b) The efficiency of the TE device and average zT value at various hot-side temperatures*[58]*. (c) The efficiency of TE devices and temperature difference at various zT values*[58]*.*

It should be noted that the zT values are used for evaluate the TE performance of materials in different temperature ranges. From Equation (2-11), the larger the zT value is, the higher η is. Figure 2-3(b) shows the relationship between the efficiency of the TE device and the zT value at various T_{hot} and ΔT values when that of the cold side is fixed at 300 K. It can be seen that the zT value of the material needs to be above 2 if we want to achieve a comparable efficiency of the conventional energy conversion technique. Currently, the zT values of most TE materials are below 1. Therefore, improving the zT value of materials has become the primary goal in the field of TE materials.

2.1.2 Thermoelectric parameters

As discussed in the last section, the dimensionless figure of merit (zT) is a combination of four physical parameters (σ, S, $\varkappa_{\text{tot}}$, and T). A higher power factor ($PF=\sigma S^2$) and lower $\varkappa_{\text{tot}}$ result in a larger zT value. However, as shown in Figure 2-4, optimizing the TE performance is a relatively complex task due to the intercorrelations between the transport parameters (σ, S, $\varkappa_{\text{tot}}$). Thus, it is necessary to introduce the electrical and thermal parameters separately to claim the physical mechanisms behind them.

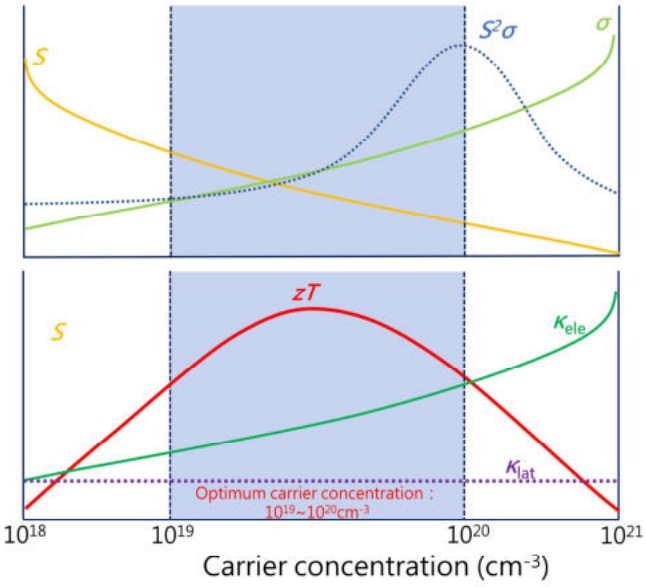

Figure 2-4 *Schematic diagram of the relationship between S, σ, κ_{ele}, κ_{lat}, and n*[58].

i) Electrical parameters

The relationship among the Seebeck coefficient (S), electrical conductivity (σ), carrier concentration (n), mobility (μ), and effective mass (m^*) in TE materials can be obtained using electronic band structure theory approximated by the single parabolic band (SPB) model.

$$\sigma = ne\mu \tag{2-13}$$

$$S = \mp\frac{k_e}{e}\left[\eta - \frac{(\lambda+\frac{5}{2})F_\lambda+\frac{3}{2}\eta}{(\lambda+\frac{3}{2})\mathrm{F}_\lambda+\frac{1}{2}\eta}\right] \tag{2-14}$$

$$n = 4\pi\left(\frac{2m^* k_B T}{h^2}\right)^{\frac{2}{3}} F_\lambda(\eta) \tag{2-15}$$

$$\mu = \frac{2e}{3m^*}\tau_e(\lambda+1)(k_B T)^{\lambda-\frac{1}{2}}\frac{F_\lambda(\eta)}{F_{1/2}(\eta)} \tag{2-16}$$

$$L = \left(\frac{k_B}{e}\right)^2\left\{\frac{(\lambda+\frac{7}{2})F_\lambda+\frac{5}{2}\eta}{(\lambda+\frac{3}{2})\mathrm{F}_\lambda+\frac{1}{2}\eta} - \left[\frac{(\lambda+\frac{5}{2})F_\lambda+\frac{3}{2}\eta}{(\lambda+\frac{3}{2})F_\lambda+\frac{1}{2}\eta}\right]^2\right\} \tag{2-17}$$

where $F_\lambda(\eta)$, η ($\eta = E_F/k_BT$), λ, τ_e, L, k_B, h, e, and T represent the reduced Fermi integral, scattering factor, electron relaxation time, reduced chemical potential, Lorenz number, Boltzmann constant, Planck constant, and absolute temperature, respectively.

With the above relations, it can be found that σ/S is closely related to the Fermi energy levels E_f, m^*, τ_e, and λ. These parameters are related to each other and cannot be regulated individually. Usually, in the study of TE materials, S can be increased by

element alloying or adding second phases, which could alter the band structure alignment.

ii) Thermal parameters

The nature of thermal conductivity in solids is related to the movement of microscopic particles and interparticle interactions that constitute the materials[37]. In most cases of single carrier conduction, the total thermal conductivity ($\varkappa_{tot}$) is the sum of the electronic thermal conductivity ($\varkappa_{ele}$) and the lattice thermal conductivity ($\varkappa_{lat}$), which can be expressed as

$$\varkappa_{tot}=\varkappa_{ele}+\varkappa_{lat} \tag{2-18}$$

According to the Wiedemann-Franz law, $\varkappa_{ele}$ can be expressed as

$$\varkappa_{ele}=L\sigma T \tag{2-19}$$

where L is calculated from Equation (2-17). It can be seen that $\varkappa_{ele}$ could be reduced by decreasing σ but may not be effective for increasing zT. Thus, $\varkappa_{lat}$, the only independent material property, plays a vital role in manipulating the thermal properties without influencing the electrical properties.

For most TE materials, the phonons dominate the heat transport, and $\varkappa_{lat}$ is determined by

$$\varkappa_{lat}=\frac{1}{3}C_v v_g \tau_p \tag{2-20}$$

where C_v is the specific heat, v_g is the group velocity, and τ_p is the phonon relaxation time. Among the parameters in Equation (2-20), minimizing τ_p by intensifying the scattering rate of phonons has been the focus in previous studies[37]. Different types of phonon scattering, including dominated Umklapp scattering (τ_U), have various frequency- and temperature-dependent τ_p values. Thus, different types of defects can be involved in the minimization of $\varkappa_{lat}$. Effective defects include point defects (PDs, zero dimension), dislocations (DS, one dimension), and phase interfaces between impurity and matrix (IF, two dimensions). The corresponding τ_p values are shown in Equations (2-21) as τ_{PD} τ_{DS} and τ_{IF}, respectively, all of which contribute to reducing the total τ_p for a low $\varkappa_{lat}$.

$$\frac{1}{\tau_p}=\frac{1}{\tau_U}+\frac{1}{\tau_{PD}}+\frac{1}{\tau_{DS}}+\frac{1}{\tau_{IF}}+\cdots \tag{2-21}$$

Hence, constructing dense phase interfaces by forming the second phase in the matrix to enhance interface phonon scattering is an effective method to reduce the total τ_p and $\varkappa_{lat}$.

2.2 Interface/surface modification of thermoelectric materials

2.2.1 Principles

As discussed in the previous section, the main concepts for optimizing the zT value converge towards two approaches: i) enhancing the PF in terms of electrical properties by point-defect engineering[5–7], band engineering[8–10], texturing[11–13], and energy filtering[14–16]; ii) decreasing the independent κ_{lat} via nanostructuring[17–19], phonon engineering[20–22], interfacial modifications[23–25], or searching for new TE materials with intrinsically low thermal conductivity[26–28]. Single-phase TE materials have been thoroughly investigated. However, their zT values can be further enhanced through the aforementioned strategies. Thus, the introduction of new materials into TE multiphase composites is another prominent approach attracting major scientific interest. When following the conventional melting route, second phases/precipitation may occur and disperse heterogeneously in the TE material due to the non-equilibrium state. Additionally, the compositions of precipitation are close to that of the matrix which constrains the selection of combinations between the second phase and matrix.

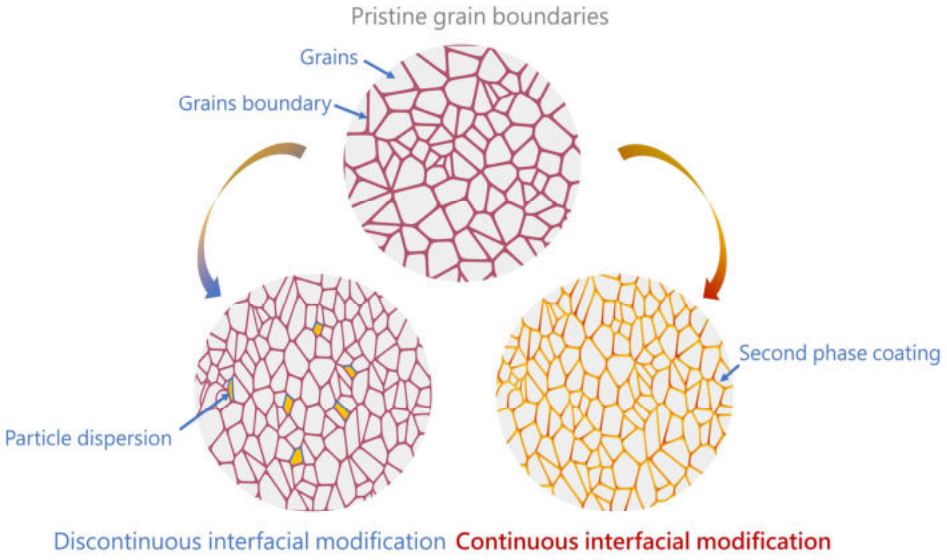

Figure 2-5 *Schematic diagram of the interface modification in TE materials.*

Uniform distribution and multiple-phase with different compositions can be achieved by manually adding the second phase into the matrix, such as directly dispersing the nanoparticles or forming a core-shell structure (Figure 2-5). Depending on the modification methods, the techniques of dispersion decorating or second-phase coating could establish discontinuous interfaces or continuous interfaces, respectively, between

the matrix and the second phases. It should be noted that surface modification approaches provide the possibility to combine different dispersions and matrices in such a way that two or more constituents with different thermodynamic stability conditions can be gathered in one system, endowing the final system with their specific advantageous characteristics. Furthermore, as opposed to other alteration methods (e.g., phase precipitation), the resulting chemical composition can be more finely tuned.

i) The effect on the thermal properties of interface modification

Regarding thermal transport, heat flow tends to bypass the dispersion when the $\varkappa$ of the matrix is higher than that of the dispersion (Figure 2-6(a))[63]. Owing to the larger mismatch in the acoustic impedance or phonon spectra between the second phase and the matrix phase, the introduced high-density interfaces between the dispersed nanoparticles and matrix are more effective in phonon scattering than normal grain boundaries. According to theoretical calculations, by increasing the dispersion size and thickness of the second phase coating, the second phase scatters phonons from short to long wavelengths[58]. Because of the mid-wavelength phonon scattering, the scattering will be more effective if the second phase is properly selected in terms of dispersion concentration/size or thickness of the second phase coating (Figure 2-6(b)), allowing for the zT values to be further improved[64]. Additionally, owing to the middle-wavelength phonon scattering and thermal resistance between the dispersion and matrix interfaces, a high decrease in lattice thermal conductivity that is unaffected by carrier transportation, can be expected.

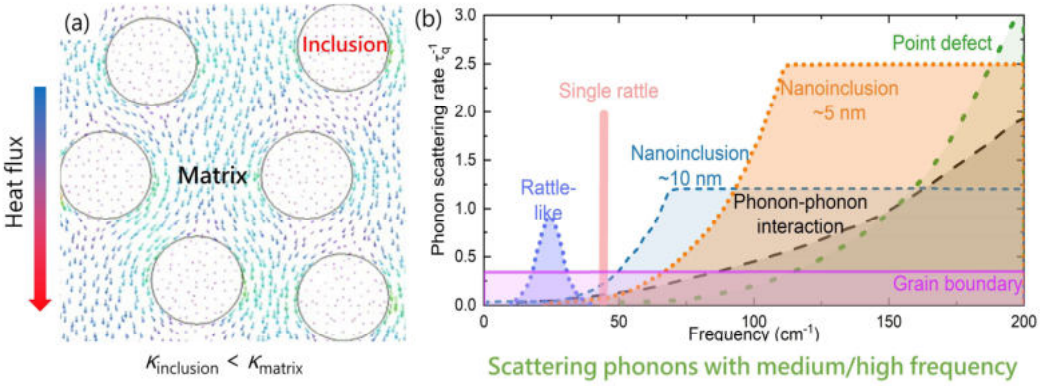

Figure 2-6 *(a) Heat flux vectors for dispersion of sphere-like inclusions in the matrix with* $\varkappa_{inclusion} < \varkappa_{matrix}$. *(b) Plot of phonon scattering rates for various mechanisms*[65].

ii) The effect on the electrical properties of interface modification

In terms of electrical transport, S can be enhanced by a mechanism known as electron energy filtering[66], as well as by modifying the resistance between the dispersion and the

matrix (Figure 2-7). This is achieved by curving the electron bands at the interfaces between the second phase and the bulk matrix, enabling the high-energy electrons to pass, while scattering the low-energy electrons. This selective scattering procedure can increase the value of S and therefore requires the appropriate materials to be used as second phases to ensure a beneficial band bending. There are mainly two key factors underlying the influence of the carriers on the electrical properties of energy filtering: i) the interface density and ii) the band alignment between the TE matrix materials and nanoinclusions. The interface density might be altered by the size and volume/weight fraction of the matrix and the dispersion. Additionally, the rate of nucleation and growth can be regulated through the appropriate selection of precursors and synthetic methods applied on both the matrix and the dispersion, especially when using solution-processed chemical synthetic methods. Band alignment can be adjusted by selecting dispersion materials matching the electronic band structure (e.g., bandgap, work function, or electron affinity) that can form suitable charge carrier traps or barriers[67]. A controlled potential barrier for energy filtering is expected to be optimized in the PF enhancement as reported by previous theoretical studies. However, research in the literature corroborating this energy filtering effect (e.g., carrier concentration, mobility/homogeneity of the second phase) remains scarce[68–70]. Consequently, the energy filtering mechanism responsible for PF boosting will be further investigated.

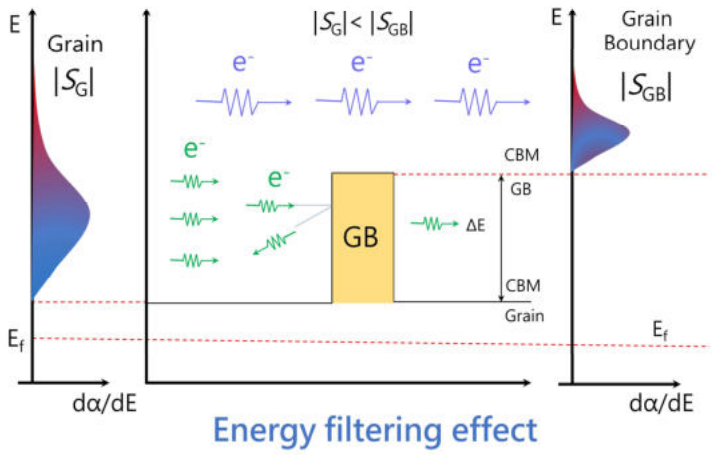

Figure 2-7 *Schematic diagram of influence on electrical properties by energy filtering effect*[35].

2.2.2 Discontinuous interface modification

The dispersion of the second phase into the TE material matrix is an essential approach for improving TE properties. It should be noted that the dispersion of the second phase differs from the precipitation which occurs mostly during the cooling stage of the synthetic process. According to the type of inclusions, they can be classified as metals,

semiconductors, oxides, and carbonic materials. Additionally, the dimensionality of the second phase also plays a critical role in the manipulation of the carrier and phonon scattering, as well as attaining a factorial improvement in the zT values. In general, the dispersion of metals can form the electrical conduct path but $\varkappa_{ele}$ increased. While the oxides are beneficial for suppressing the $\varkappa_{lat}$, electrical properties may deteriorate. Oxide compounds and metals may lead to the degradation of the electrical properties and increase the electrical thermal conductivity of a TE material, respectively. In this aspect, semiconductors may play a moderate and compensatory role in improving TE performance. The moderate band structure difference between the semiconductor (as the second phase) and the TE matrix will benefit the formation of potential energy wells and enhance the energy filtering effect, which may facilitate the manipulation of the electrical transports. However, the semiconductor inclusion should be properly selected to avoid the solubility of one phase into the other. The review as written previously offers a detailed analysis of discontinuous modification by dispersion and can be referred to in our published review[35].

2.2.3 Continuous interface modification

The continuous interface modification strategy entails commonly used chemical routes to form the core-shell structure, in which atoms or molecules are assembled into the grain boundary and heterostructures are created. In general, continuous surface modification can be divided into two categories: liquid phase synthesis and gas phase synthesis, all of which are referred to as "bottom-up" methods. On the other hand, directly mixing the second phase into the TE matrix decorates the dispersions on the boundaries and creates discontinuous islands, which can be referred to as the "top-down" process. Top-down approaches typically generate relatively large amounts of nanoparticles (~g scale) with wide particle size distributions, while offering easy material selectivity and requiring less complicated instrumentation. Conversely, bottom-up methods produce fewer nanoparticles (~mg scale) and have the benefits of offering better control over the morphology of the core-shell structure and can significantly improve TE performance. In either case, the use of continuous interface adjustment methods is highly encouraged for improving the zT values.

1.2.3.1 Liquid phase methods

The synthesis of TE core-shell nanoparticles can be mitigated by employing a variety of liquid phase-based synthesis methods[71]. In these strategies, either solid precursors are dissolved in suitable solvents or liquid precursors get in controlled contact with the core materials. These substrates can be nanowires, nano-dots, or nanoparticles in

general. By using a colloidal-based synthesis approach, both the core and the shell are synthesized together in a single pot[72–74]. The formation of the core is either achieved by reducing larger particles to the size of colloids (10–10^2 nm) or via the condensation of smaller molecules. The shell thickness can be controlled by the precursor concentration[75] and the pulsing time, i.e., the duration of having the core material in contact with the liquid precursor[76]. Additionally, in certain strategies, like precipitation- or hydrothermal-based methods, the pH values, and temperatures have an important influence on the shell thickness. Different liquid phase-based synthetic methods have been developed and improved over time, including hydrothermal/solvothermal, precipitation-based, colloidal, or reduction-based synthesis, with all sharing the same core idea: to use the core TE material as a template for the controlled (and sometimes epitaxial) growth of the shell.

1.2.3.2 Gas phase methods

The central concept underlying the gas phase synthetic process, apart from eliminating the second phase via gas removal, is shaping the core-shell structure by uniformly depositing the "shell" materials. According to the growth mechanism, the approach of gas phase synthesis can be mainly classified into physical vapor deposition (PVD) and chemical vapor deposition (CVD).

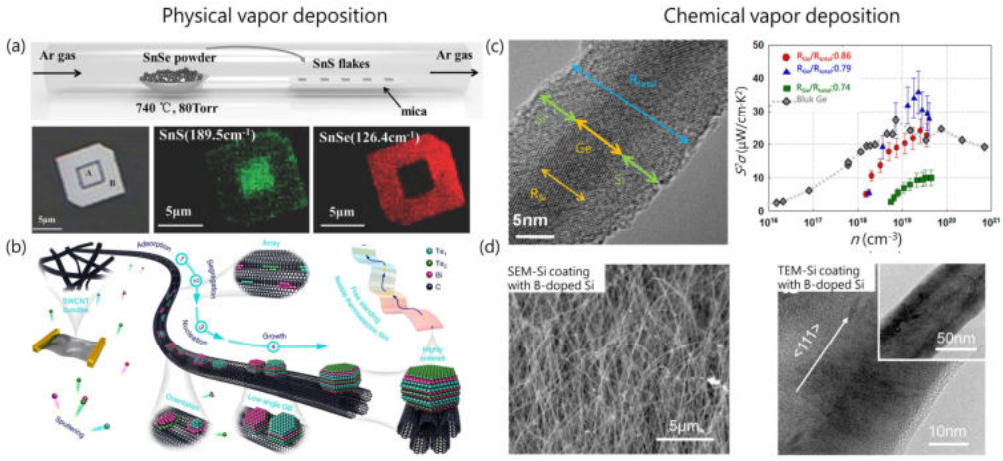

Figure 2-8 *(a) Schematic illustration of PVD growth of layered SnS-SnS_xSe_{1-x} core-shell heterostructures and the corresponding Raman intensity maps*[77]*. (b) Schematic illustration of the magnetron sputtering-based fabrication process and structure of a free-standing highly ordered Bi_2Te_3/single-wall carbon nanotube composites*[78]*. (c) TEM of CVD growth of Ge-Si core-shell heterostructures and their electrical properties*[79]*. (d) TEM of CVD growth of Si nanowires coating with B-doped Si*[80]*.*

i) Physical vapor deposition (PVD)

The PVD method is the deposition process where coatings are grown on the substrates, thereby necessitating the atomization or vaporization of the material from one or

several solid sources (usually called targets). It should be noted that the PVD process can change the surface properties and the transition zone between the substrates and the deposited materials. In addition, the substrate characteristics can also affect the film properties. The PVD deposition process can be conducted in a gaseous vacuum, plasma, or electrolytic environment[81,82]. The top panel of Figure 2-8(a) shows the epitaxial growth of orthorhombic SnS-SnS_xSe_{1-x} core-shell structures using a two-step PVD method[77]. The bottom panel of Figure 2-8(a) displays the optical image of the core-shell structure and its Raman characterization, confirming the SnS and SnS_xSe_{1-x} compositions of the inner and the outer regions, respectively. Since the PVD method is primarily based on the evaporation of the deposition materials and their subsequent removal via gas flow, it doesn't induce chemical bonding and may cause the formation of multilayers[83]. As illustrated in the schematic diagram in Figure 2-8(b), the layer-structured Bi_2Te_3 on the single-wall carbon nanotubes (SWCNTs) scaffold was synthesized using a magnetron sputtering technique[78]. The highly ordered (000*l*)-textured Bi_2Te_3 nanocrystals were anchored on high-quality SWCNTs bundles and the crystallites were decorated on their surfaces. The low lattice thermal conductivity of 0.26 ± 0.03 W/m·K was obtained for the Bi_2Te_3-SWCNTs, which was close to the minimum lattice thermal conductivity of 0.28 W/m·K[77]. This ultralow lattice thermal conductivity was theoretically derived from the high density of multiscale defects, such as Te vacancies/Te_{Bi} antisites, dislocations, phase interfaces, stacking faults, grain/twin boundaries, and randomly distributed nanopores, which significantly contributed to the scattering of a wide wavelength-range of phonons. Combined with the moderate *PF*, the zT of the flexible free-standing Bi_2Te_3-SWCNTs hybrid was increased to ~0.9 at 300 K.

ii) Chemical vapor deposition (CVD)

The CVD method can have similar results regarding the interface modification of the core-shell structure. During the CVD process, the vapor-liquid-solid mechanism serves as the typical growth model and the nanowires/nanoplates can be epitaxially grown on the substrate with the aid of precursors along a specific direction, that is controlled by the lowest formation energy. Wingert *et al.*[79] fabricated *p*-type Si-deposited Ge nanowires with different diameter ratios (R_{Si}/R_{total}) using the CVD method and they achieved different S and σ values by tuning the R_{Si}/R_{total} ratio. When the R_{Si}/R_{total} reached 0.79, the maximum *PF* of 36 ± 6 $\mu W \cdot cm^{-1} \cdot K^{-2}$ was obtained, which was much higher than that of bulk Ge (Figure 2-8(c)). Similarly, the intrinsic Si nanowires were coated with B-dope Si using the CVD method[80]. The diameters of the synthesized coated nanowires ranged between 20 and 200 nm (Figure 2-8(d)). Notably, the TE

performance changed with the different diameters, indicating that the core-shell structure characteristics had a huge influence on the electrical behavior.

These results verify that the appropriate core-shell structure design can be beneficial for achieving high TE performances; however, the line-of-sight transfer processes typically employed in PVD coating techniques can hinder the full coverage of complex geometries. Also, the non-conformal step coverage of CVD/PVD methods can be considered a major drawback when the modification of rugged surfaces is desired. Moreover, the above methods are mainly used in the fabrication of low-dimensional material devices, e.g., nanowires or thin films, while the preparation technologies of applied TE generators are mainly dependent on bulk materials sintered from TE material powders. Thus, applying methods that enable the conformal coating of particles and complex surface geometries provides beneficial and interesting alternatives.

Compared with traditional CVD methods, as a layer-by-layer deposition technique, atomic layer deposition (ALD)[84] is known for its unique capability of depositing highly uniform films in a controlled manner[85]. Thus, it gives us fresh insight into applying the coating layers on powders. The development of ALD on powders will be discussed in detail in the following sections.

2.3 Background of atomic layer deposition

A thin-film deposition technique called atomic layer deposition (ALD), also known as atomic layer epitaxy, is based on chemical processes that occur on the substrate surface and originate from chemical precursors in the vapor phase[84]. It might be viewed as a different type of CVD. In CVD, the precursors pulse together to fulfill chemical reactions. However, ALD operates discontinuously employing alternating pulses of precursors that are separated by pumping or purging stages. Each precursor exposure causes a specific, self-terminating half-reaction. Alternating these exposures allows the growth to proceed by merging the half-reactions into a full reaction, which results in the production of a (sub)monolayer of the desired material. One full reaction is referred to as one ALD cycle. The growth rate of films in ALD is defined by the total thickness/cycle number (growth per cycle, GPC). Typical values for the GPC are on the order of 1 Å/cycle, which is comparable to the length scale of interatomic distances; this is why the deposition technique is referred to as an "atomic layer". However, it may range over two orders of magnitude depending on the specific procedure. Typically, the GPC is precisely known and constant for a given procedure. By merely repeating these cycles, it is possible to precisely regulate the film thickness being deposited, which can control the thickness down to the nanoscale by adjusting the number of cycles.

2.3.1 An ALD process example

The thermal ALD of aluminum oxide reacting between trimethylaluminum ($Al(CH_3)_3$, TMA) and water (H_2O) is a well-understood, typical example for illuminating the general reaction chemistry of the ALD process. The detailed process is shown in the following reaction sequence:

1. TMA vapor is pulsed into an ALD chamber and reacts with the hydroxyl ($-OH$) groups present on the substrate surface. The TMA molecule is chemisorbed onto the surface, and the byproduct CH_4 is released:

$$\text{-OH}+\text{Al}(\text{CH}_3)_3 \rightarrow \text{-O-Al}(\text{CH}_3)_2+\text{CH}_4 \quad (2\text{-}23)$$

2. When the TMA pulsed into the chamber has fully reacted with the -OH site, the first half-reaction self-terminates. The excess TMA and the byproduct are purged.

3. Then, the second precursor, H_2O, is pulsed into the chamber. Similarly, it reacts with the methyl ($-CH_3$) group derived from TMA absorbed onto the surface. The -OH terminations on the surface are created, and the byproduct is released:

$$-\text{Al}(\text{CH}_3)_2+2\text{H}_2\text{O} \rightarrow \text{-Al}(\text{OH})_2+2\text{CH}_4 \quad (2\text{-}24)$$

4. When all $-CH_3$ sites have fully reacted with H_2O, the second half-reaction has finished. Additionally, the excess H_2O and byproducts are removed from the ALD chamber. One ALD cycle is finished, and more cycles can be repeated until reaching the desired thickness.

A schematic illustration of aluminum oxide ALD is shown in Figure 2-9.

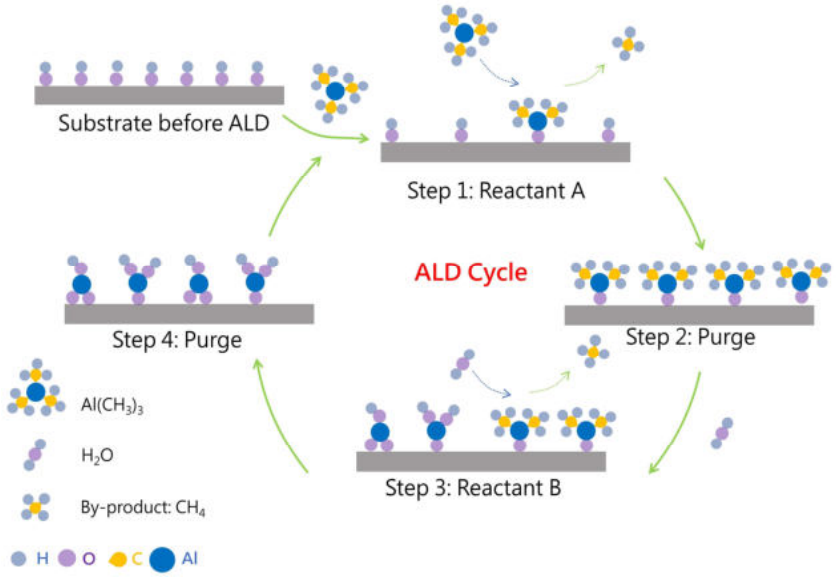

Figure 2-9 *Schematic illustration of thermal ALD of aluminum oxide based on TMA and water as vapor-phase precursors, showing the substeps within one cycle.*

2.3.2 Growth characteristics

In the ALD process, the growth characteristics are important for understanding the deposition mechanism behind them.

i) Growth linearity

Owing to the self-limiting feature of ALD, the GPC is constant at specific temperatures, implying that the film thickness is proportional to the number of cycles (Thickness=GPC×Number of cycles). As shown in Figure 2-10(a), there is linear growth with a constant slope. Notably, the nucleation effect may influence the GPC in the initial growth stage, which depends on the type of deposited substrates and materials.

ii) Temperature dependency

As described in the detailed ALD process, thin film growth is governed by the chemical reaction between the precursors, while the reaction temperature plays a vital role in determining the reaction rate. Thus, the substrate temperature in ALD is an important variable.

Generally, the typical temperature dependency of GPC is shown in Figure 2-10(b). In the low-temperature region, there is not enough thermal activation energy to proceed with the chemical reaction, which results in a decrease in GPC. Additionally, the precursors can also condense on the substrate surface due to the low reaction temperature, and the deposition process turns into normal CVD reactions, leading to an increase in GPC. In the high-temperature region, enough thermal energy may break up the bonding of the molecules of the precursors, leading to the decomposition of precursors. In this case, the extra ligands from the precursor decomposing can react with the other reactant and form the continuous deposition of the thin film even by a single precursor, resulting in an elevated GPC. In another case, there is no reaction between the extra ligands and other precursors, and those functional groups desorb from the substrate, leading to a decreased GPC.

In between the extreme conditions, the ‘‘temperature window” could be observed, and the GPC remained constant within the temperature window, which is quite an ideal and optimal ALD process. The real criterion for ALD-type growth is self-saturation.

iii) Self-saturation

In ideal ALD growth, the half-reactions triggered by precursor exposure need to be self-limiting. This result indicated that the GPC is "saturated" with increasing precursor exposure time. As shown in Figure 2-10(c), the GPC first increases with precursor

exposure time until the half-reaction is finished; after that, further exposure does not cause additional reactions, leading to a flattening of the GPC. The speed of saturation depends on the reactivity of precursors. A linear increase in GPC with precursor exposure occurs when CVD-type growth occurs because the deposition is continuous and does not reach saturation.

vi) Three-dimensional conformality

Due to the feature self-saturation, even a high specific surface area (e.g., nanowires, nanotubes, and trenches) in a three-dimensional structure that locally receives lower precursor fluxes will eventually be coated with uniform layers if there is insufficient exposure time. This is in contrast to CVD and PVD, where the deposited film thickness is proportional to the local precursor flux (Figure 2-10(d)).

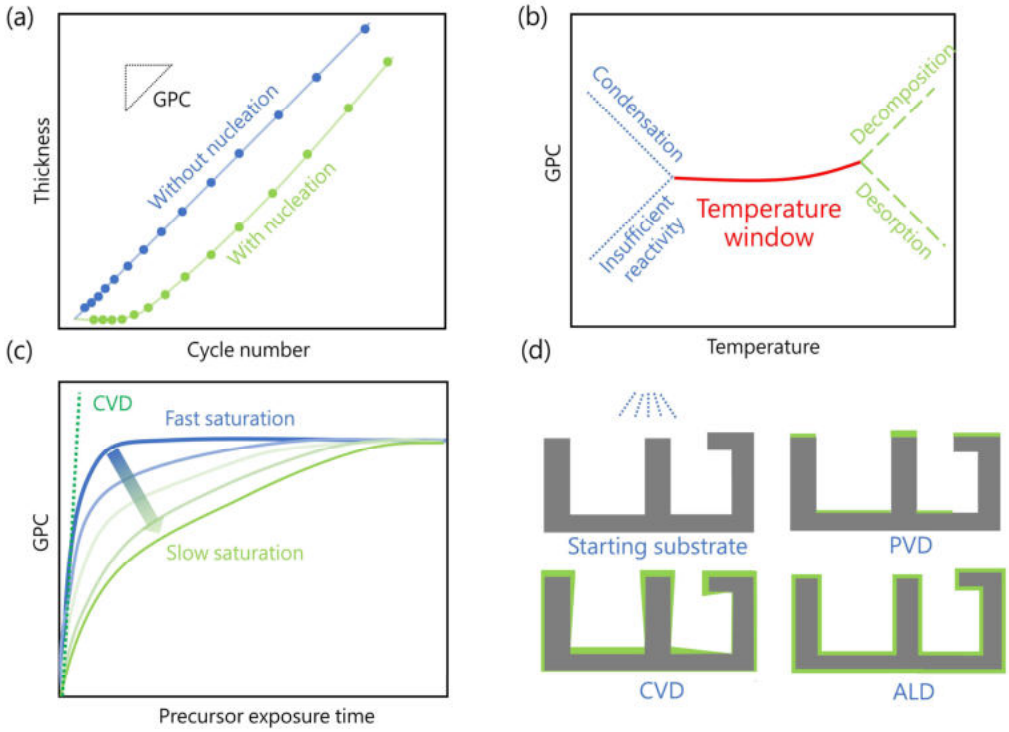

Figure 2-10 *Simplified graphs showing typical ALD growth characteristics: (a) growth linearity, (b) temperature dependency, (c) GPC saturation, and (d) diagrammatic illustration of coating conformality, showing an irregularly shaped substrate coated by using different deposition methods.*

2.3.3 Powder ALD

Due to controlled layer-by-layer growth, ALD can uniformly coat any structure, from planar substrates to three-dimensional structures, as discussed in the previous section. Hence, coating various kinds of layers on a powder surface can modify the physical and chemical properties of materials used in many fields, such as Li-ion batteries, catalysis, and TE. In practice, many engineering challenges are associated with coating

nanoparticles by ALD, which are related to the conformality, composition of coating layers, thickness, and most importantly, agglomeration.

i) Thickness/composition of coating layers/conformality

To control thickness, it is straightforward to increase the cycle number to realize thicker coating layers. However, it should be noted that the byproducts from the ALD chemical reaction may influence the composition of layers and conformality. For instance, TiO_2 thin films could be obtained by the precursors of $TiCl_4$ and H_2O. However, the byproduct of HCl may destroy the morphology of films due to HCl etching on the surface and change the composition of films[86].

Additionally, some processes do require long exposure times when ALD is carried out for high-aspect-ratio structures to obtain good conformality. The surfaces of the powders could be partially covered due to the sufficient exposure time of the precursors. Taking Al_2O_3 growth as an example, a conformal coating on a flat substrate can be produced in only milliseconds. When ALD is used to create conformal coatings on Bi particles with a 1.5 μm diameter, the exposure time is approximately 15 seconds.

ii) Agglomeration

Agglomeration is one of the most important technical challenges involved in covering individual nanoparticles. Many efforts have been made to build different types of powder ALD devices to accomplish uniform coating. Generally, powder ALD reactors can be classified into two types, as shown in Figure 2-11, i.e., gas fluidization and rotary reactors.

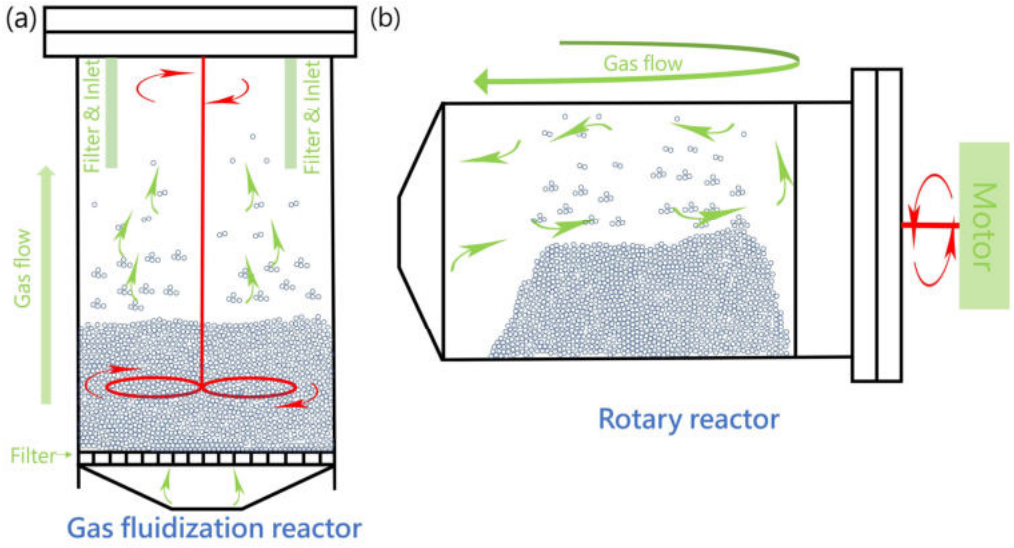

Figure 2-11 *Schematics of (a) a gas fluidization reactor and (b) a rotary reactor for powder ALD.*

In the gas fluidization reactor (Figure 2-11(a)), vibration, stirring, or other methods of agitation to prevent particles from agglomerating are utilized during the coating process to improve the uniformity of coatings. During ALD coating, the inserting carrier gas purge was combined with mechanical stirring to effectively fluidize nanometer- or micrometer-sized particles. Notably, the agglomerated particles exhibit dynamic agglomeration behavior in which agglomerates of primary particles continuously break apart and form again. However, gas fluidization methods face the problem of low precursor utilization efficiency. A large fraction of the precursor may be carried away by the fast, continuous gas that is necessary for particle fluidization. Thus, it is challenging to obtain a uniform coating.

In rotary reactors (Figure 2-11(b)), the coating tube can be rotated with the help of a motor at speeds of 1–60 rpm (rpm, revolutions per minute) to agitate the powder during the ALD process. This design reduces the loss of powders, and the device structure is quite simple. However, it should be noted that the coating parameters (size/density of the powder and rotating speed) should be carefully investigated and optimized. For instance, a rotation that is too slow will result in an inhomogeneous coating, but a speed that is too high will lead to the loss of powder brought by the gas flow.

2.4 Powder ALD in thermoelectricity

As a layer-by-layer deposition technique, atomic layer deposition (ALD) is known for its unique capability of depositing highly uniform films in a controlled manner and the thickness control can be down to the atomic level, enabling the deposition of extremely thin films, even only a few atoms thick. As shown in Figure 2-12(a), the concept of powder ALD can be divided into two procedures: preparing a TE powder with adequately tiny size and coating the shell materials with a rotation process.[87] The rotation process, combined with the small size of the powder particles, ensures a uniform coating even with a few cycles. Briefly, the powder size (d) and the potential energy barrier must be specifically designed to satisfy the relationship that τ_p (phonon momentum relaxation length) $<$ d (the particle size)$<$ τ_e (electron momentum relaxation length); in this manner, S will be improved without significantly decreasing σ, resulting in a substantial net improvement of PF[87]. Additionally, a large reduction in thermal conductivity can be achieved by depositing a few layers of specific materials on the interfaces of the TE material particles.

The idea of modifying the interfaces of TE materials using powder ALD was reported for the first time by Li *et al.* in 2016[87]. By employing a continuous-flow ALD reactor,

they achieved the deposition of an ultrathin ZnO layer on the surfaces of *n*-type $Bi_2Te_{2.7}Se_{0.3}$ TE powder particles using the precursors of diethylzinc (DEZ) and H_2O. Intriguingly, there was a proportional relation between the layer thickness and cycle number. Figure 2-12(b) presents the electrical and thermal transport values at 300 K for the samples coated with ZnO layers of varying thicknesses, indicating that both very thin (< 1 nm) and thick (> 6 nm) coating layers led to the vanishing of the carrier transports. The sample with the 2 nm-thick ZnO coating exhibited a high *PF* of 25.1 $\mu W \cdot cm^{-1} \cdot K^{-2}$, derived from its strongly enhanced *S* of -261 μV/K, which resulted in a high *zT* value of 0.58 at 390 K. Driven from these results, ZnO was selected for powder ALD on the surfaces of *p*-type $Bi_{0.4}Sb_{1.6}Te_3$ powder particles, using the same precursors.[88] As shown in Figure 2-13(a), energy dispersive X-ray (EDX) elemental mapping revealed clear phase boundaries between the matrix and the ZnO layer of the coated sample after 10 cycles. The excellent control of the powder ALD process increased the overall *zT* from 1.0 to 1.5 for the samples coated with an 8 nm-thick ZnO film.

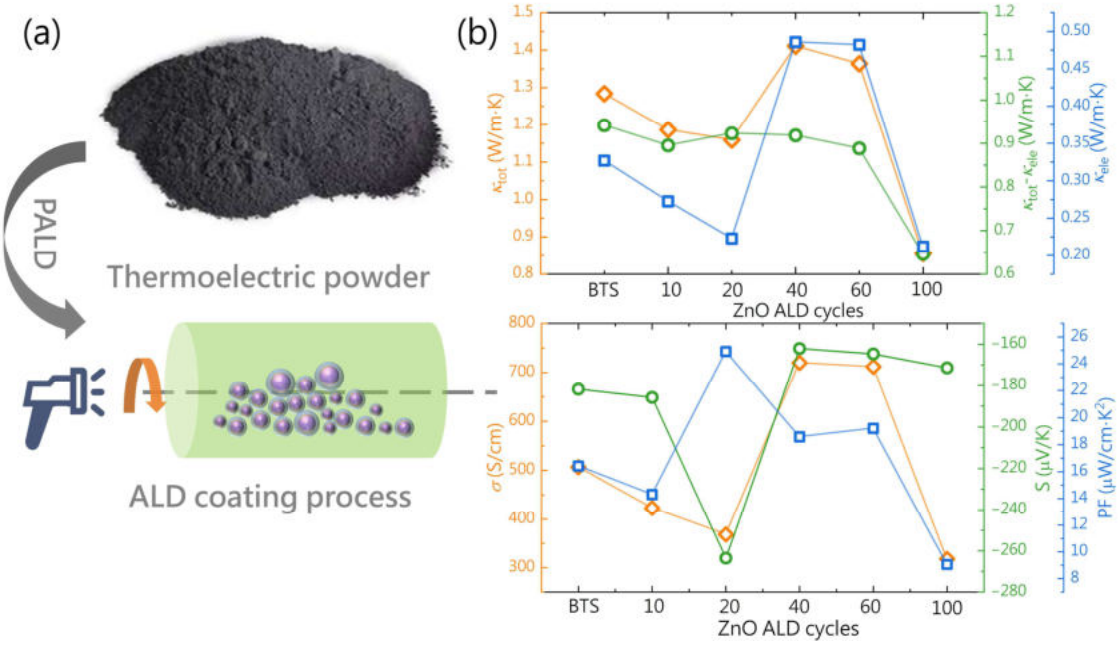

Figure 2-12 *(a) Schematic illustration of the powder ALD process*[88]*. (b) Dependence of the ALD cycle number on the thermal and electronic transport properties of ZnO layers in* $Bi_2Te_{2.7}Se_{0.3}$ *(BST) at 300 K*[54]*.*

Furthermore, the electrical resistivities of the samples showed a decreasing tendency between 0 and 5 cycles, whereas the opposite trend was observed between 6 and 15 cycles. This behavior induced the continuous reduction of the μ_H, even though the *n* initially increased and then decreased. The results from the Zn K-edge extended X-ray absorption fine structure analysis explained this phenomenon, by showing that Zn-Te

bonds were formed during the initial growth stage (< 10 cycles), which in turn caused the n to increase (due to the interactions between DEZ and Bi_2Te_3). This phenomenon enabled the Zn ions to act as acceptors which substituted the Bi/Sb sites. As the cycle number increased (> 10 cycles), however, the ZnO layer started to form and led to a decrease in the n. This pattern was also confirmed in the ZnO/SnO_2-$Bi_2Te_{2.7}Se_{0.3}$ system after even fewer cycles (< 10)[53], where the n in the ZnO-coated sample continuously decreased. On the contrary, the n in the SnO_2-coated sample showed the inverse trend with the increasing cycle number (Figure 2-13(b)). Thus, the S was improved after doing 5 ALD cycles of the ZnO layers while that decreased after the same number of ALD cycles of the SnO_2 layer, which can be attributed to the difference of the Zn^{2+} ions and Sn^{4+} ions.

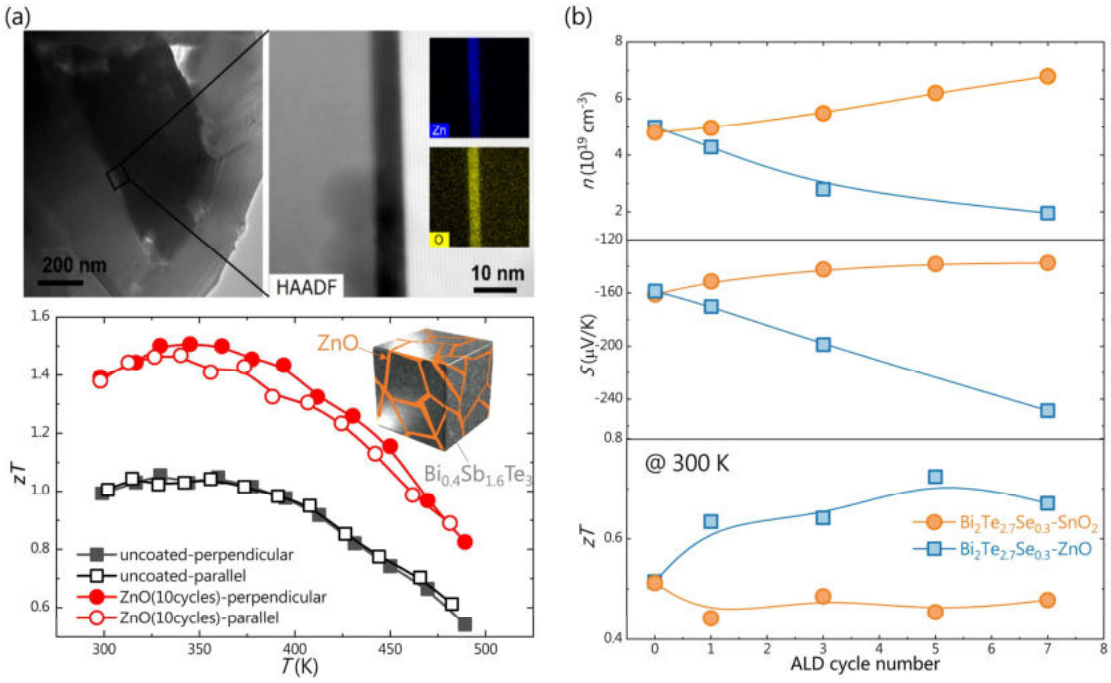

Figure 2-13 *(a) The TEM and EDS elemental mapping of the ZnO-coated $Bi_{0.4}Sb_{1.6}Te_3$ system and the temperature dependence of the zT values*[88]*. (b) ALD cycle number dependence on n, S, and zT values for the SnO_2- and ZnO-coated $Bi_2Te_{2.7}Se_{0.3}$*[53]*.*

It is worth noting that the coating layer may react with the core materials and form other phases during the pressing process. For instance, Zhang *et al.*[56] coated a $ZrNiSn_{0.99}Sb_{0.01}$ composite with an Al_2O_3 layer and observed the formation of Zr vacancies and ZrO_2 nanoparticles during the SPS process. The combination of Zr and O formed ZrO_2 phases in the amorphous Al_2O_3 layer, which in turn caused the generation of Zr vacancies in the $ZrNiSn_{0.99}Sb_{0.01}$ matrix. Therefore, the synergetic influence of the Zr vacancies and the ZrO_2 phases optimized the carrier scattering

performance, which resulted in the simultaneous enhancement of the S and σ. In a TiO_2-coated $Bi_2Te_{2.7}Se_{0.3}$ system[89], Bi_2O_x and Te secondary phases appeared in the form of precipitates, indicating that a small amount of oxygen had occupied the Te sites. Apart from the second phase, high-density dislocation clusters were observed on the interfaces between the TiO_2 and $Bi_2Te_{2.7}Se_{0.3}$ molecules. The diffusion of Te atoms and ZnO/Te interfaces, which further contributed to phonon scattering, can be observed in the TEM image of the ZnO-coated $Bi_2Te_{2.7}Se_{0.3}$ system[54]. The ALD-based interface engineering strategies were applied to improve the performance of TE materials which are summarized in Table 2-1.

Matrix	Shell	Optimum cycles	Pristine zT_{max}	zT_{max} -ALD	Ref.
$Bi_{0.4}Sb_{1.6}Te_3$	ZnO	10	1.06 at 360 K	1.52 at 360 K	88
$Bi_2Te_{2.7}Se_{0.3}$	TiO_2	10	0.69 at 400 K	0.91 at 430 K	89
$ZrNiSn_{0.99}Sb_{0.01}$	Al_2O_3	140	0.85 at 875 K	1.14 at 875 K	56
$Bi_2Te_{2.7}Se_{0.3}$	ZnO	5	0.52 at 300 K	0.73 at 300 K	53
$Bi_2Te_{2.7}Se_{0.3}$	SnO_2	7	0.52 at 300 K	0.48 at 300 K	53
$Bi_2Te_{2.7}Se_{0.3}$	ZnO	20	0.51 at 400 K	0.86 at 400 K	54
$In_{0.2}Yb_{0.1}Co_4Sb_{12}$	ZnO	5	0.69 at 687 K	0.64 at 687 K	55
$In_{0.2}Yb_{0.1}Co_4Sb_{12}$	SnO_2	1	0.69 at 687 K	0.57 at 687 K	55

Table 2-1 *Summary of typical TE systems coated with various materials using the powder ALD process.*

Although there are few studies in the literature discussing the effects of employing different precursor ligands on the core TE materials, the precursors should be meticulously selected to ensure that their reaction energy with the core materials will remain as low as possible during the coating process under high temperatures. Garcia et al. analyzed the chemical composition of core TE materials coated via the powder ALD process with different precursors[90]. The experimental results showed that the core material (γ-Fe_2O_3) was reduced to Fe_3O_4 after using tetrakis(dimethylamino)hafnium (TDMAHf) and tetrakis(dimethylamido)titanium (TDMATi) as precursors under a low process temperature (150 ℃); however, no reduction was observed with $TiCl_4$ as a core material. Additionally, the reaction energy of reducing Fe_2O_3 to Fe_3O_4 exhibited different values when distinct ALD precursors were used. According to the density functional theory (DFT) calculation results, the TDMAHf/TDMATi precursors can easily oxidize the core materials due to the low reaction energy. Thus, selecting the

appropriate precursors is crucial for preventing the oxidation of specific core materials. Nevertheless, the discussed results demonstrated that ALD is a promising approach for modifying the interfaces of TE materials to significantly improve their zT values.

2. 5 State-of-art in Bi, CuNi alloys, and Zn_4Sb_3

As discussed in previous chapters, the electrical and thermal transport properties are the key criteria for selecting promising TE materials. A desirable zT value indicates a large S, a high σ, and a low $\varkappa_{tot}$. In terms of thermal transport, the second phase could scatter more long-wavelength phonons than normal grain boundaries by continuous interface modification, which could effectively suppress $\varkappa_{lat}$. For the electrical properties, it is ideal that the PF involving S and σ can be enhanced due to the energy filtering induced by charge carrier scattering of the second phase. However, the electrical properties may deteriorate by the inclusions, i.e., little S increment and large degradation of σ. Apparently, TE materials with high PF values should be considered candidates and used for continuous interface modification. In this way, a small negative influence on the PF but a large decrease in $\varkappa_{tot}$ (especially for $\varkappa_{ele}$) can be expected. Therefore, elemental Bi and CuNi alloys with high PF are selected to improve their TE performance. In this section, the state-of-the-art TE performance of Bi and CuNi is discussed.

In addition, stability and reliability play an important role in a candidate TE material in practical TE devices. The coating layers may not only enhance the TE performance but also act as stabilizers to prevent the degradation of TE materials during the performance. Zn_4Sb_3 with high TE performance is introduced, and the thermal stability is also summarized.

2.5.1 Bi and CuNi

i) Bi

Bismuth (Bi) was the first elemental metal material to exhibit significant TE effects, but it has been overshadowed by the discovery of bismuth telluride alloys. Bi is a semimetal with an indirect overlap of the L (electron pockets) and T (hole pocket) bands, as well as a small direct energy gap in the L band. Because of the aforementioned band alignment, Bi is considered to be a poor TE material with a low S compared with classic TE systems because the S contributions from electrons and holes cancel each other out. However, as shown in Figure 2-14(a), Bi possesses a high PF (~25 $\mu W \cdot cm^{-1} \cdot K^{-2}$ for polycrystals and ~80 $\mu W \cdot cm^{-1} \cdot K^{-2}$ for single crystals) due to the large σ, which is contributed by holes and electrons.

Furthermore, Bi has a high $\varkappa_{ele}$ due to the transport of both holes and electrons, resulting in the high $\varkappa_{tot}$ value (Figure 2-14(b)). To date, available experimental results have primarily focused on fabricating a single crystal of Bi or alloying Bi with antimony to increase S and decrease $\varkappa_{lat}$. However, as the antimony content increases, the maximum zT values shift to lower temperatures (< 300 K), rendering it unsuitable for near-room-temperature TE devices. Although Bi has been extensively studied for decades, the question of how to increase S while decreasing the thermal conductivity to increase the zT value has remained unexplored.

ii) CuNi

Cu-Ni alloys, also known as constantan, are a type of conventional, low-cost, and environmentally friendly thermocouple material. At the beginning of the last century, constantan was already investigated, and several achievements in the mechanical and TE properties of constantan were reported. Compared with traditional metal materials, the Cu-Ni alloy possesses an ultrahigh PF (~50 $\mu W \cdot cm^{-1} \cdot K^{-2}$), which derives from the brilliant σ (~2×10^4 S/cm), as shown in Figure 2-14(b). The larger power factor favors higher power density when heat can be efficiently supplied and removed. Yamamoto *et al.*[91] reported a large power factor value of 120 $\mu W \cdot cm^{-1} \cdot K^{-2}$ at ~950 K with the composition of the $Cu_{30}Ni_{70}$ alloy. A relatively high power density of 1.18 W/cm^3 was obtained using a small 20-pair device made of constantan and chromel. Additionally, the CuNi alloy is ductile and can be deformed and processed easily, resulting in much better mechanical properties then the majority of metal-based TE materials such as filled-skutterudites, half-Heusler, and Zn_4Sb_3. Kang *et al.*[92] prepared bulk CuNi-based alloys with nanostructures by melting and cryo-rolling. The deformed CuNi contains nanotwins, which lead to a promising S of ~72.8 $\mu V/K$ and PF of ~110 $\mu W \cdot cm^{-1} \cdot K^{-2}$ at 1073 K.

Studies on the enhancement of the TE performance of CuNi alloys have mainly been focused on discontinuous interface modification (Figure 2-14(c)). For example, Yuan *et al.*[93] introduced carbon nanotubes to improve the TE performance of a Cu-Ni alloy. The 141% increase in the zT value over the pristine CuNi alloy is ascribed to the introduction of both porous structures and carbon-nanotube-metal interfaces, which significantly suppressed $\varkappa_{lat.}$ In other work, Guo *et al.* realized all-scale hierarchical architectures (point defects, second phases, nanocomposites, and micropores) by dispersing SiC into CuNi[94], leading to a significant reduction in thermal conductivity from 18.14 to 3.23 W/m·K at 773 K.

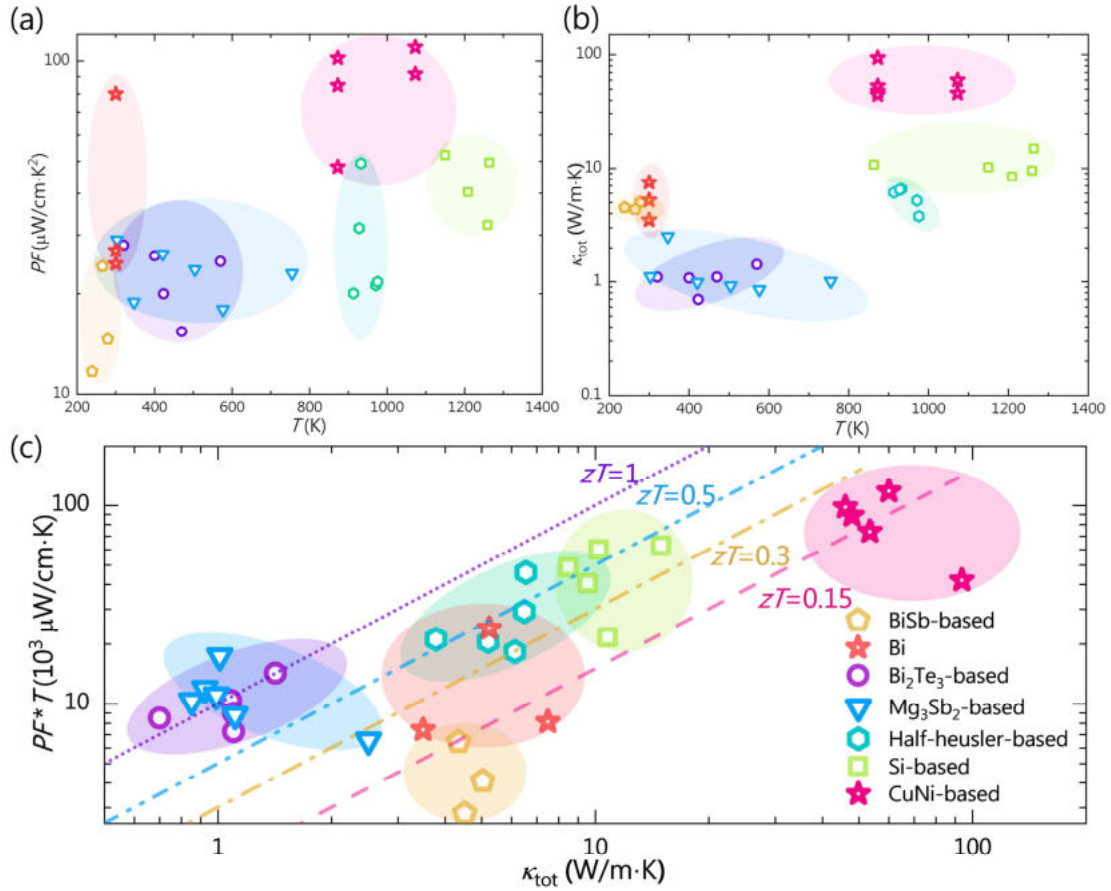

Figure 2-14 *The temperature dependence of optimized (a) PF and (b) κ_{tot} in different TE systems. (c) The κ_{tot} dependence of PF with the highest zT values in various TE systems.*

2.5.2 β-Zn_4Sb_3

Among brilliant TE candidates with intermediate working temperature regions (500–900 K), β-Zn_4Sb_3 possesses inexpensive and nontoxic elements and a relatively high zT value due to its ultralow thermal conductivity, indicating that it is a promising TE material (Figure 2-15(a)). β-Zn_4Sb_3 exhibits a hexagonal rhombohedral crystal structure (space group: *R-3c*), and Zn interstitial atoms result in "glass-like" thermal transport, which effectively suppresses κ_{lat}. Owing to diffused and disordered channels of zinc, κ_{tot} is much lower than that of other classic TE systems, such as PbTe and Bi_2Te_3 (Figure 2-15(b)). Additionally, the Zn interstitial atoms play a dual role as electron donors and Seebeck enhancers, as determined by the first-principal calculation of the electronic band structure.

However, the thermal stability of those "phonon-glass" compounds with interstitial ions could degrade under tremendous temperature differences and current bias. The temperature gradient and current drive the migration of interstitial atoms along the direction of the temperature gradient/current.

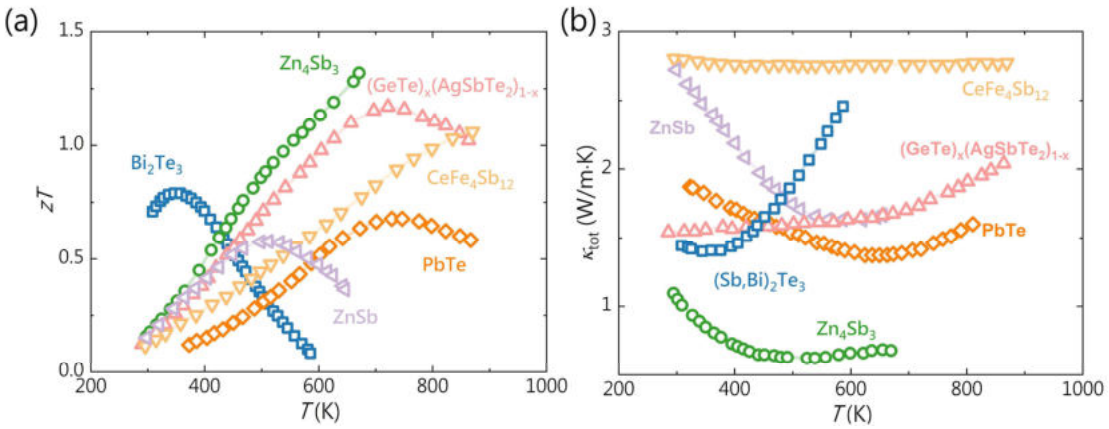

Figure 2-15 *(a) zT of β-Zn_4Sb_3 compared with other materials*[95]*. (b) Thermal conductivity of β-Zn_4Sb_3 compared with other materials*[95]*.*

Notably, Zn migration is related to the direction of the temperature gradient and current. This phenomenon is similar to the movement of the majority of carriers with the temperature difference in a TE generator, in which holes can migrate from the hot side to the cold side. Likewise, under a temperature gradient, Zn ions could accumulate on the cold side and form more Zn metal.

As shown in Figure 2-15(c), the prolonged measurement time and elevated temperature differences lead to an increase in resistance. Due to Zn ion migration, the part near the hot side exhibits larger S values (Figure 2-16 (a)). Zn migrates from the hot to the cold side of the sample to be expelled from the structure as Zn whiskers,[96] as shown in Figure 2-16 (b). Several strategies have been applied to Zn_4Sb_3 to explore the blocking effect:

i) Doping elements into the crystal structure to impede the movement of atoms

As an example, various elements such as Mg[97], Ag[98], and Pb[99] have been used to dope into the Zn site in β-Zn_4Sb_3. The results showed that doped samples are more stable than nondoped samples under thermal cycling. Unfortunately, all attempts thus far have led to a limited improvement in thermal stability.

ii) Reducing the critical electric potential difference of immigrating atoms by segmentation

For instance, Thorup *et al.* [100] claimed that the thermal stability of Zn_4Sb_3 legs could be enhanced by segmentation using stainless steel foil. The segmentation could reduce the critical electric potential difference of Zn, and the migration of the Zn ion is suppressed. However, the TE performance was reduced after segmentation with this

method. In addition, the mechanical properties of Zn_4Sb_3 legs could decrease due to the different thermal expansion coefficients between the stainless-steel foil and Zn_4Sb_3.

iii) Incorporating a second phase into an unstable TE compound to form the discontinuous interface modification

Second phases, such as oxides (such as ZnO[101] and TiO_2[96]), semiconductors (such as Cu_3SbSe_4[102]), and carbon-based materials[103], have been successfully used to prevent ion migration. However, the uniformity of particle distribution is an important issue for TE performance. Additionally, the minute particle size of the second phase requires higher and safer fabrication conditions.

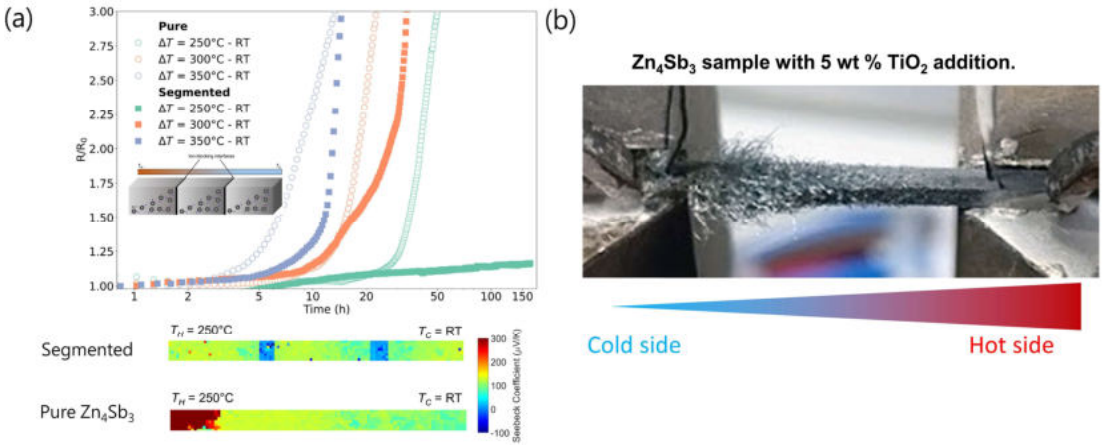

Figure 2-16 *(a) Normalized resistance as a function of time for segmented and β-Zn_4Sb_3 samples under various temperature gradients without external current and Seebeck mapping*[96]*. (b) Picture of the sample with 5 wt % TiO_2 after the temperature gradient*[96]*.*

Most works have been focused on the creation of energy barriers (either point defects or second phases), in which the blocking effect is satisfied under the operation condition and thermal stability is not fully optimized. However, with the help of powder ALD, millions of energy barriers induced by ALD coating layers could be constructed. Meanwhile, due to the layer-by-layer growth of powder ALD, the thickness and composition of the coating layers could be precisely tuned, which enables us to balance the thermal stability and TE properties. Thus, there is an urgent demand for new approaches for powder ALD to block Zn ion migration to stabilize the TE performance under a temperature gradient and current field.

3

Chapter 3 Experimental techniques

3.1 Material synthesis and preparations

i) TE powder syntheses and preparations

For the preparation of Bi powders, eight grams of high-purity Bi (99.99%, needles) was weighed and loaded into a stainless-steel ball-milling jar in a glove box and milled for 10 h in a SPEX 8000D machine. Zn_4Sb_3 was synthesized by ball-milling high-purity elemental Zn (99.9%, shot) and Sb (99.99%, shot) in stoichiometric proportions for various hours (1/2/4 hours) in the same milling machine (Figure 3-1(a)). Commercial CuNi alloy powders purchased from Nanoval GmbH & Co. KG were directly used in the experiments.

ii) Powder ALD process of coating the various powders

Different powders were coated in a commercial ALD reactor with a powder rotation option (Veeco Savannah S200) under a base pressure of 0.2 torrs (Figure 3-1(b)). For each experiment, 2 g of powder was transferred into the tumbler in the glove box. During the coating process, the tumbler was rotated at a speed of 2 rpm. Al_2O_3, ZnO, and TiO_2 layers were deposited using trimethylaluminum (TMA, 97%, Aldrich), diethylzinc (DEZ, Zn $\geqslant$ 52.0%, Aldrich), and $TiCl_4$ (97%, Aldrich) as Al, Zn, and Ti sources, respectively, reacting with H_2O as an oxidant at 150 °C. $SbCl_5$ (97%, Aldrich) and H_2O_2 (55%, Aldrich) were used for the deposition of Sb_2O_5 films. All of the precursors were kept at room temperature. The pulse/purge times were as follows: 0.015/15 s for TMA, DEZ, and H_2O and 0.03/15 s for $TiCl_4/H_2O$. The precursor was supplied to the chamber with a 20 sccm flow of N_2 gas. The optimized pulse and purge times for one ALD deposition cycle ($SbCl_5$/Ar/H_2O_2/Ar) were 0.3/15/1/15 s in Sb_2O_5 deposition.

iii) Pressing process of the coated powders

As shown in Figure 3-1(a), the coated powders with different layers were pressed into pellets by spark plasma sintering (SPS, AGUS-PECS SPS-210Gx). The powders were

pressed at various temperatures (473 K for Bi, 1073 K for CuNi, and 683 K for Zn_4Sb_3) for 10 min in a vacuum with a uniaxial pressure of 50 MPa. After polishing both sides, the obtained pellets were directly used to measure the physical properties. The relative densities of the bulk samples after SPS exceed 94%.

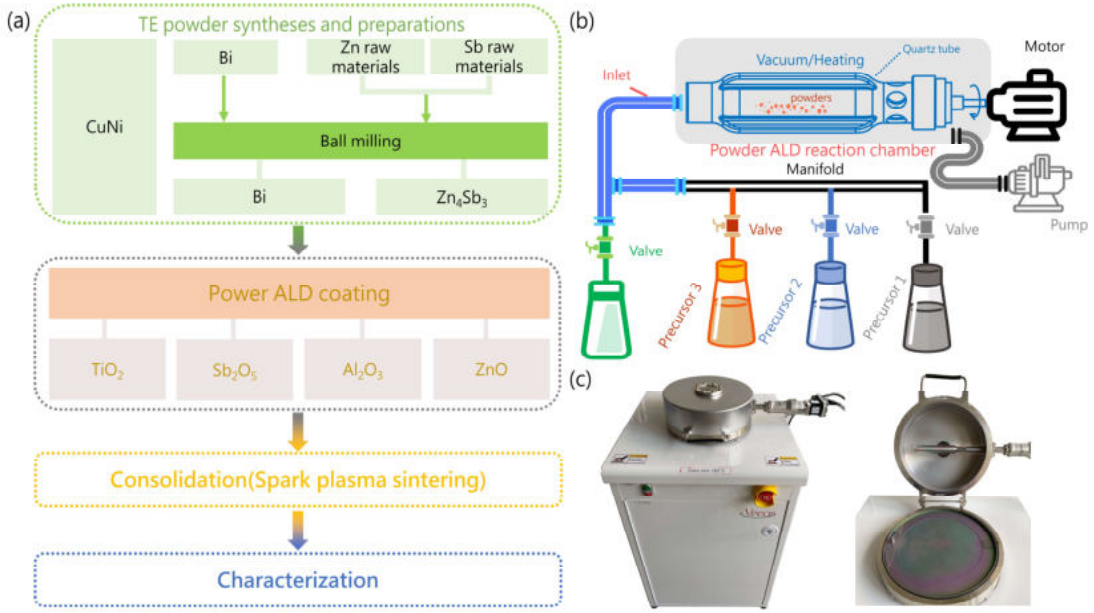

Figure 3-1 *(a) Schematic illustration of the sample synthesis experiments. (b) The powder ALD design and (c) optical images.*

3.2 Material characterizations

i) Characterizations of powders and bulks

Inductively coupled plasma–optical emission spectrometry (ICP–OES) measurements were conducted with an iCAP 6500 Duo View (Thermo Fisher Scientific) after aqueous acidic digestion to determine the composition of the powders.

X-ray powder diffraction (XRD) measurements for bulk samples were performed using a Bruker D8 with a Co source in the Bragg–Brentano mode to examine the phase purity and crystal structure of the samples. Powder XRD measurements were performed on a STOE STADI P diffractometer with Mo Kα1 radiation. The microstructures and fractured surfaces of the samples were analyzed by field emission scanning electron microscopy (FESEM, Sigma 300-ZEISS) and transmission electron microscopy (TEM, Titan 80-300 and Talos F200X, FEI). Cross sections of the lamella were prepared using a focused ion beam (FIB, FEI Helios Nanolab 600i, 30 and 4 kV Ga^+ ions) with a final thinning step using Ar^+ ion etching (GATAN PIPSII, 0.2 kV). High-angle annular dark-field scanning transmission electron microscopy (HAADF-STEM) imaging and scanning transmission electron microscopy-energy dispersive X-ray (STEM-EDX)

analyses were conducted by using a Titan Themis microscope (Thermo Fisher Scientific) equipped with an image corrector at an operation voltage of 300 kV. STEM-EDX spectrum imaging was acquired using a SuperX detector, and multivariate statistical analysis was applied to reduce the noise and separate areas with different compositions.

APT analysis was performed using a local electrode atom probe (CAMECA LEAP 5000 XS) in pulsed laser mode at a specimen base temperature of 60 K. The laser pulse energy, detection rate, and frequency were set to 50 pJ, 1%, and 125 kHz, respectively. Data reconstruction and analyses were performed with AP Suite 6.3, provided by CAMECA Instruments.

The temperature-dependent S and σ were measured by the standard four-probe method (LSR-3, Linseis). The temperature-dependent thermal diffusivity (λ) was evaluated by a laser flash method in a helium atmosphere (LFA 1000, Linseis). The density (D) of the samples was measured by the Archimedes method, and the heat capacity (C_p) was calculated using the Dulong-Petit law. The total thermal conductivity ($\varkappa_{tot}$) was calculated according to the relationship $\varkappa_{tot} = \lambda D C_p$. The Wiedemann-Franz law can be used to calculate $\varkappa_{ele}=L\sigma T$, where L is the Lorenz number and is described as $L=1.5+exp\ (-|S|/116)$. The carrier concentration (n) and Hall mobility (μ_H) were determined from 10 K to 300 K with Hall measurements in the van-der-Pauw geometry with a physical property measurement system (9 T LOT Dynacool system).

ii) Characterizations of thin films

The thickness of the thin films was measured using X-ray reflectivity (XRR, Philips X'Pert Pro MRD). The surface morphology was studied by atomic force microscopy (AFM, Bruker Dimension Icon). X-ray photoelectron spectroscopy (XPS) was used to determine the chemical state of the element in the compounds and was conducted using a Thermo Scientific K-Alpha$^+$.

In the following section, several characterizations in this thesis are discussed in detail to introduce the mechanisms of measurement methods.

3.2.1 ICP–OES

As an elemental analysis technique, inductively coupled plasma optical emission spectroscopy (ICP–OES) can obtain the element contents in the samples from the emission spectra of elements excited within a high-temperature plasma (Figure 3-2).

In ICP–OES, the sample is usually in the form of liquid for the introduction system, but most of our samples are in the of powder form. Therefore, it is necessary to first dissolve the powders with a microwave at 150 °C for 20 seconds in a mixture of nitric

and hydrofluoric acid. Then, the liquids with dissolved powders are introduced into the plasma, and the optical system (spectrometer) is utilized to separate wavelengths of light, which correspond to different elements. The spectrometer can efficiently concentrate the resolved light onto the detector. Two components make up the spectrometer: a mono- or polychromator and fore-optics. As the light exits the mono- or polychromator, it is focused onto the detector, and the derived signals are analyzed to quantify the elemental composition.

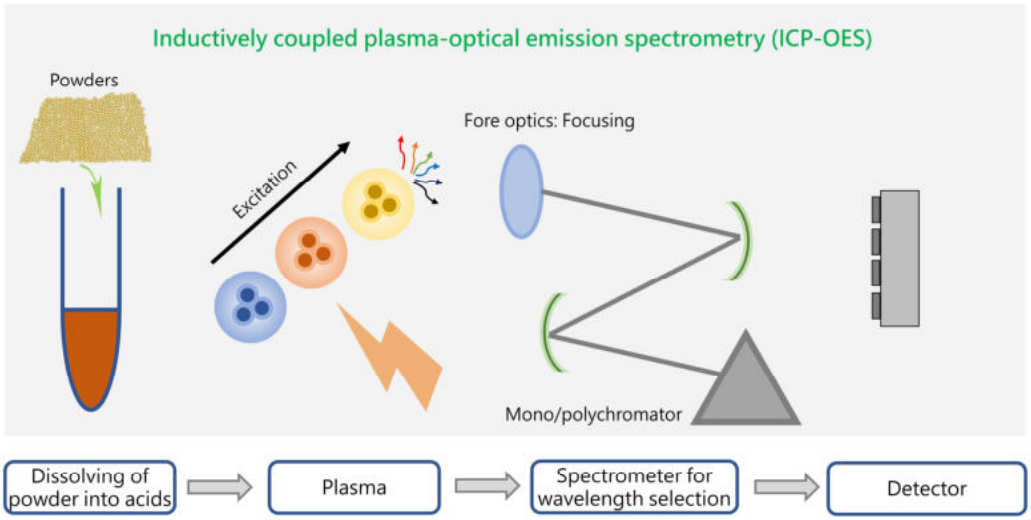

Figure 3-2 *Basic components of ICP–OES*[104].

3.2.2 APT

Atom probe tomography (APT) provides three-dimensional compositional mapping at the atomic scale (approximately 0.1–0.3 nm resolution in depth and 0.3–0.5 nm laterally). The sensitivity of APT is in the range of parts per million for all elements (including light elements such as hydrogen, carbon, or lithium). The APT technique has contributed to defect identification, such as dislocations and nanoprecipitation, in the TE field.

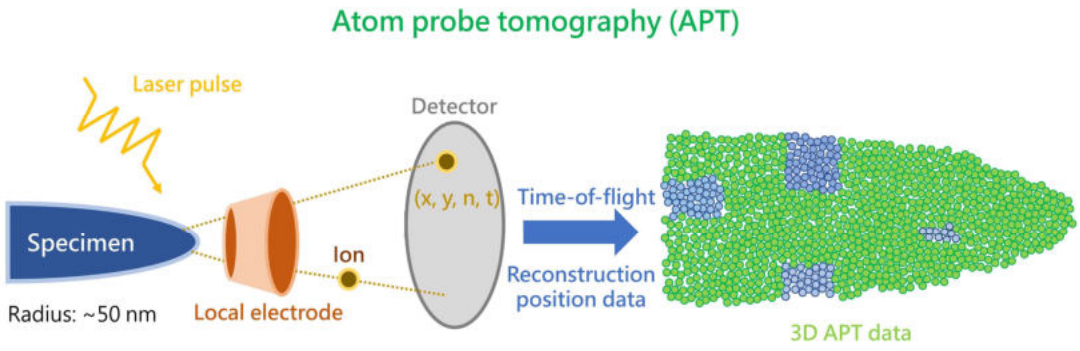

Figure 3-3 *Schematic illustration of APT principle*[105].

The samples are usually required to be made into the form of tips with a maximum diameter of 50 nm (Figure 3-3). A high direct current voltage is applied to the cooled tip (3–15 kV). Then, an extremely strong electrostatic field (tens V/nm) is generated on the surface of the tip, while it should be just below the point of atom evaporation. As the laser pulses, one or more atoms are evaporated off the surface by the field effect (almost 100% ionization). These atoms are then projected onto a position-sensitive detector (PSD) with a high detection efficiency. The best analytical efficiency of any three-dimensional microscope is achieved with ion efficiencies of up to 80%. The specimen and the 2D position-sensitive detector are depicted in Figure 3-3, which demonstrates the basic workings of atom probe tomography. A laser or voltage pulse operating on the specimen's tip causes the evaporation of ions at time t (pulse), and at time t (event), the ion arrives at the detector. By repeating this evaporation process, the atoms in the tip are progressively removed, and a three-dimensional compositional map can be reconstructed at the atomic scale.

3.2.3 LSR and LFA

The temperature-dependent S and σ were simultaneously measured by the standard four-probe method (LSR-3, Linseis). The sketch of LSR is shown in Figure 3-4(a), and the measured bar-shape or disked-shape sample is mounted between the upper and lower blocks. To create a temperature gradient, the generated heat from the lower block passed through the sample at a fixed measurement temperature. As the stable temperature gradient over the sample is established, the thermocouples can detect two different temperatures (T_2 and T_1). At the same time, the thermal electromotive force or the Seebeck voltage (dV) is obtained. Additionally, at a fixed temperature, the electrical resistivity can be measured by the four-point probe method. As a constant current will go through the whole sample, the voltage gradient between the above two thermocouples can be measured as well. The uncertainties of σ and S are $\pm$ 10% and $\pm$ 7%, respectively.

The LFA measuring methodology is displayed in Figure 3-4(b). The bottom of the measured sample is heated by laser pulsing. The heat will conduct from the sample's bottom to its top. Therefore, the detector is able to track the variation in time-dependent temperature. The temperature-dependent thermal diffusivity may be calculated by the mathematical model of temperature rise. The uncertainty of the value measured by LFA is approximately 10–20% using the Dulong-Petit law calculated C_p. Therefore, differential scanning calorimetry (DSC) could be used to provide a more accurate measurement of heat capacity.

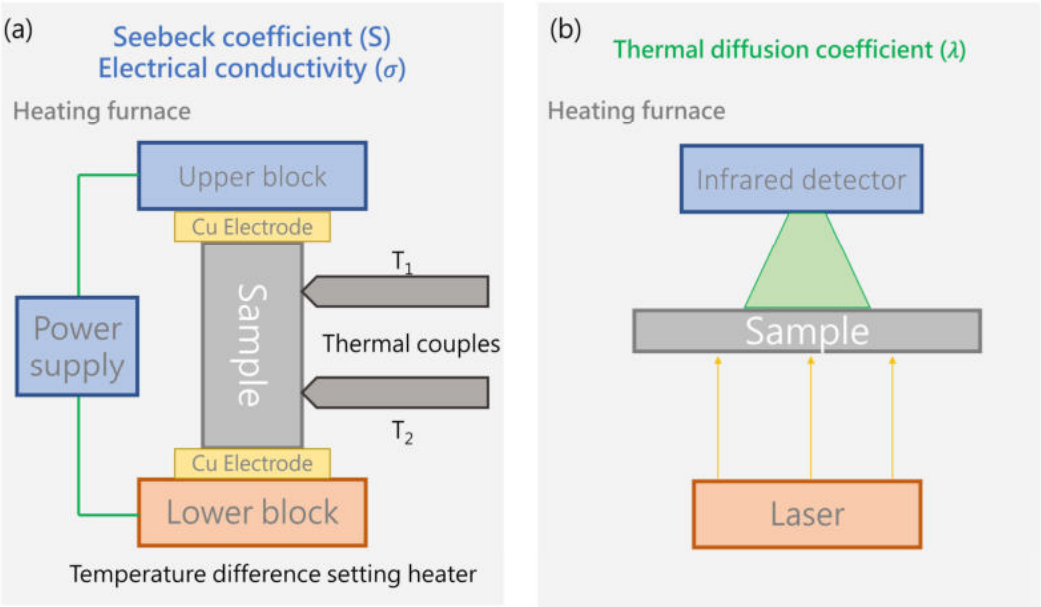

Figure 3-4 *Schematic illustration of (a) LSR and (b) LFA*[106].

3.2.4 GIXRD

Grazing incidence X-ray diffraction (GIXRD) is a surface-sensitive diffraction technique that utilizes a small incident angle X-ray beam to limit penetration into the bulk material and optimize the intensity. (Figure 3-5). Conventional $\vartheta/2\vartheta$ scanning methods often provide a weak signal from the surface layer but a strong signal from the substrate of the sample, making it challenging to investigate the properties of thin films deposited on substrates. During GIXRD, the X-ray scanning measurements with a set grazing angle of incidence can evade this high signal from the substrate to obtain a better-quality signal from the films on the surface. The fixed angle is generally chosen to be slightly above the critical angle for the total reflection of the films.

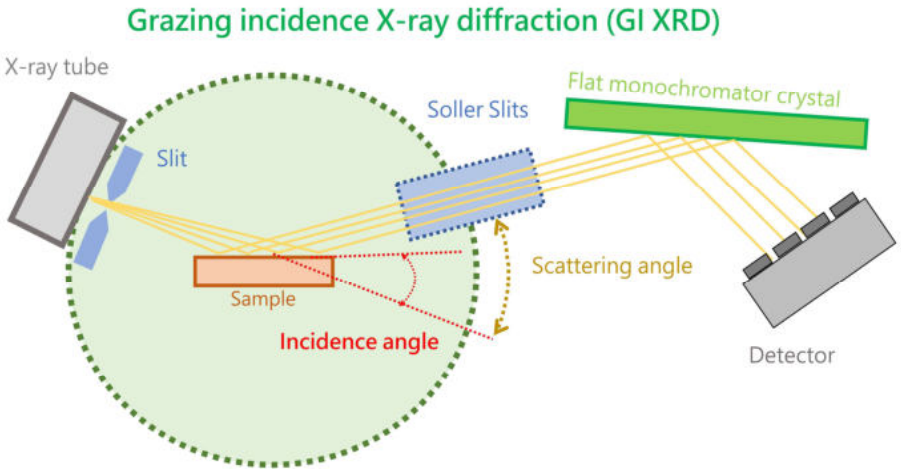

Figure 3-5 *Schematic illustration of GIXRD*[107].

3.2.5 XPS

To obtain more information regarding the Sb states in the newly developed ALD Sb_2O_5 thin films, X-ray photoelectron spectroscopy (XPS) was carried out to determine the oxidation state of Sb. As a surface characterization technique, XPS can provide information on the chemical bonding of thin films. The photoemission principle of XPS is shown in Figure 3-6. When X-rays irradiate the sample surface, electrons can be emitted from atoms because they exceed the binding energy of electrons. Additionally, the energy is proportional to the frequency ($h\nu$), not the intensity or length of exposure to the incident electromagnetic radiation. Because each electron has a unique binding energy and atoms might have many orbitals at various energy levels, the reaction will result in a range of released electrons with various binding energies (and kinetic energies), providing an XPS spectrum (Figure 3-6).

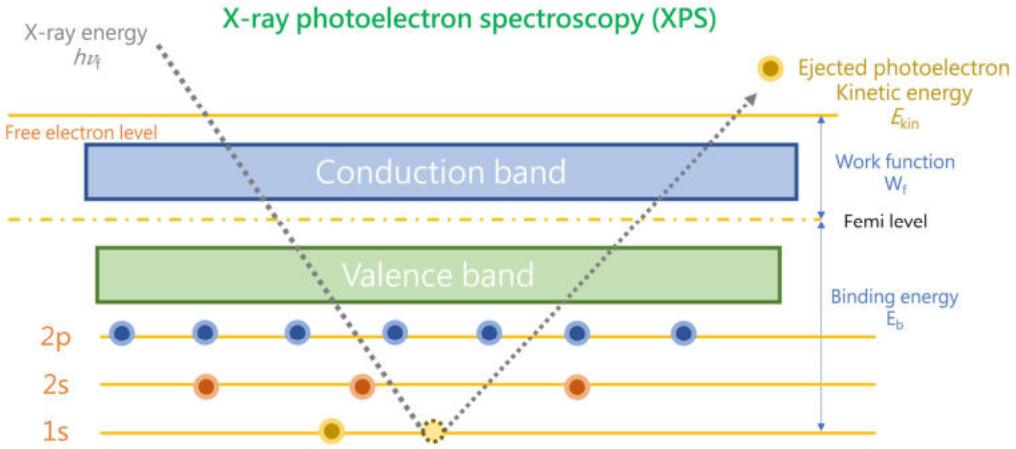

Figure 3-6 *Schematic illustration of XPS*[108].

4

Chapter 4 Effect of powder ALD interface modification on the thermoelectric properties of Bismuth

The majority of the presented results in this chapter have been published in the following articles:

Shiyang He, Amin Bahrami*, Xiang Zhang, Ignacio González Martínez, Sebastian Lehmann, Kornelius Nielsch*, Effect of Powder ALD Interface Modification on the Thermoelectric Performance of Bismuth, ***Advanced Materials Technologies***, 2022, 7(5), 2100953. (Chapter 4.2)

Shiyang He, Jun Yang, Amin Bahrami*, Xiang Zhang, Ran He, Martin Hantusch, Sebastian Lehmann, and Kornelius Nielsch*. Surface Modification of Bismuth by ALD of Antimony Oxide for Suppressing Lattice Thermal Conductivity. ***ACS Applied Energy Materials***, 2022, 5(4), 4041-4046. (Chapter 4.3)

4.1 Introduction

Bismuth (Bi) was the first elemental metal material to exhibit significant TE effects, but it has been overshadowed by the discovery of bismuth telluride alloys[59]. Because of the aforementioned band alignment, Bi is considered a poor TE material with a low S because the S contributions from electrons and holes cancel out each other. Furthermore, Bi has high $\varkappa_{ele}$ due to the transport of both holes and electrons, resulting in high total thermal conductivity[109]. To date, available experimental results have primarily focused on fabricating a single crystal of Bi or alloying Bi with antimony to increase S and decrease $\varkappa_{lat}$[110–112]. However, as the antimony content increases, the maximum zT values shift to lower temperatures ($<$ 300 K), rendering it unsuitable for near-room-temperature TE devices[112,113]. Although Bi has been extensively studied for decades, the question of how to increase S while decreasing the thermal conductivity to increase the zT value has remained unexplored.

4.2 The influence of Al_2O_3, TiO_2, and ZnO layers on TE properties

The purpose of this research is to improve the TE performance of polycrystalline bismuth utilizing a powder ALD method with coating layers of Al_2O_3, TiO_2, and ZnO. For the first time, ultrathin layers of Al_2O_3, TiO_2, and ZnO are deposited on the surface of ball-milled Bi powders. Microstructural analyses show that grain growth could be suppressed after the deposition of Al_2O_3, ZnO, and TiO_2 coatings during the sintering process. The experimental results show that, by tailoring the microstructure at the atomic scale, S can be improved from -68 μV/K to -79 μV/K after 5 cycles of Al_2O_3 coating. The enhanced S of Bi coated with a few atomic layers of Al_2O_3 is significantly higher than that of most pure polycrystalline metals (Figure 4-1(a)), such as Sb, Mo, Pb, and so on[114–116]. As a result of the reduction in the thermal conductivities, the zT values and zT_{avg} of all of the coated samples were enhanced (Figure 4-1(b) and (c)), and the highest zT of ~0.15 was obtained for the 5 cycles Al_2O_3-coated sample at 390 K (~0.13 at 300 K), which was higher than that of some typical near-room temperature TE materials[59,113,117–119], such as $YbAl_3$[117] and Ta_4SiTe_4[119] (Figure 4-1(d)). Our findings demonstrate that powder ALD-based interface modification could be applied as a general route to decouple the strongly interrelated parameters and thus enhance TE performance.

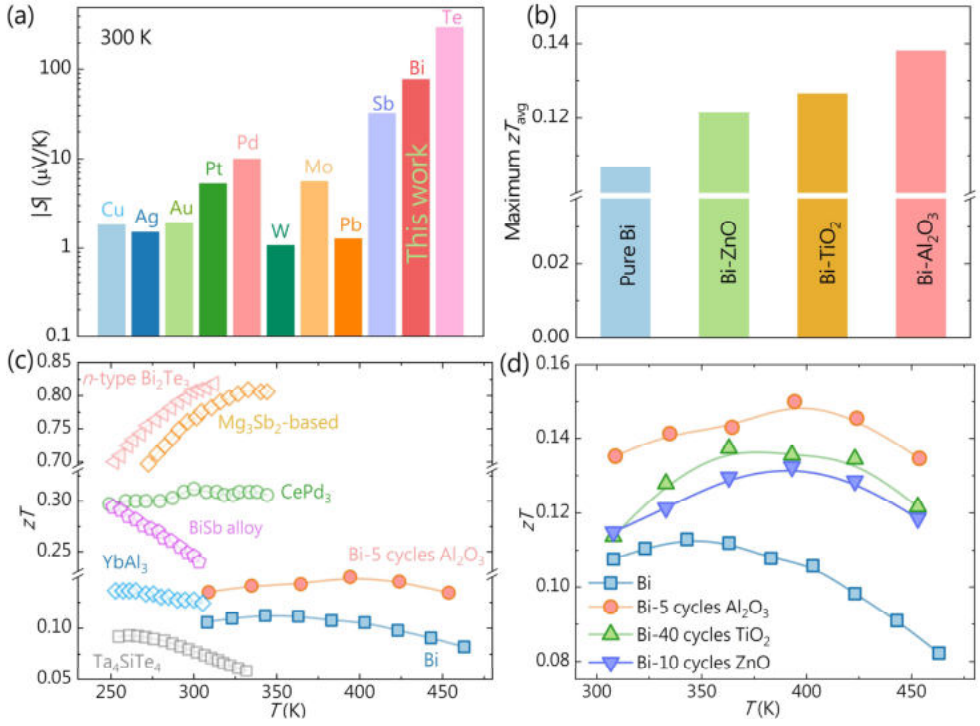

Figure 4-1 *(a) Temperature dependence of maximum zT values in Al_2O_3-, TiO_2-, and ZnO-coated samples*

and pure Bi. (b) Comparison of average zT values for Al_2O_3-, TiO_2-, and ZnO-coated samples and pure Bi from 300 to 453 K. (c) Temperature-dependent zT comparison of several TE materials and Al_2O_3-coated Bi[59,113,117–119]*. (d) Typical comparison of S among various pure metals and Al_2O_3-coated Bi at 300 K*[114–116].

4.2.1 Characterizations of Al_2O_3, ZnO, and TiO_2 ALD thin films

Al_2O_3, ZnO, and TiO_2 films are deposited using the powder ALD method in specified cycles to systematically examine the influence of various oxide coatings on the microstructural characteristics of Bi (Figure 4-2). According to earlier research on Al_2O_3, TiO_2, and ZnO thin films, TiO_2 thin films grow at a considerably slower rate than Al_2O_3 and ZnO thin films[120–122]. As illustrated in Figure 4-2(a), two coating recipes with distinct pulse modes were devised to ensure the uniform and conformal coating of the particles. The thin film thickness changes on the Si-SiO_2 and Si wafers by cycle number are shown in Figure 4-2(b). The excellent thickness controllability at the subnanoscale is evidenced by a linear increase in thickness proportional to cycle numbers. Using the aforementioned recipes, growth rates of 0.67, 0.90, and 2.42 Å per cycle were calculated for TiO_2, Al_2O_3, and ZnO with Si-SiO_2 wafers, respectively, consistent with the literatures[120–122] (Figure 4-2(b)). Furthermore, GIXRD analysis confirmed the amorphous nature of the TiO_2 and Al_2O_3 thin films, as well as the crystalline structure of the ZnO thin films, as previously reported (Figure 4-2(c))[42,123,124]. The XRD patterns of the ALD-coated samples showed no crystalline peak for Al_2O_3 and TiO_2, which could be due to the amorphous nature of the Al_2O_3 and TiO_2 layers, as well as the low content of ZnO (see Figure Appendix A).

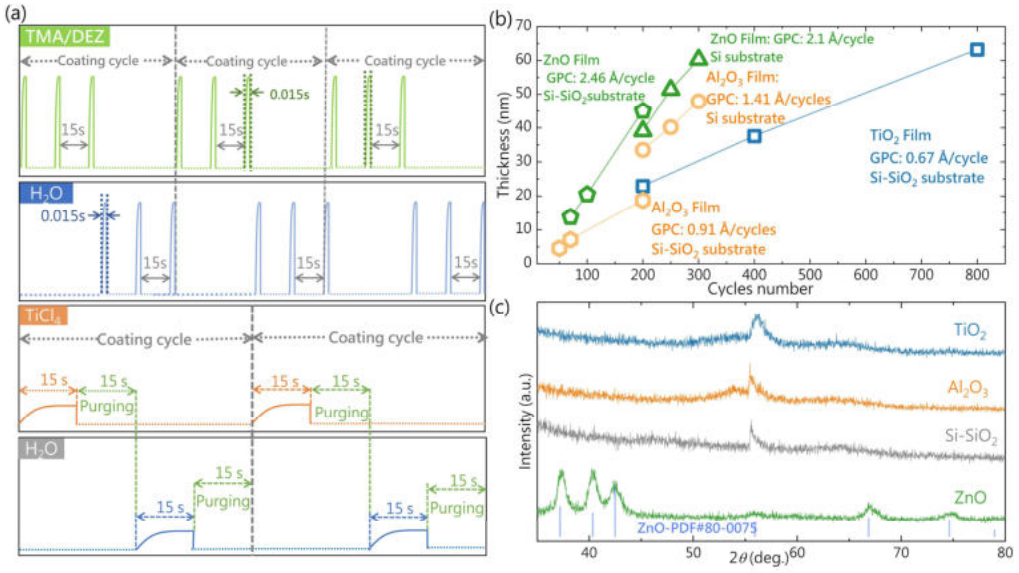

Figure 4-2 *(a) The pulsing and purging process for Ti-, Zn-, and O-precursor in powder ALD process.*

(b) The plots of cycle number vs thickness for TiO_2, Al_2O_3, and ZnO thin films deposited on the Si-SiO_2 and Si substrates. (c) The GIXRD patterns of TiO_2/Al_2O_3/ZnO thin films deposited on the Si-SiO_2 substrates.

4.2.2 Microstructural characterizations of bulks

The SEM fractured surfaces of various sintered Bi pellets are shown in Figure 4-3(a), indicating that all of the sintered samples were well crystallized and void-free, consistent with a density > 95%. It can also be noted that the fractured surface for single-phase bulk Bi showed a typical coarse and anisotropic structure without apparent preferential orientation for grains. However, the ALD of Al_2O_3, TiO_2, and ZnO significantly influences the size, morphology, and growth of Bi particles during the SPS process, as illustrated in Figure 4-3(a). The fractured surfaces of the Al_2O_3- and ZnO-modified samples had a different morphology from those of the Bi-TiO_2 system, with no obvious grain boundaries and only partially covered grains visible.

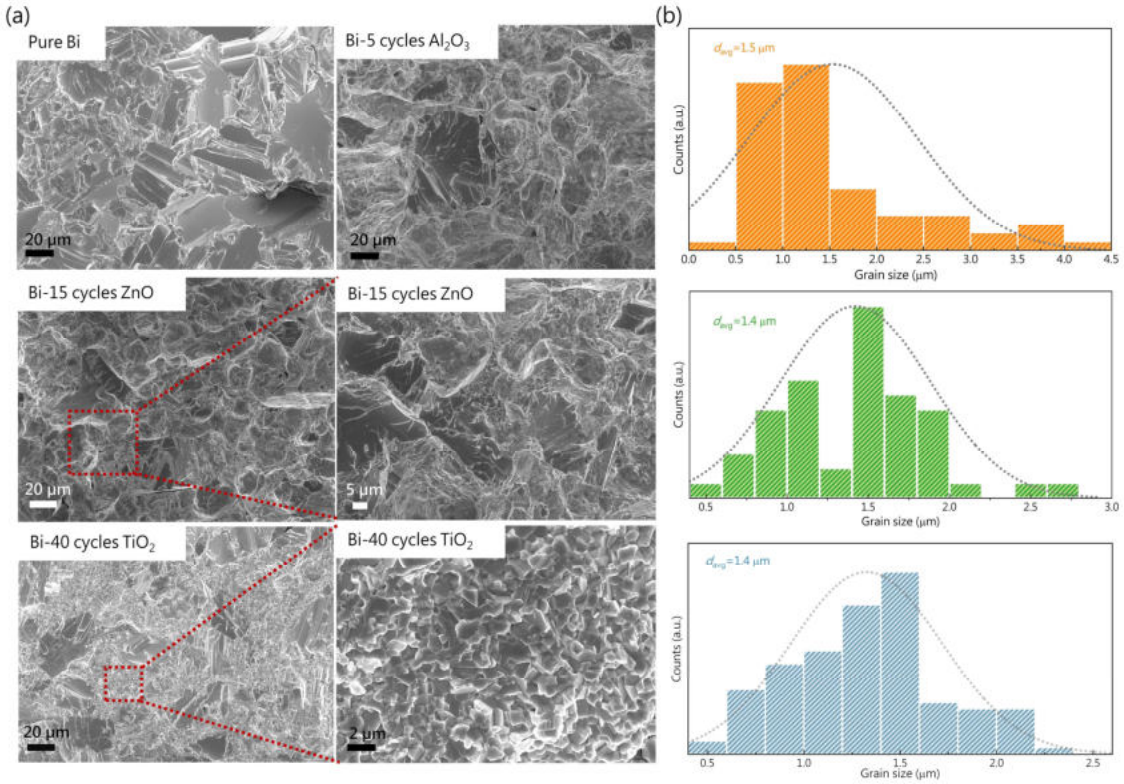

Figure 4-3 *(a) SEM images of the fractured surfaces of pure Bi with deposition of 5 cycles of Al_2O_3, 15 cycles of ZnO, and 40 cycles of TiO_2. (b) The grain size distribution of the coated samples.*

The statistical grain size distributions and area-weighted average grain sizes of the corresponding samples in Figure 4-3(a) are calculated and plotted in Figure 4-3(b), showing an average grain size of ~1.4–1.5 μm for Bi particles coated with Al_2O_3, TiO_2,

and ZnO. High magnification SEM images reveal a plethora of stretch marks on the surfaces of the Bi grains in the Al_2O_3- and ZnO-modified samples, which is particularly intriguing since it indicates that the existence of coated films might impede the expansion of Bi grains during the sintering process, as marked with yellow arrows in Figure 4-4(a). It should be emphasized that no stretch marks were detected in samples coated with fewer than 10 cycles of Al_2O_3 and ZnO or any of the TiO_2-coated samples. The observed phenomena become more prominent as the coating layer thickness increased; i.e., 20 cycles of Al_2O_3 coating exhibited greater resistance to the expansion of Bi grains, resulting in the squeeze of Bi from such stretch marks, as illustrated by the pink arrows in Figure 4-4(a). The formation of these stretch marks could be attributed to a difference in the coefficient of thermal expansion (CTE) of the Bi and oxide layers, such as Al_2O_3 and ZnO. Uncoated particles easily form necks and grow once they reach the sintering point of pure Bi (473 K). The presence of oxides with lower CTE delays necking and suppresses Bi grain growth. This outcome can be better explained when CTE values reach 16.7×10^{-6}/K, 6.1×10^{-6}/K, 3.1×10^{-6}/K, and 3.5×10^{-6}/K, for Bi, TiO_2, Al_2O_3, and ZnO, respectively[125–127]. This type of inhibition of grain growth was also observed by Kim *et al.*[88] when $Bi_{0.4}Sb_{1.6}Te_3$ particles were coated with a ZnO thin layer. The low movement energy of oxides at the sintering process temperature, which can be attributed to the large difference between the melting point of oxides and matrix, might hinder Bi grain growth. The amorphous Al_2O_3 layers also can be observed in TEM images (Figure 4-4(b)).

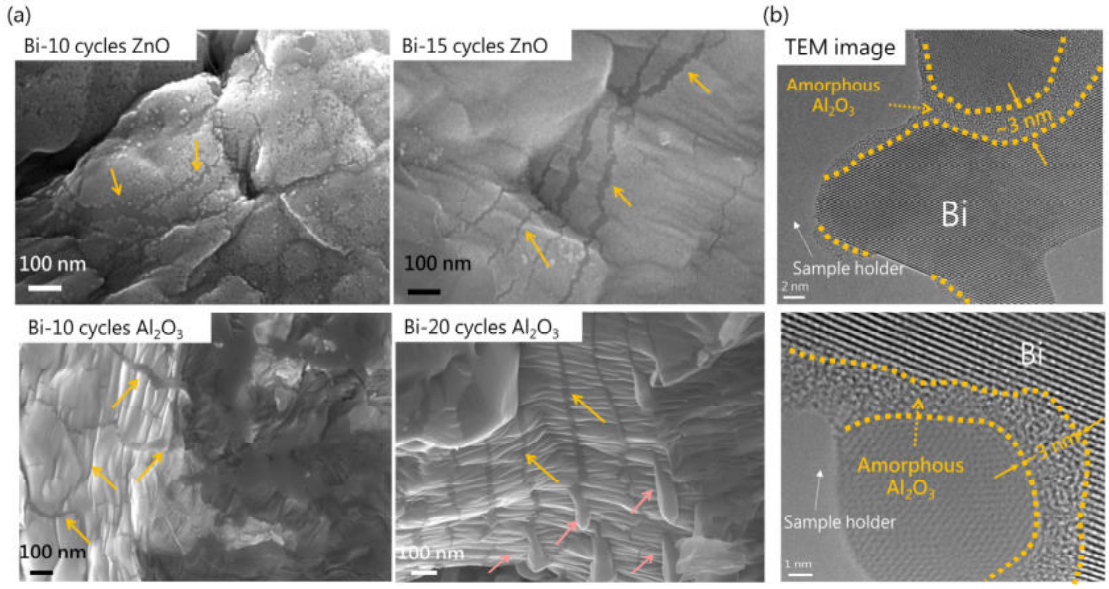

Figure 4-4 *SEM images of stretch marks in Bi grains after ALD of (a) 10 cycles ZnO, (b) 15 cycles ZnO, (c) 10 cycles Al_2O_3 and (d) 20 cycles Al_2O_3. (e) TEM images of 5 cycles Al_2O_3 coated Bi.*

4.2.3 Effect of ALD surface modification on the TE properties of Bi

The deposition of oxide layers on the surface of Bi particles has a significant effect on electrical transport, as explained by energy filtering phenomena. According to this mechanism, the established barrier produced by the coating layers could result in a decrease in the n and an increase in S. The temperature-dependent S and σ of the Al_2O_3-, TiO_2-, and ZnO-coated samples are shown in Figure 4-5.

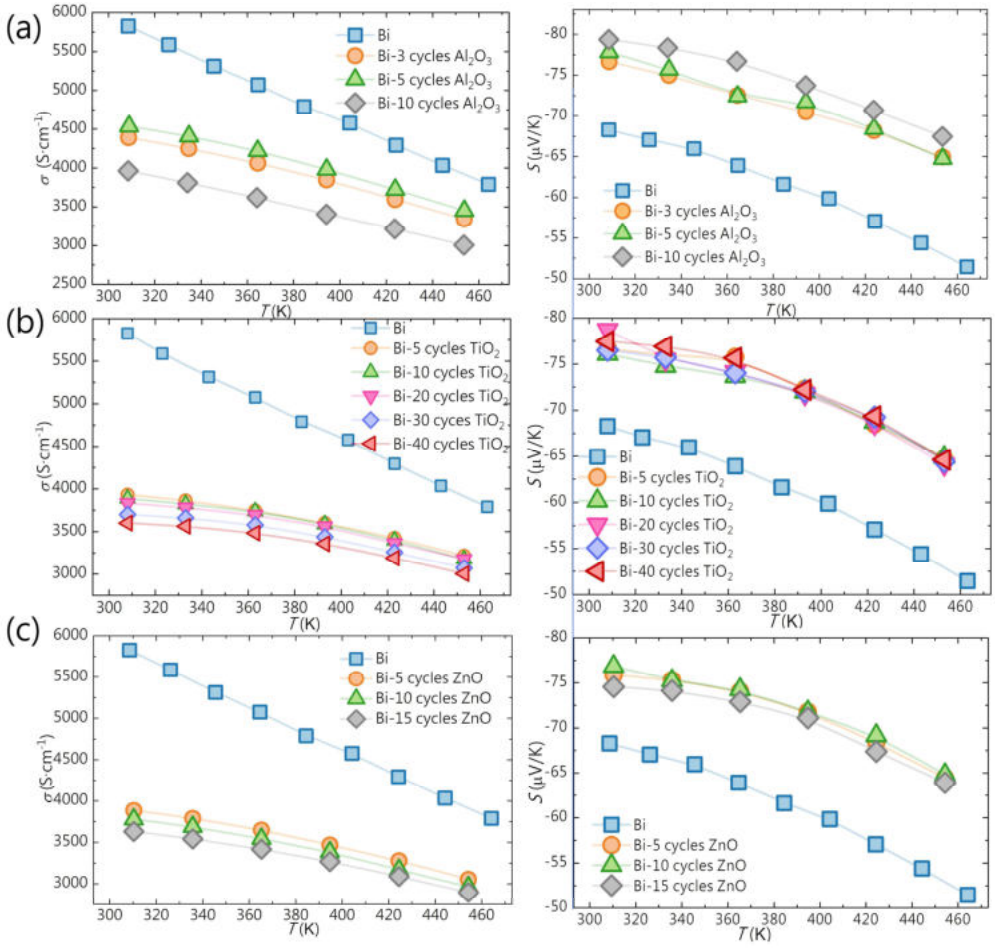

Figure 4-5 *Temperature dependence of the (a) σ, (b) S, and (c) PF of the Bi samples with different cycles of Al_2O_3-, TiO_2-, and ZnO-coated samples.*

An S of ~-68 μV/K at 300 K was obtained for pristine Bi, which is slightly higher than that reported in the literature (-60 μV/K)[128]. In addition, the obtained data showed a considerably lower σ of ~5900 S/cm at 300 K than that for polycrystalline Bi (10000 S/cm)[128]. This inconsistency might originate from the finer Bi grain size used in this study. For all of the coated samples, the negative S indicates n-type conduction, which decreases with increasing temperature, showing metal electrical conduction behavior. A considerable increase in the S of all of the coated samples was observed even after a

few ALD cycles. This increase is more pronounced when Al_2O_3 is deposited in such a way that, after three ALD cycles, the absolute S can reach 76 μV/K at 300 K and be augmented by increasing the number of ALD cycles. However, for TiO_2- and ZnO-coated Bi samples, the absolute S was enhanced after five ALD cycles, and adding more cycles did not result in a further increase in the S value. This outcome indicates that the main charge carrier scattering phenomena occurred after a few ALD cycles. A negligible change in the S of other TE materials with an increasing number of ALD cycles of other oxides has been reported previous[55]. As shown in Figure 4-5, the σ of coated samples with different oxides dramatically and continuously decreased when the number of ALD cycles increased. For Bi coated with five ALD cycles of TiO_2 and ZnO, this reduction is from ~5800 (for pure Bi) to ~3950 and ~3900 S/cm, respectively, demonstrating that the oxide coating has a significant influence on the manipulation of the electrical properties.

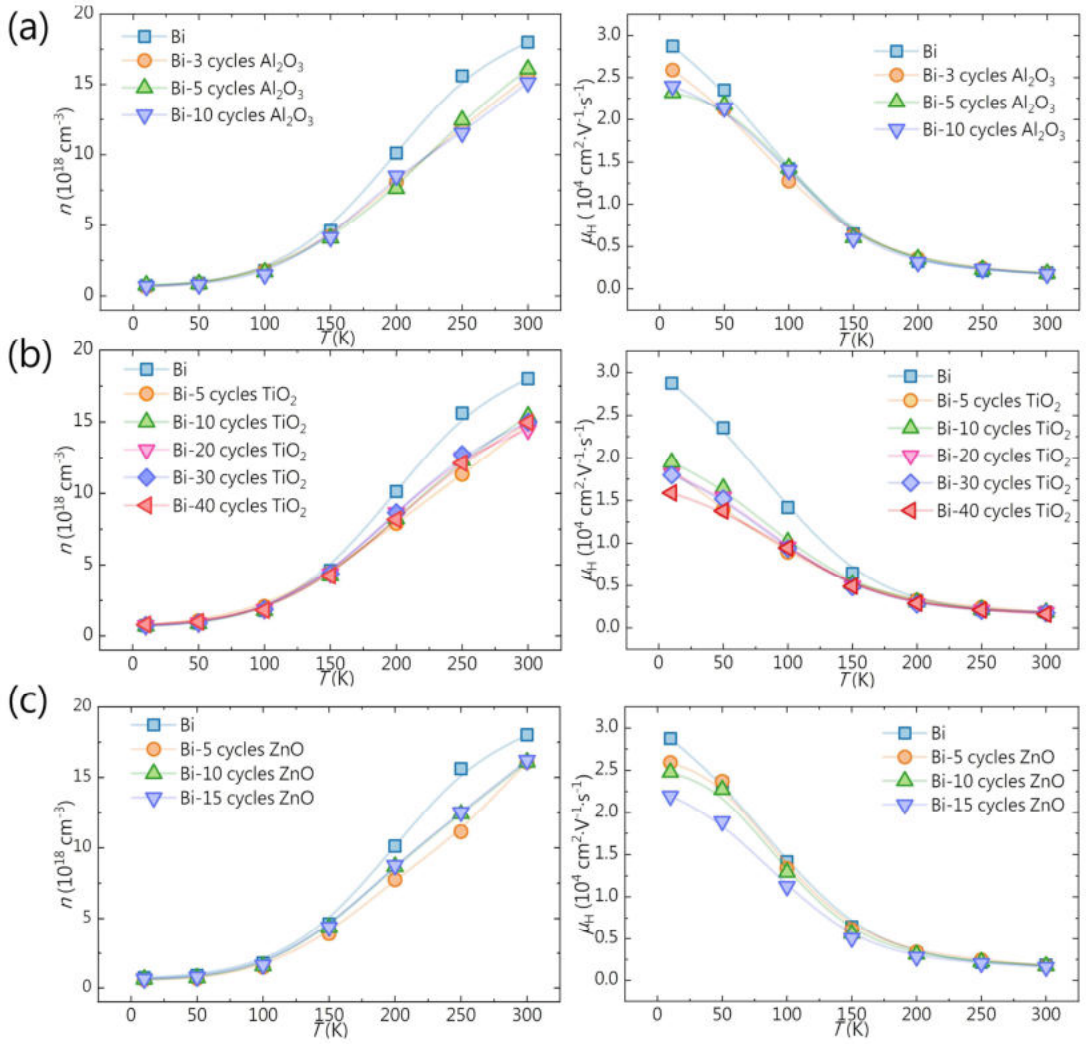

Figure 4-6 *Temperature dependence of (a) the n and (b) the μ_H of the Bi samples with different cycles of Al_2O_3, TiO_2, and ZnO coated samples.*

The variation in electrical properties can be understood through the Hall measurement performed in the temperature range of 10–300 K. As demonstrated in Figure 4-6(a) and (b), n was augmented with temperature, whereas μ_H decreased for all samples, resulting in increased electrical resistivity as temperature increased. This resistivity augmentation with temperature indicates that all of the samples are semimetals, as evidenced by prior research[111]. The variations in μ_H and n in the analyzed samples are also consistent with previous research[129]. The n of all coated samples was not changed by increasing the cycle numbers in the lower temperature range (10–150 K), while their μ_H decreased significantly in the same temperature range, proving that the impurity scattering induced by coating layers mainly affects the μ_H in the lower temperature region. At elevated temperatures (> 150 K), the observed discrepancy between the μ_H values of coated and uncoated samples disappeared, while it became more pronounced for n.

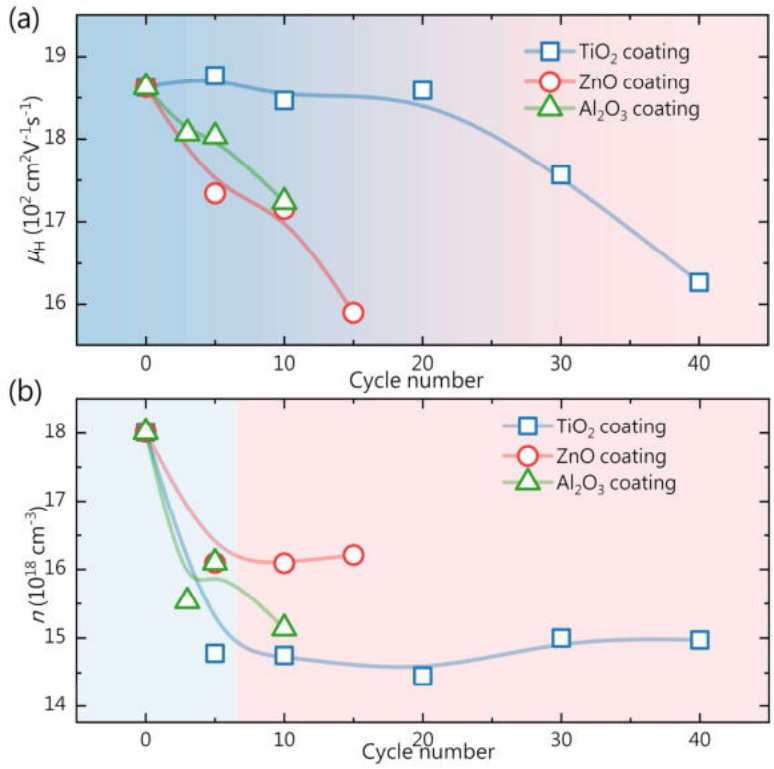

Figure 4-7 *The cycle number dependence of (a) μ_H and (b) n for Al_2O_3-, TiO_2- and ZnO-coated samples at 300 K.*

For a better understanding of the effects of each type of coating and cycle number on electrical transport, the derived results from the Hall measurement at 300 K are summarized and presented in Figure 4-7(a). The μ_H decreases monotonically when the number of Al_2O_3, TiO_2, and ZnO coating cycles increases. The decreasing trend in μ_H matches well with the GPC of each oxide. Among the three coating layers, the ZnO

layers possess a much larger GPC; thus, the rate of decrease in μ_H for ZnO-coated samples is greater than that of the other two. The low GPC of TiO_2 leads to a slower reduction rate in μ_H compared with two other systems within the same cycle number. However, the oxide coating has a distinct effect on n compared to μ_H, behaving in two steps. First, the n decreases significantly with fewer ALD cycles of oxides, and then a further increase in the number of ALD cycles will be profitless in terms of n variation (> 5 cycles), as illustrated in Figure 4-7(b). From the same graph, it can be noted that various oxide coatings lead to different effects on the n. Fewer ALD cycles of Al_2O_3 cause a continuous reduction in n from 18.1×10^{18} cm^{-3} to 15.5×10^{18} cm^{-3}, and a constant value of n in a greater number of cycles can be expected. However, for ZnO- and TiO_2-coated samples, after the first five ALD cycles, the n values reached a plateau. For instance, after 5 cycles of TiO_2, the n immediately dropped from 18.1×10^{18} cm^{-3} to 14.7×10^{18} cm^{-3}, followed by a plateau of the obtained values.

Considering the Hall measurement results, it can be concluded that the continuous decrease observed in σ of the coated samples could be attributed to the simultaneous reduction of n and μ_H within the first few ALD cycles (< 5 cycles). By increasing the number of ALD cycles, the observed reduction in σ in ZnO- and TiO_2-coated samples might be derived from the reduction in μ_H since the n remains almost constant. In addition, the increase in S with a low ALD cycle number is due to the decrease in n, while the small variation in S in greater amounts of ZnO and TiO_2 could be attributed to the small change in n. It can be postulated that, as the energy barrier is established by the coating layer, high-energy carriers can pass through, and low-energy carriers will be scattered by the energy barrier. Upon reaching a higher coating thickness, the movement of carriers will be constrained, leading to a continuous decrease in μ_H. However, the constancy of n values as a result of increasing the ALD cycles merits further investigation.

It is expected that, by increasing the oxide layer thickness, high-energy carriers will also be scattered, resulting in a higher S. Nevertheless, a greater content of oxide on the grain surface will be detrimental to σ due to the fast decrease in μ_H (see Figure 4-6). This phenomenon also can be found in other TE materials, such as Mg_2Si[130] and Mg_3Sb_2[131,132] with MgO impurity, where the second oxide phase may result in high-resistance grain boundaries and decrease the electrical properties. As shown in Figure 4-5(c), the PF of Bi coated with ten ALD cycles of oxides is slightly less than that of pristine Bi, indicating that the PF is mainly governed by σ in all three systems. Therefore, reaching a reasonable trade-off between σ and S in this work is essential for improving the overall TE performance of Bi.

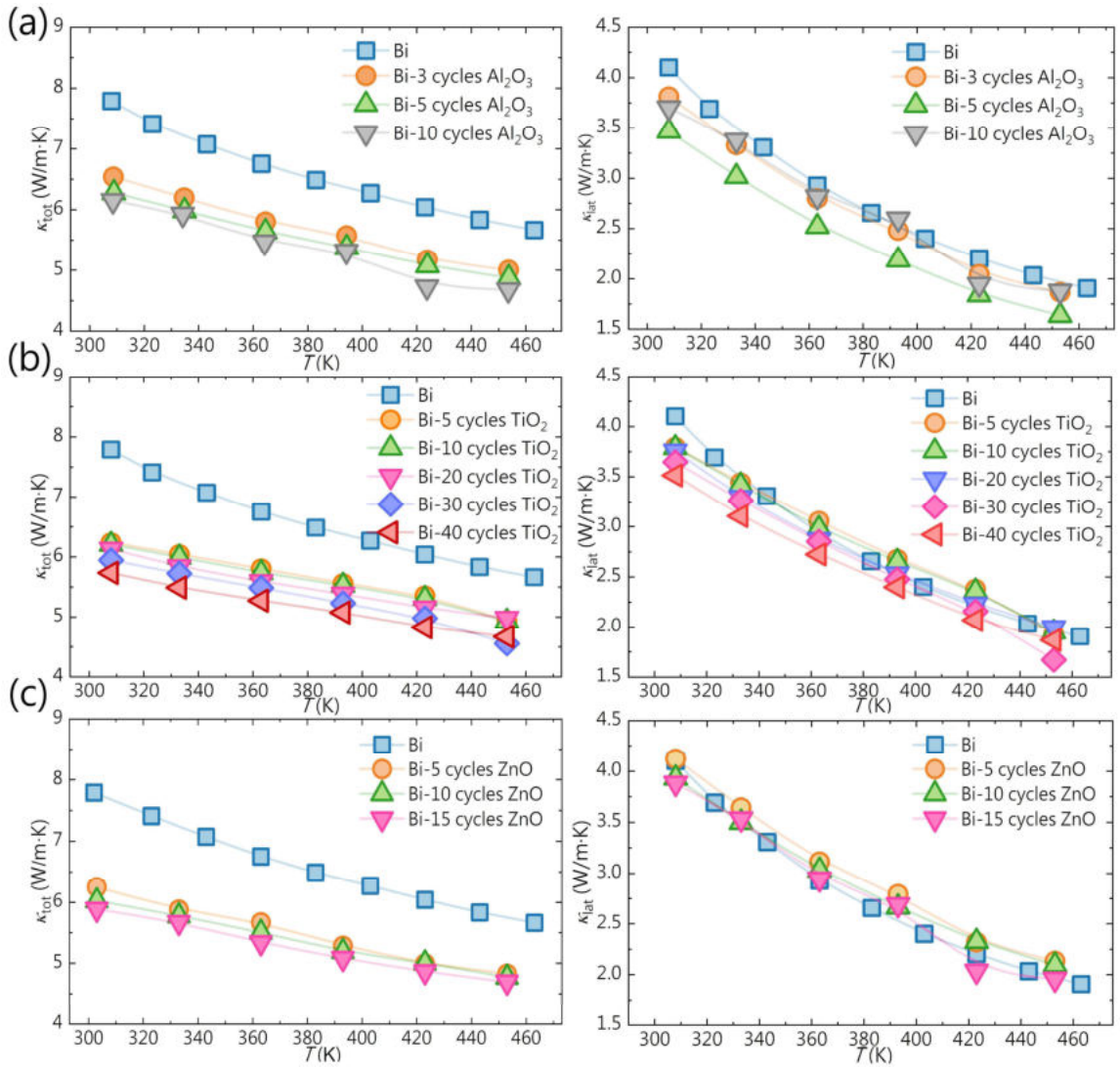

Figure 4-8 *Temperature dependence of the $\varkappa_{tot}$ and $\varkappa_{lat}$ of Bi coated (a)Al_2O_3, (b) ZnO, and (c) TiO_2 layers.*

Figure 4-8(a) shows the temperature dependence of the $\varkappa_{tot}$ of Al_2O_3-, TiO_2-, and ZnO-coated Bi with various oxide thicknesses. With increasing numbers of ALD cycles throughout the complete temperature range, a considerable reduction in $\varkappa_{tot}$ compared to pristine Bi is seen for all three oxides. After three ALD cycles of Al_2O_3, $\varkappa_{tot}$ decreased from 7.78 W/m·K to 6.57 W/m·K, while after five ALD cycles of TiO_2, an approximately 19% reduction in $\varkappa_{tot}$ was observed, indicating that the introduced oxide/Bi heterogeneous interface had a positive effect on the reduction of thermal conductivity. $\varkappa_{tot}$ is the sum of the electronic ($\varkappa_{ele}$) and lattice ($\varkappa_{lat}$) constituents, and their contributions to the total thermal conductivity should be evaluated in detail. The thermal conductivity of the electronic contribution is 3.7 W/m·K, which is ~47.4% of the $\varkappa_{tot}$ of pristine Bi. However, $\varkappa_{ele}$ can be effectively suppressed by interface

modification; i.e., after 5 cycles of ALD of TiO_2, $\varkappa_{ele}$ decreased from 3.7 to 2.4 W/m·K, for almost a 35.1% reduction. Additionally, $\varkappa_{lat}$ can be subtracted from $\varkappa_{tot}$ (Figure 4-8). $\varkappa_{lat}$ also decreased with increasing cycle numbers, although the reduction was not as significant as $\varkappa_{ele}$, reaching 35%. The lower reduction in $\varkappa_{lat}$ compared to $\varkappa_{ele}$ confirms that the observed suppression in $\varkappa_{tot}$ mainly derives from the electronic contribution. Figure 4-9(a) compares the reductions in both lattice and electronic contributions for all of the coated samples, as well as pristine Bi at 300 K. All of the coated samples experienced a tremendous reduction in $\varkappa_{tot}$, while $\varkappa_{lat}$ changed insignificantly.

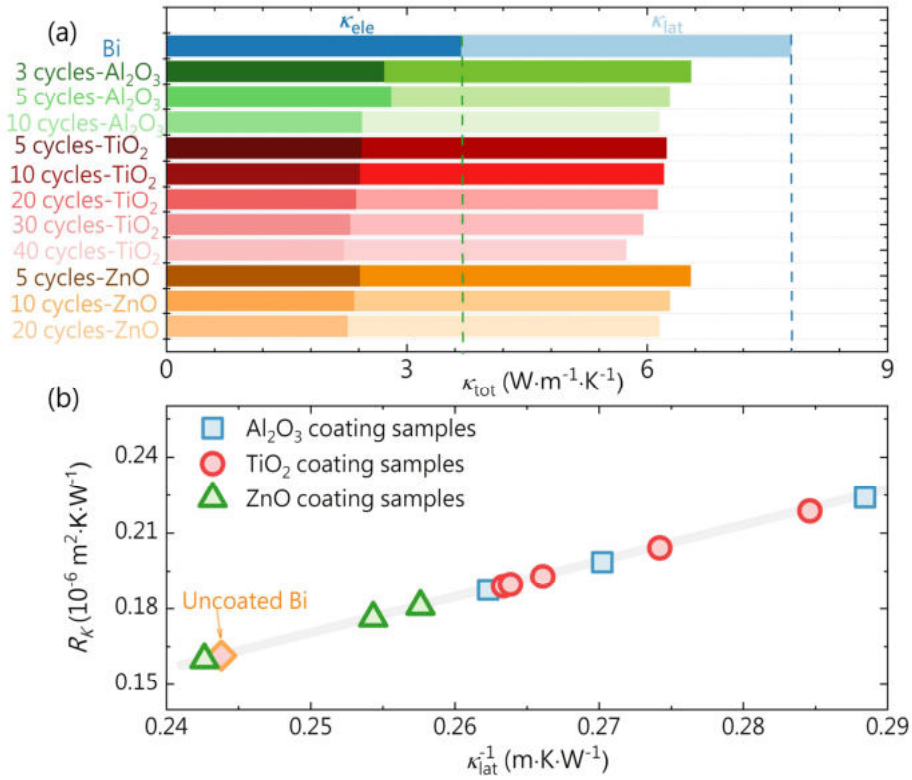

Figure 4-9 *(a) Comparison of $\varkappa_{ele}$ and $\varkappa_{lat}$ among the Al_2O_3-, TiO_2-, and ZnO-coated samples with different cycles at 300 K. (b) The $1/\varkappa_{lat}$ and calculated R_K of the Al_2O_3-, TiO_2-, and ZnO-coated samples at 300 K.*

To evaluate the effect of the microstructure and the grain boundary components (matrix and oxide coating), the interfacial thermal resistance/Kapitza resistance (R_K) can be calculated. The Kapitza resistance in this model includes contributions from the matrix (Bi), as well as an additional contribution from the heterogeneous grain boundary. The thermal lattice conductivity of coated and pristine Bi is fitted to $\frac{1}{\varkappa_{lat}} = \frac{1}{\varkappa_{Bi}} + \frac{R_K}{d_{avg}}$, where d_{avg} is the average grain size defined by SEM, $\varkappa_{Bi}$ is the total thermal conductivity of Bi, and R_K is the Kapitza resistance reflecting the grain boundary contribution for the reduction of $\varkappa_{lat}$[57]. The values of $1/\varkappa_{lat}$ for Al_2O_3-, TiO_2-,

and ZnO-coated samples were calculated to confirm the effectiveness of the fitting model, as shown in Figure 4-9(b). Here, an average grain size of 1.4 μm is used for the fitting. All of the data exhibit linear fitting, and the fitting results agree well with the experimental results. Compared with ZnO-coated samples, the Al_2O_3 and TiO_2 coating layers have a more effective influence on decreasing $\varkappa_{lat}$. For instance, the interfacial Kapitza resistance of 40 cycles of TiO_2 can reach 0.21×10^{-6} $m^2\cdot K\cdot W^{-1}$, which is higher than the 0.177×10^{-6} $m^2\cdot K\cdot W^{-1}$ of 10 cycles of ZnO coating. In summary, the R_K values of the coated samples increased with the increasing cycle number, which could be ascribed to the increasing thickness of the oxide layer and the enhanced phonon scattering manipulated intentionally using the powder ALD technique.

Although there is little deterioration of the *PF* of the samples coated with Al_2O_3, TiO_2, and ZnO, the significant decrease in $\varkappa_{tot}$ overcompensates for that reduction and results in a significant improvement of zT (Figure 4-10). Figure 4-1(d) demonstrates the temperature-dependent zT of the optimized samples. The zT value of Bi increased by approximately 40% and reached a peak of 0.15 after five ALD cycles of Al_2O_3 in the entire temperature range of 300–453 K. Additionally, the maximum zT values shifted to high temperatures compared with pristine Bi. It is worth noting that the average zT at all measured temperatures increased from 0.11 to 0.14 after five ALD cycles of Al_2O_3 (Figure 4-1(b)), implying that Bi surface modification by ALD of the studied oxides in such a wide temperature range is favorable for the energy harvest device in the near-room temperature region.

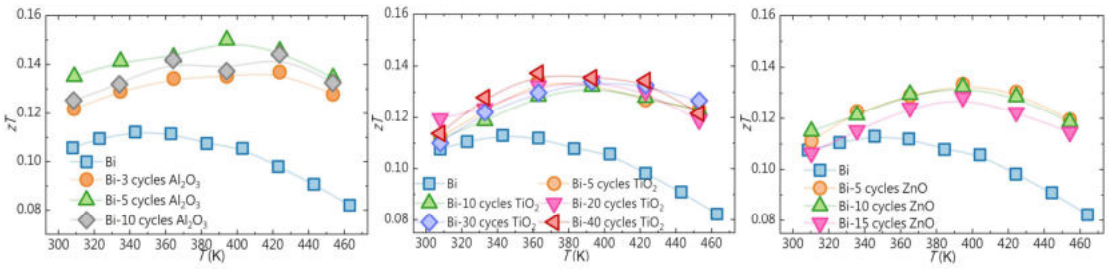

Figure 4-10 *Temperature dependence of the zT of the Bi samples with different cycles of Al_2O_3-, TiO_2-, and ZnO-coated samples.*

4.3 The influence of newly developed Sb_2O_5 layers on TE properties

As previously mentioned, powder ALD has been used effectively in a variety of traditional TE materials systems. In all these investigations, the values of $\varkappa_{tot}$ were unprecedentedly suppressed using TiO_2, Al_2O_3, and ZnO coating layers due to their

brilliant chemical stability and developed deposition process[52,54,55,87,89]. However, if further suppression of $\varkappa_{tot}$ in TE matrices is desired, one of the main challenges that must be addressed is the development of novel coating layers.

4.3.3 New developed Sb_2O_5 ALD films

The deposition of Sb_2O_5 thin films by ALD technique only was reported using $SbCl_5$/water deposited at 773 K and $Sb(NMe_2)_3/O_3$ deposited at 393 K[133,134]. Herein, by using a new precursor combination of $SbCl_5$ as an antimony reactant and H_2O_2 as the oxidizer, we deposited Sb_2O_5 at a low deposition temperature of 373 K.

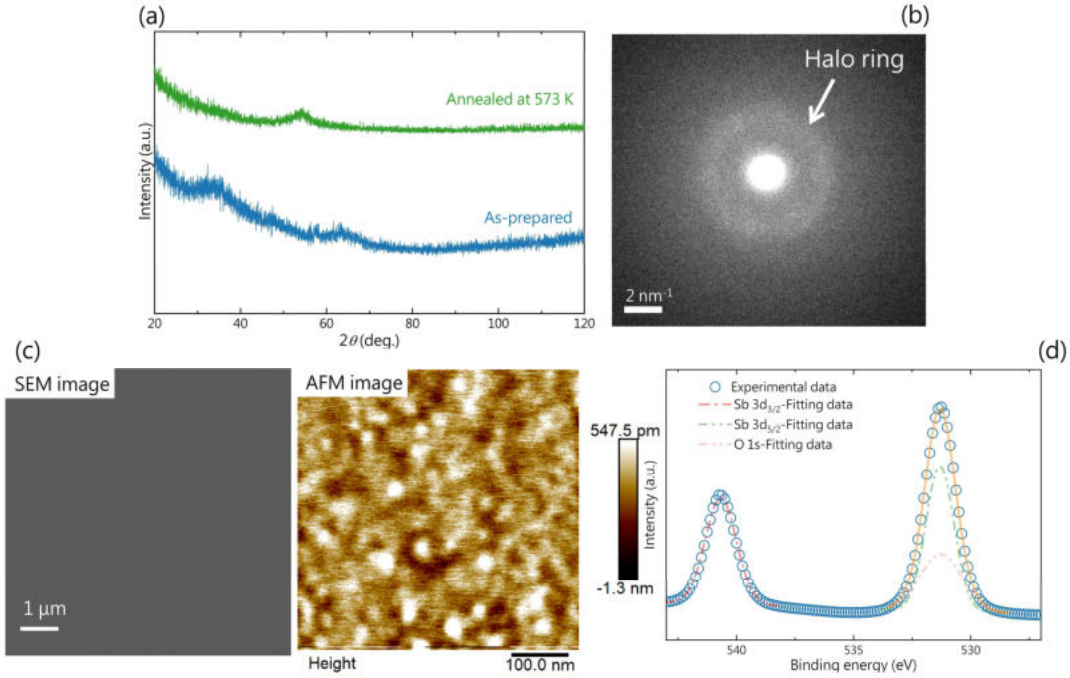

Figure 4-11 *(a) The GIXRD pattern of as-prepared Sb_2O_5 film and annealed Sb_2O_5 film at 300 ◦C for one hour. (b) TEM image and SAED patterns of amorphous Sb_2O_5 revealing the characteristic halo ring pattern. (c) The SEM and AFM image of Sb_2O_5 film morphology. (d) The XPS spectra of Sb_2O_5 thin film.*

The uniform amorphous Sb_2O_5 film was deposited on the Si-SiO_2 wafer as confirmed by SEM, TEM, and GIXRD, as presented in Figure 4-11(a) and (b). Sb_2O_5 film was annealed in Argon environment at 573 K for one hour to assess the stability of the deposited film. There was no thickness loss and an apparent crystalline peak in the XRD pattern of the annealed sample, demonstrating the film's thermal stability (see Figure 4-11(a)). The shown thermal stability may assure that no crystallization occurs during the sintering of coated powder into the pellet at 473 K. The root mean squared (RMS) value of 1.06 nm derived from atomic force microscopy (AFM) analyses, in conjunction with SEM surface morphology of the Sb_2O_5 films, demonstrates the excellent conformity and smoothness of the deposited films, as seen in Figure 4-11(c).

The XPS spectrum of the Sb 3d/O 1s core line region showed two peaks at 531.3 and 540.7 eV (Figure 4-11(d)). The deconvolution of the spectra located at 531.3 eV showed that there were two components, namely Sb $3d_{5/2}$ and of O 1s, indicating the formation of the Sb_2O_5 phase, while the peak centered at 540.7 eV corresponded to Sb $3d_{3/2}$.

4.3.2 Microstructural characterizations of bulks

The newly developed Sb_2O_5 film was applied on Bi powders in a tumbler within an ALD system. To achieve high homogeneity of coating on Bi particles, three different approaches were applied: i) Prior to the ALD process, the Bi powders were ground using high energy ball milling, resulting in fine and non-agglomerated Bi particles with full exposure of the particle surface to the reactants; ii) the extended exposure time allowed enough time for the ALD reaction on the particles to complete; and iii) using a quartz tumbler as a rotation apparatus with an optimum rotation speed of 2 rpm permitted gases to reach all sides of the particle surface.

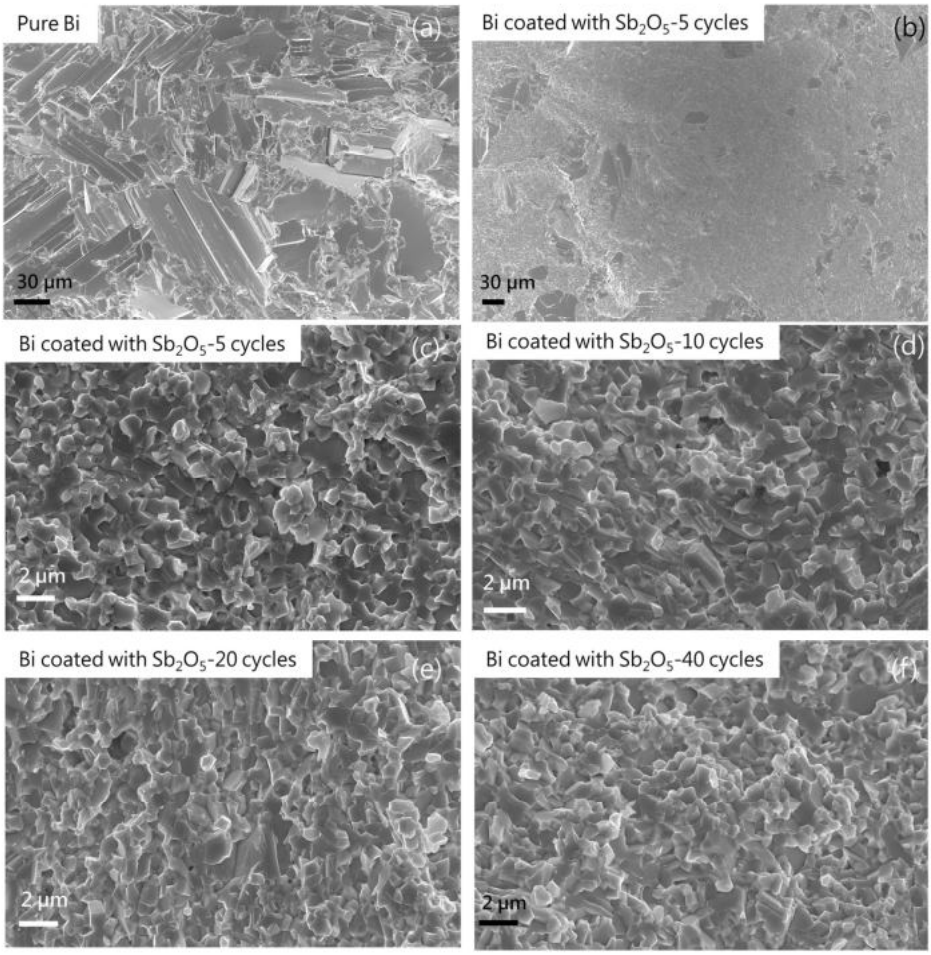

Figure 4-12 *SEM images of the fractured surfaces of (a) pure Bi, (b) Bi after 5 cycles ALD of Sb_2O_5, (c)–(f) higher magnification image of Bi after 5, 10, 20, 40 cycles ALD of Sb_2O_5.*

Figure 4-12 depicts the fractured surface of sintered Bi before and after various cycles of ALD of Sb_2O_5. The pure Bi fractured surface exhibited a transgranular fracture running through the non-preferential oriented coarse particle, as shown in Figure 4-12(a), whereas intergranular fracture is the dominant fracture mode in Bi-Sb_2O_5 samples. The observed transition from transgranular to intergranular fracture mode demonstrates the strong influence of surface modification on the morphology and grain growth of sintered Bi particles, mostly suppressing Bi grain size (Figure 4-12(b)-(f)). Similar behavior was observed when TiO_2 coatings were applied to Bi particles[52]. The particle size distribution histogram shows an average grain size of 1.4 μm for Bi coated with 5 cycles of Sb_2O_5 (Figure 4-13). The modest fluctuation observed in the average grain size as the cycle number increases indicates that tuning behavior on the microstructure occurred even after a few ALD cycles (see Figure 4-13).

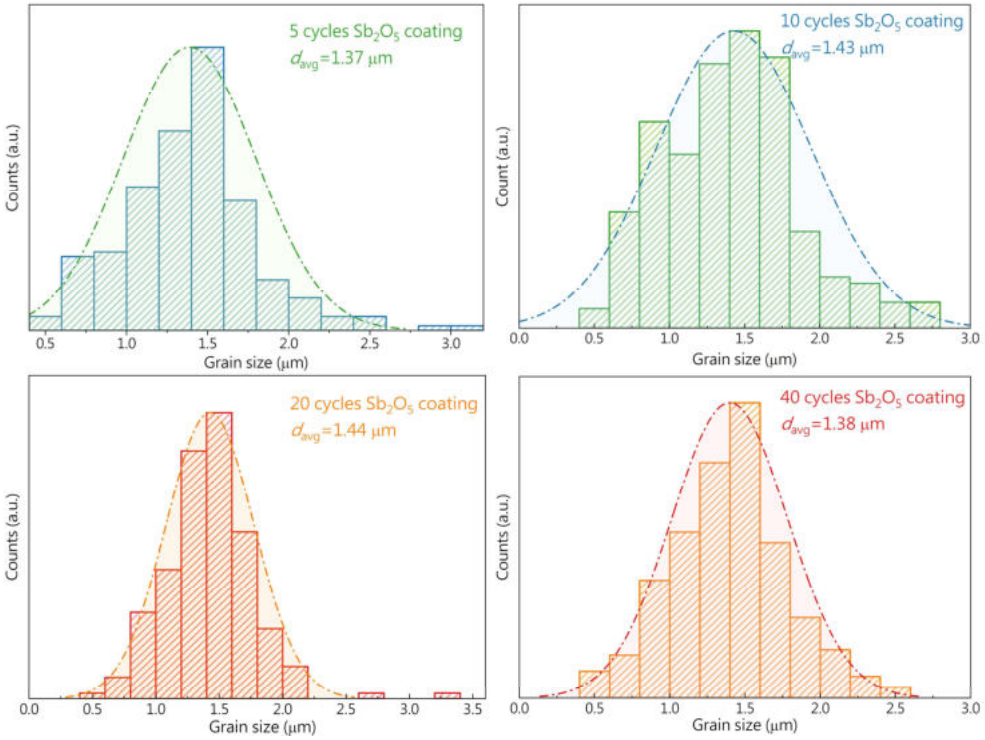

Figure 4-13 *Grain size distribution of Bi samples with different ALD cycles of Sb_2O_5.*

The difference in the coefficients of thermal expansion (CTE) of the Bi and oxide layers might explain the observed decrease in particle size. When uncoated Bi particles reach their sintering point (473 K), they rapidly form necks and grow, but the addition of oxides with lower CTE delays necking and suppresses Bi grain growth. It is worth mentioning that no contaminants (such as bismuth oxides) were detected in the XRD patterns of bulk pellets (Figure 4-14), suggesting that no substantial oxidation occurred during the powder ALD coating process, even using strong oxidant of H_2O_2 in ALD process.

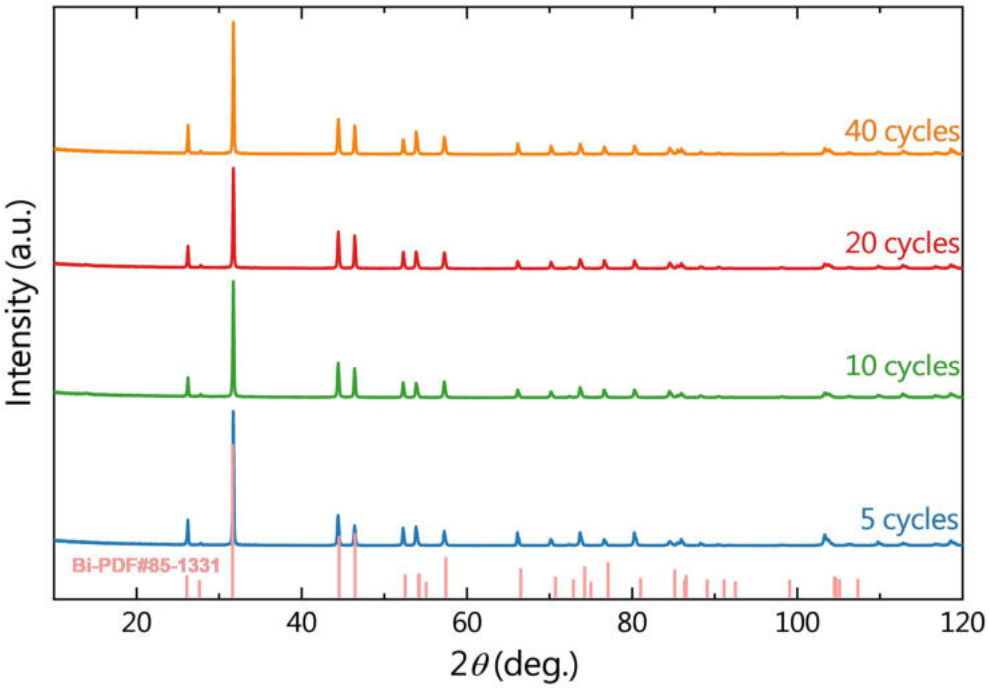

Figure 4-14 *XRD patterns of Bi samples with different ALD cycles of Sb_2O_5.*

4.3.3 Effect of ALD surface modification on the TE properties of Bi

The temperature dependency of the $\varkappa_{tot}$ of Sb_2O_5-coated Bi samples is shown in Figure 4-15(a). As can be observed, the $\varkappa_{tot}$ of the samples is significantly reduced by Sb_2O_5 coating. Increasing the ALD cycle numbers over the whole temperature range results in a constant reduction of $\varkappa_{tot}$ compared to the pristine Bi. By comparing the $\varkappa_{tot}$ of Sb-doped Bi single or polycrystals[129,135–139] to the $\varkappa_{tot}$ of 20 cycles Sb_2O_5 coated Bi sample in Figure 4-15(b), it is fair to conclude that coating of Bi particles can result in a reduction of $\varkappa_{tot}$ comparable to the doping effect in $Bi_{0.88}Sb_{0.12}$ polycrystal[137] and $Bi_{0.926}Sb_{0.074}$ single crystal[110]. This remarkable performance in reducing Bi thermal conductivity shows that the ALD technique has a favorable effect on optimizing thermal transports without the need for doping elements. The large reduction in $\varkappa_{tot}$ is due to two factors: i) the contribution of phonon scattering, and ii) the decrease in $\varkappa_{ele}$[35].

In terms of $\varkappa_{lat}$, the introduced oxide/Bi heterogeneous interface mainly scatter phonons from short to long wavelengths more efficiently than normal grain boundaries. Figure 4-15(c) depicts the temperature dependency of the $\varkappa_{lat}$ of Sb_2O_5-coated Bi with various ALD cycle numbers. It can be seen that as the cycle number increases, the $\varkappa_{lat}$ decreases over the whole temperature range examined, with a huge reduction of 21.5% achieved after 20 ALD cycles of Sb_2O_5. Figure 4-15(d) summarizes the decrease of $\varkappa_{lat}$ of Bi samples with various types of the coating layer, revealing that just 5 cycles of Sb_2O_5

lead to the maximum reduction (16%) among all studied oxide layers. This variation on the $\varkappa_{lat}$ with different coating layers might be ascribed to R_K. Based on earlier research[140], more R_K might be produced due to extra phonon scattering centers at the grain boundaries, and a simple model for thermal conduction was proposed to understand the effect of the Bi/Sb_2O_5 interfaces.

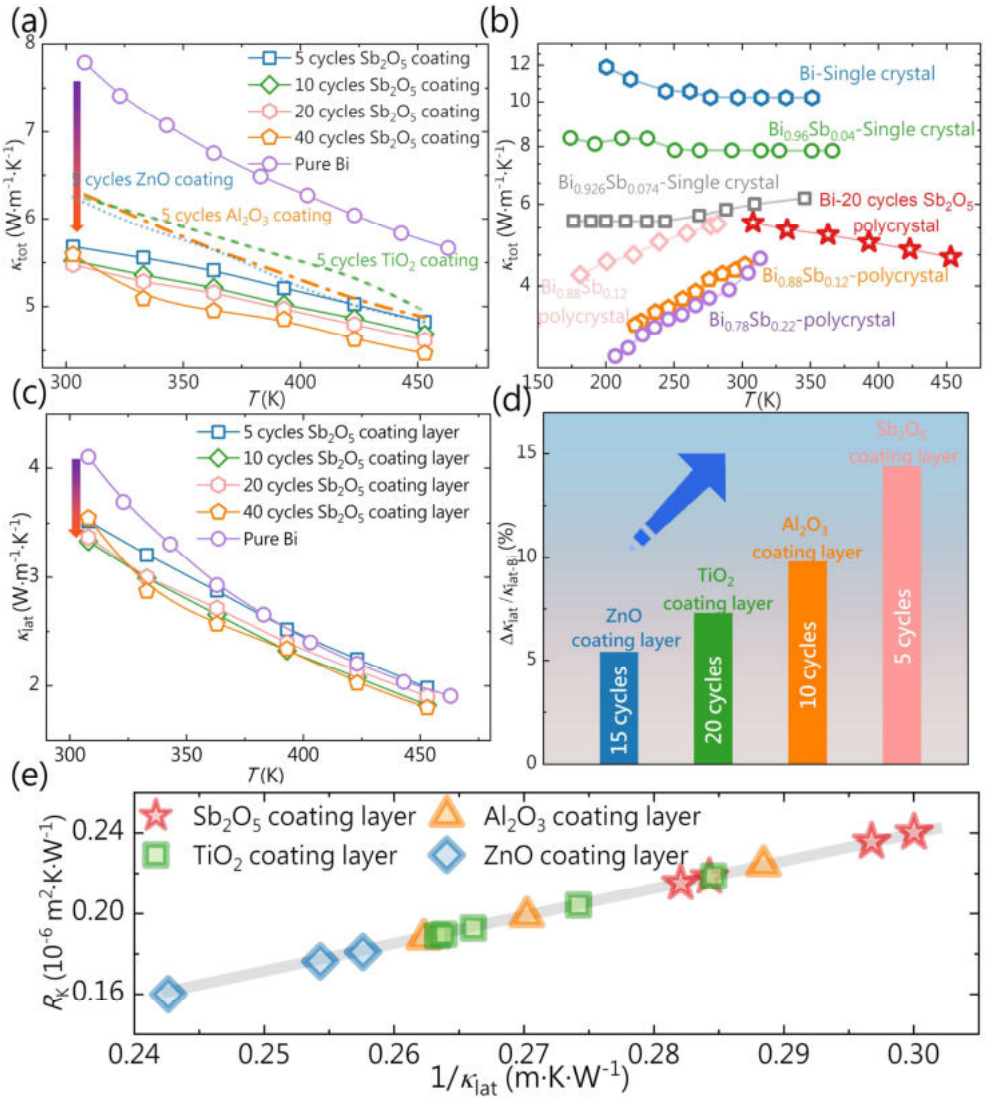

Figure 4-15 *Temperature dependence of(a) $\varkappa_{tot}$, (b) $\varkappa_{tot}$ of Sb_2O_5-Bi sample with Sb-doped Bi single crystals and polycrystals*[129,135–139]*, (c) Temperature dependence of $\varkappa_{lat}$ of Bi coated with different ALD cycles of Sb_2O_5, (d) $\Delta\varkappa_{lat}/\Delta\varkappa_{lat\text{-}Bi}$ of Sb_2O_5-coated Bi compared to that of Al_2O_3-, TiO_2-, and ZnO-coated Bi. (e) $1/\varkappa_{lat}$ vs calculated R_K for Al_2O_3-, TiO_2-, ZnO- and Sb_2O_5-coated Bi samples at 300 K*[52]*.*

By plotting the $\varkappa_{lat}$ at 300 K with different Sb_2O_5 coating layers as a function of R_K[89], it is found that all the data fit well with the predicted curve calculated through the model using d=1.4 μm as determined by SEM image (Figure 4-12). For the Bi coated with different cycle numbers, the R_K increases from 0.2 to 0.24 × 10^{-6} m^2K/W as the

number of cycles increases (Figure 4-15(e)), revealing the regulation of phonon transport by the thickness of Sb_2O_5 layers at Bi grain boundaries. Furthermore, the Sb_2O_5 layer has the highest R_K among all studied oxide layers, implying that the Sb_2O_5 layers on grain boundaries are more effective in modifying thermal characteristics.

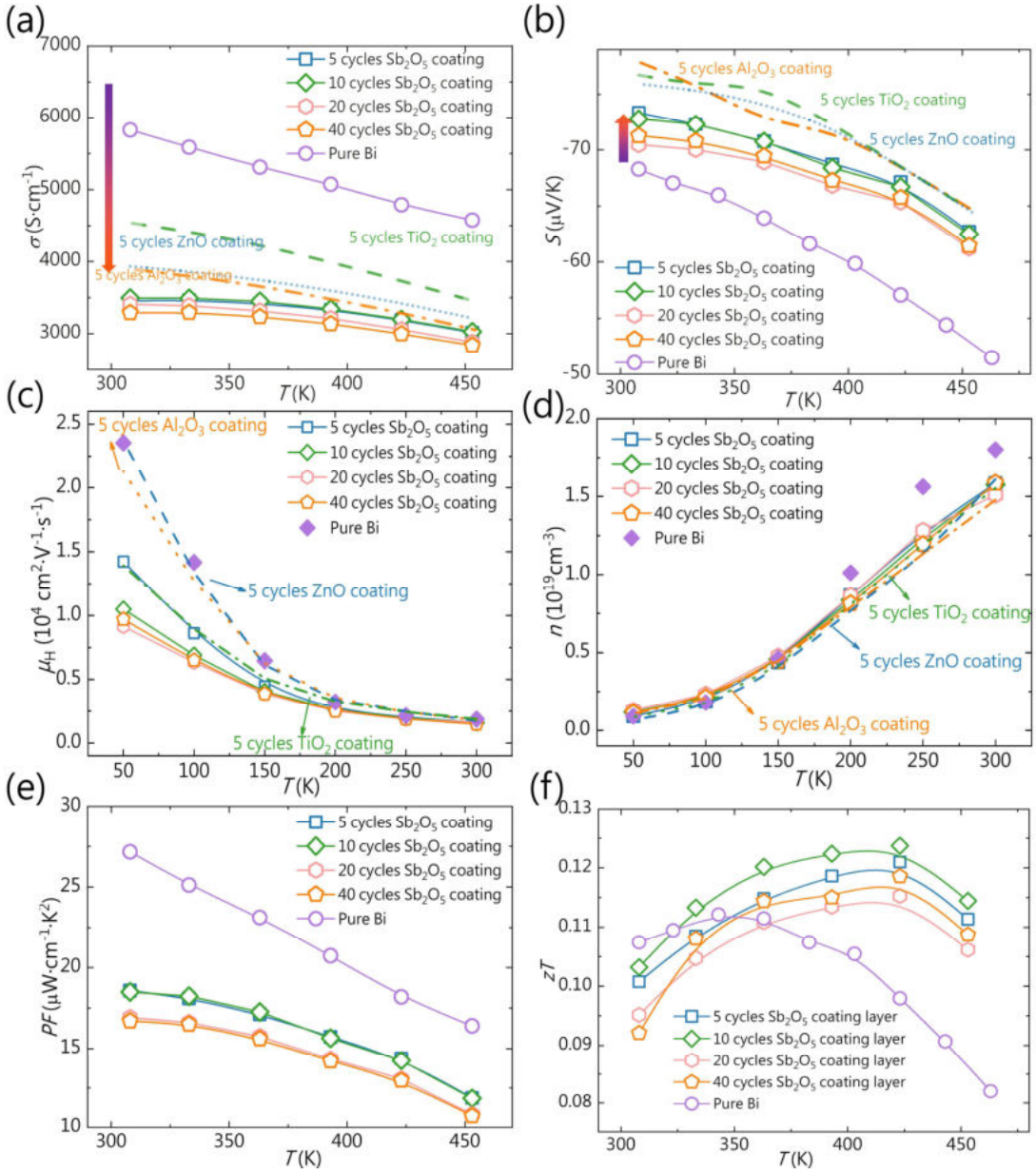

Figure 4-16 *Temperature dependency of (a) σ, (b) S, (c) μ_H, (d) n, (e) PF, and (f) zT for Bi coated with different ALD cycles of Sb_2O_5. Reported data for different types of oxide layers are also included for comparison*[52].

Despite the fact that the inclusion of Sb_2O_5 coating layers results in a significant decrease of $\varkappa_{lat}$, it is well known that the oxide compounds scattered on the grain boundaries can degrade the electrical characteristics, as reported for Mg_2Si- and Mg_3Sb_2-based materials containing MgO as an impurity[130,131]. Therefore, it is critical

to comprehend how the thickness of Sb_2O_5 affects the carrier transport characteristics. Figure 4-16(a)–(b) illustrate that in all Sb_2O_5 modified Bi samples, σ decrease and $|S|$ increase as the ALD cycle number increases. Compared to pure Bi, σ decreases by ~ 29.5 % and $|S|$ augment ~9% (from 66 to 73 μV/K), respectively at 300 K, indicating strong carrier scattering at the Bi/Sb_2O_5 interface. Hall measurements at 10–300 K were used to assess the apparent increase in S and decrease in σ values (Figure 4-16(c) –(d)). In the low-temperature area (< 150 K), there is a substantial reduction in μ_H, while n changes slightly, showing that the oxide layer mostly impacts μ_H at low temperatures, as previously reported[52]. According to the 300 K data, both n and μ_H reduce dramatically even after a few ALD cycles (5 cycles) of Sb_2O_5, with n approaching a constant value and μ_H decreasing as the number of ALD cycles increases (Figure 4-17(a)–(b)). When compared to other oxide coatings, the effect of Sb_2O_5 on decreasing the μ is substantially stronger, while its effect on decreasing the n is slightly weaker, resulting in lower S and σ. Changes in electrical properties have a substantial impact on the considerable reduction of $\varkappa_{ele}$, which is the main component of $\varkappa_{tot}$ decrease. Despite the little loss in PF (Figure 4-17(e)), the highest value of zT increases for all coated samples, with the zT peak relocated to 423 K, making the Bi-Sb_2O_5 system more appropriate for near-room-temperature TE devices (Figure 4-17(f)).

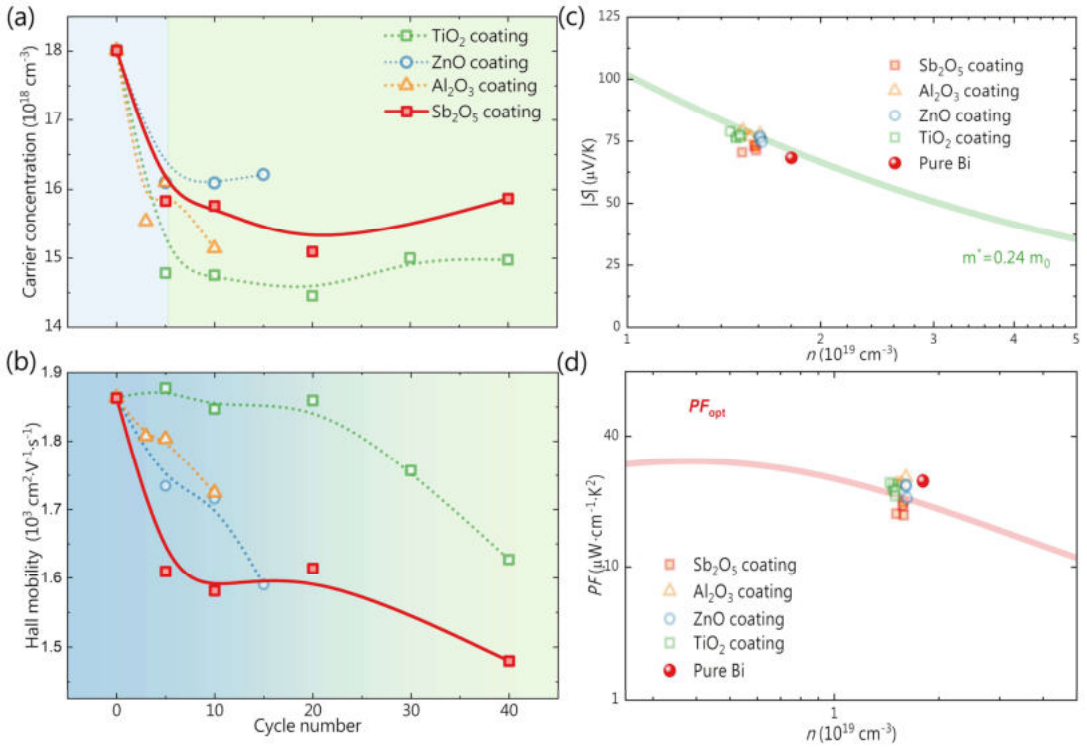

Figure 4-17 *(a) ALD cycle number dependence of n for Sb_2O_5-coated samples at 300 K. (b) ALD cycle number dependence of μ_H for Sb_2O_5-coated samples at 300 K. (c) n dependence of experimental |S| and calculation results at 300 K. (d) calculated optimum PF and experimental results at 300 K for the samples.*

Based on the Hall measurement and electrical measurement results, we plotted the n as a function of the absolute S in Figure 4-17(c) together with Equation (2-13)–(2-17) to evaluate the effective mass m^*, using the SPB model, which is estimated to be $0.24m_e$. Figure 4-17(d) shows the n-dependent optimum PF of samples at 300 K following an SPB model, together with our experimental results. Clearly, there is great potential to further improve the power factor by further reducing the n. Therefore, other approaches are sought to further enhance TE performance of Bi.

5

Chapter 5 Precision interface engineering of CuNi alloys by multilayers of powder ALD

The majority of the presented results in this chapter have been prepared in the following article:

Shiyang He, Amin Bahrami*, Chanwon Jung, Xiang Zhang, Ran He, Zhifeng Ren, Siyuan Zhang, Kornelius Nielsch*, Precision Interface Engineering of CuNi Alloys by Powder ALD Toward High Thermoelectric Performance. ***Advanced Functional Materials* (*Under reviewed*)**

5.1 Introduction

The selection criteria for ideal ALD layers to obtain higher zT values have not been well investigated in previous works for a single kind of oxide coating. In terms of electrical properties, the resistivity (ϱ) and thickness of the coating layers (x) are vital for electrical conduction between phase boundaries. The lower ϱ of the coating layers may relieve the degradation of the overall electrical conductivity, but it is difficult to avoid because of the low conductance between the phase boundaries. Additionally, thicker coating layers could benefit scatter carriers, resulting in an increase in S, but there is a tremendous loss of electrical conductivity. Therefore, a lower ϱ and higher thickness of the coating layer are expected. In terms of thermal properties, the x and $\varkappa$ of the oxide coating layer are important for thermal conduction between phase boundaries. A larger x indicates a higher Kapitza resistance introduced by the oxides, which could more effectively scatter phonons compared with normal grain boundaries. However, the thermal conduction path may be formed if x is too large due to the well-known high $\varkappa$ of oxides.

In addition to the above parameters, the complexity of the coating layers has rarely been explored in previous work and may play an important role in modifying the properties of the coating layers. Due to the layer-by-layer growth mode, the multiple-layer structure could be constructed on the surface of the powder. As reported in

references of ALD thin films, inserting TiO_2[141], HfO_2[141], or Al_2O_3[142] into ZnO layers with multiple-layer structures could significantly reduce the ϱ compared with pristine ZnO. The doping effect of Al results in an increase in n in the oxide layers. Therefore, introducing multiple-layer structures on the surface of powders could increase the complexity of the layers. This benefits electrical and thermal transport simultaneously: i) the decreased ϱ of the coating layers allows us to deposit a higher thickness of layers, which may enhance S and maintain PF (PF=S^2/ϱ). ii) The increased complexity could induce stronger phonon scattering compared with a single kind of oxide coating.

Herein, we employ ALD-based interface modification to optimize the thermal and electrical transport properties of a CuNi thermoelectric material in an attempt to decouple the thermoelectric parameters. The effect of a single layer of ZnO and Al_2O_3 oxides and multilayers of ZnO/Al_2O_3/ZnO on TE properties has been thoroughly investigated, as listed in Table 5-1. The presence of ZnO and Al_2O_3 layers on CuNi, contributes to the creation of an energy barrier by the oxide layer, resulting in a significant increase in S. Although there is an insignificant decrease in ϱ, the enhanced S after 50 ALD cycles of ZnO compensated for the loss and resulted in an ~45% increase in PF compared to the pristine sample. In addition, the multilayer structure of ZnO/Al_2O_3/ZnO was constructed on the surface of the powder to enhance electrical resistance at phase boundaries (Figure 5-1). In the high cycle number coating ($>$ 50 cycles), the multilayer coatings stained the high PF while significantly reducing the thermal conductivity. For the sample modified with Z44/A11/Z44 multilayers, due to decoupling thermoelectric parameters by ALD, a maximum zT of 0.22 was achieved at 673 K, approximately 128% higher than that of pristine CuNi and nearly as high as previously reported[92–94,143] ((Figure 5-2).

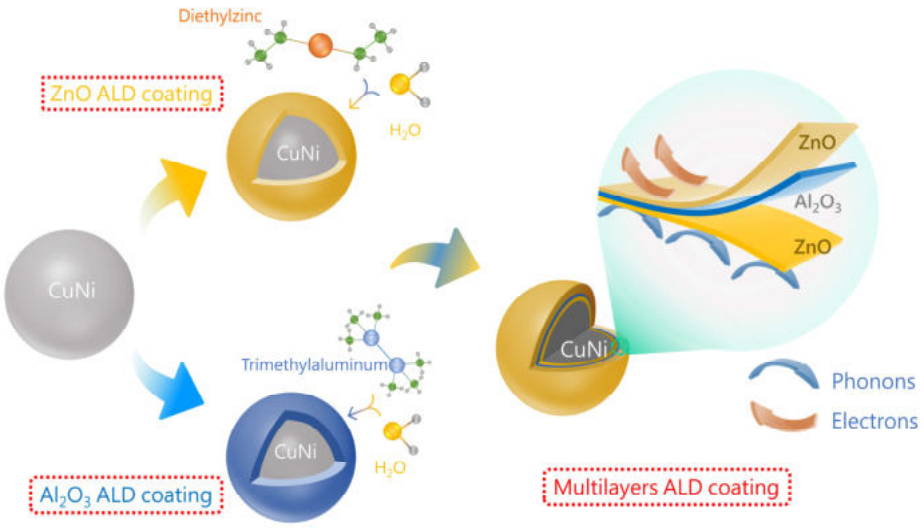

Figure 5-1 *A schematic of the powder ALD process on CuNi. In this work, single coating layers and multilayers with ZnO/Al₂O₃/ZnO structures are deposited on the surface of powders.*

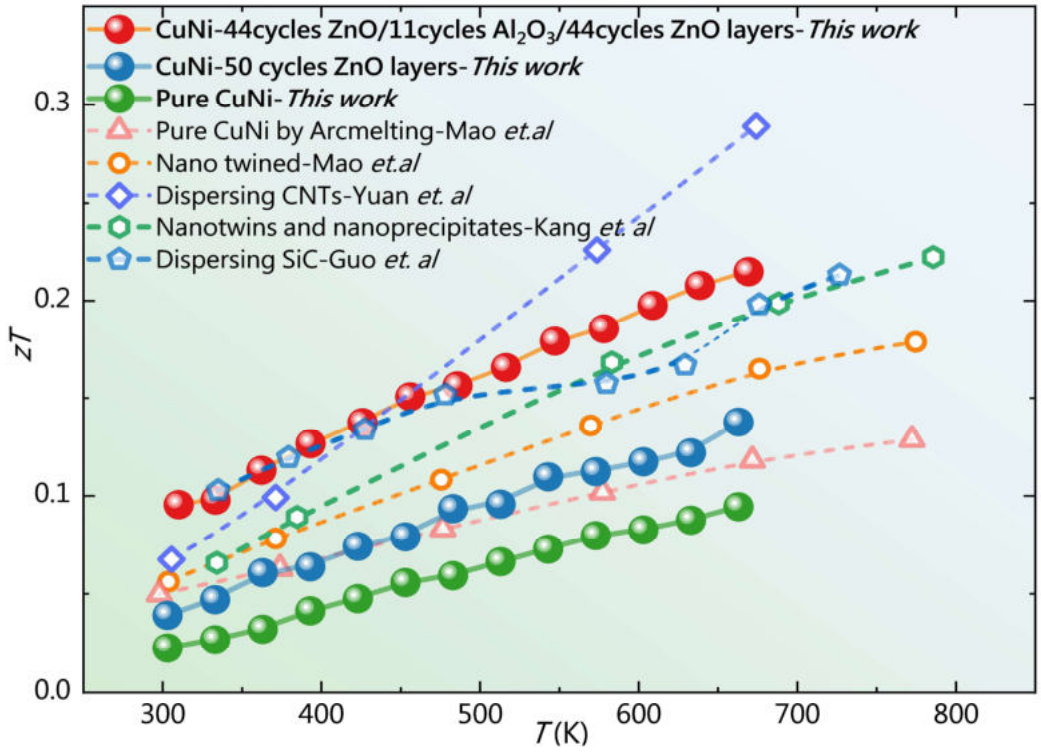

Figure 5-2 *Comparisons of temperature-dependent zT among other CuNi works*[92–94,143].

Types of ALD layers	Compositions of ALD layers	Cycle numbers of coating layers	Sample names in short
Single-kind layers	Al_2O_3	10	A10
		20	A20
		50	A50

		100	A100
	ZnO	10	Z10
		20	Z20
		50	Z50
		100	Z100
Multilayers	$ZnO/Al_2O_3/ZnO$	20/5/20	Z20/A5/Z20
		28/7/28	Z28/A7/Z28
		44/11/44	Z44/A11/Z44

Table 5-1 *Summary of ALD coating layers in this work.*

5.2 Analysis of CuNi powders coated with ZnO and Al_2O_3

To systematically investigate the effect of ALD coating layers on TE performance, the microstructure and composition of ALD thin films and coated powders should first be explored.

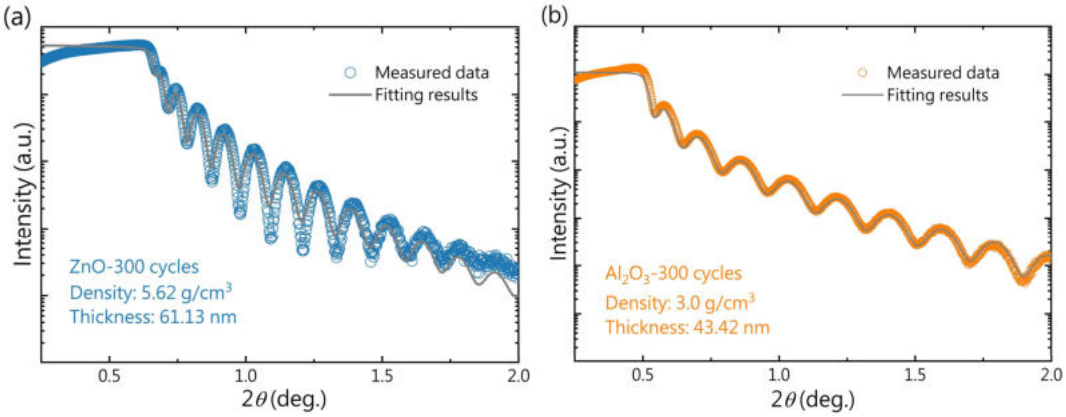

Figure 5-3 *(a) The results of XRR for 300 cycles of ZnO film. (b) The results of XRR for 300 cycles of Al_2O_3 film.*

Analyses of X-ray reflectometry measurement data with respect to a simulated curve indicate a density of 5.6 and 3.0 g/cm^{-3} and a thickness of 61.1 and 43.2 nm for 300 cycles ALD of ZnO and Al_2O_3 thin films on Si substrates, as shown in Figure 5-3(a) and (b), respectively. The linear increase in thin film thickness on the Si wafers by increasing the number of ALD cycles is shown in Figure 5-4(a), suggesting a GPC of 1.4 and 2.1 Å/cycle for ZnO and Al_2O_3, respectively. This reveals excellent thickness controllability at the subnano scale. Additionally, the electrical conductivities of ZnO and Al_2O_3 in the range of 275–400 K were examined, and ZnO films exhibit much higher electrical conductivity, which is approximately five orders of magnitude higher than that of Al_2O_3 (Figure 5-4 (b)). The difference in the electrical conductivities of

ZnO and Al_2O_3 ALD films may play a vital role in the electrical conduction of the particle boundaries, which has a great influence on the overall resistivity of coated bulk samples.

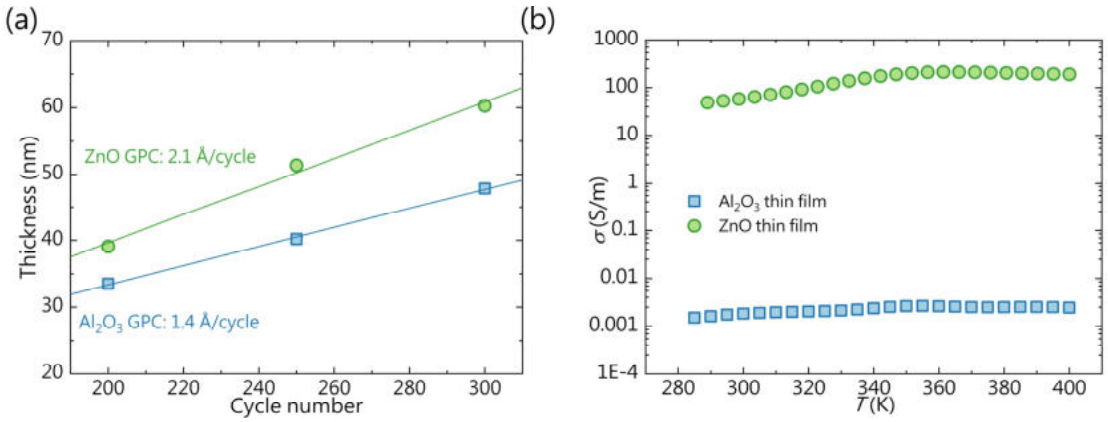

Figure 5-4 *(a) The thickness v.s cycle numbers for ZnO and Al_2O_3 films deposited on Si substrates. (b) The temperature dependence of the electrical conductivity of ZnO and Al_2O_3 films.*

The relationship between the Zn and Al content and ALD cycle numbers can be elicited from the mentioned physical parameters of films. As shown in Figure 5-5(a), we define R_{CuNi}, m_{layer}, m_{CuNi}, ϱ_{layer}, ϱ_{CuNi}, and x_{layer} as the radius of the particle, the mass of the coating layers, the mass of one particle, the density of the coating layers, the density of CuNi and the thickness of the coating layers, respectively.

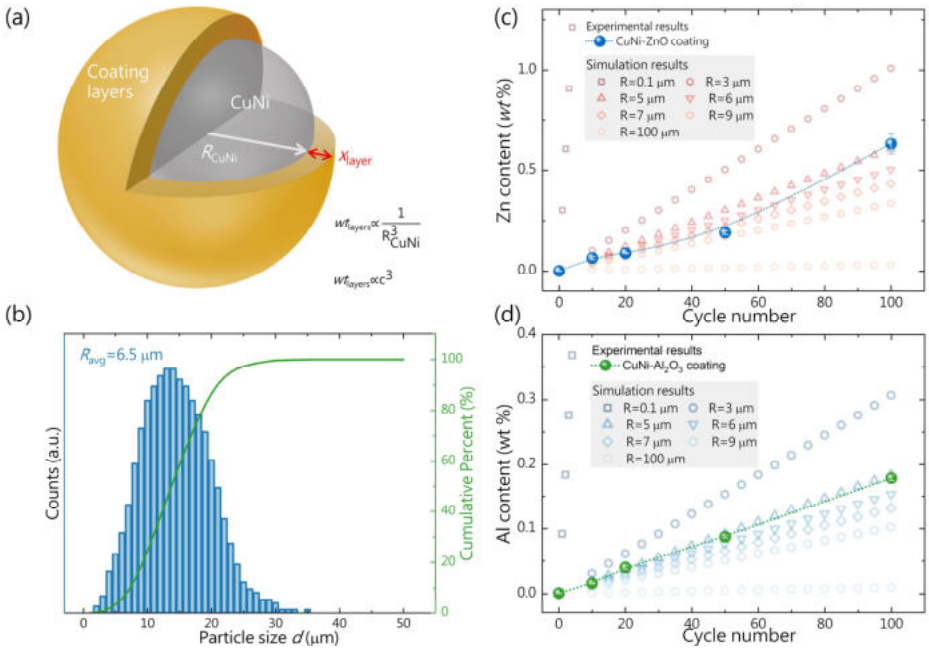

Figure 5-5 *(a) Schematic illustration of particles coated by ALD. (b) The particle size distribution of pure CuNi powders. (c) The cycle number dependence of the weight percentage of Zn. (d) The cycle number dependence of the weight percentage of Al.*

Assuming that all the particles have been uniformly deposited with oxide layers, the mass of layers and one particle can be expressed as

$$m_{\text{layer}}=\varrho_{\text{layer}}\times\frac{4\pi}{3}\left[\left(x_{\text{layer}}+R_{\text{CuNi}}\right)^3-R_{\text{CuNi}}^3\right] \tag{5-1}$$

and

$$m_{\text{CuNi}}=\varrho_{\text{CuNi}}\times\frac{4\pi}{3}\times R_{\text{CuNi}}^3 \tag{5-2}$$

Then, the weight percentage of coating layers (wt %) can be calculated as follows:

$$wt\ \%=\frac{m_{\text{layer}}}{m_{\text{CuNi}}}=\frac{\varrho_{\text{layer}}}{\varrho_{\text{CuNi}}}\times\frac{\left(x_{\text{layer}}+R_{\text{CuNi}}\right)^3-R_{\text{CuNi}}^3}{R_{\text{CuNi}}^3}\times100\%$$

$$=\frac{\varrho_{\text{layer}}}{\varrho_{\text{CuNi}}}\times\frac{\left(\text{GPC}\cdot C_{\text{layers}}+R_{\text{CuNi}}\right)^3-R_{\text{CuNi}}^3}{R_{\text{CuNi}}^3}\times100\%$$

$$=\frac{\varrho_{\text{layer}}}{\varrho_{\text{CuNi}}}\times\left[\left(1+\frac{\text{GPC}\times C_{\text{layer}}}{R_{\text{CuNi}}}\right)^3-1\right]\times100\% \tag{5-3}$$

where GPC is the growth per cycle of the coating layers and C_{layer} is the cycle number. Notably, the mass of the coating layers is negligible in the case of low-content oxides.

Additionally, wt % is proportional to C_{layers}^3 and R_{CuNi}^{-1}, where C_{layer} is the ALD cycle number and R_{CuNi} is the radius of CuNi particles (Figure 5-5(a)). In this work, the average radius of CuNi particles is considered to be 6.5 μm (Figure 5-5(b)). Considering that all the CuNi particles are uniformly coated with ZnO and Al_2O_3 films, the calculated Zn and Al contents as a function of the ALD cycle number are presented in Figure 5-5(c) and (d). The Zn and Al contents in the samples coated with different ALD cycle numbers were also measured by ICP–OES and are presented in Figure 5-5(c) and (d). With increasing ALD cycle numbers, the Zn and Al contents increased monotonically. The experimental data fit well with the simulation, indicating that the coating layers of ZnO and Al_2O_3 were homogeneously deposited on each particle. Furthermore, EDX elemental mapping and point analyses performed on the surface of ZnO-coated samples show that the Zn signal from ZnO is uniformly distributed on the surface of every single CuNi particle, as shown in Figure 5-6.

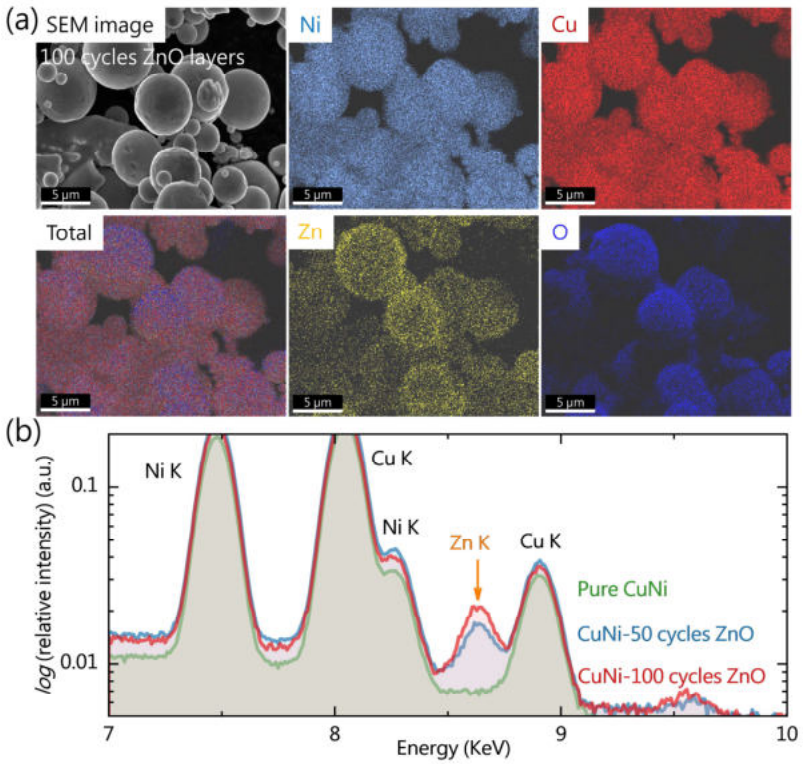

Figure 5-6 *(a) EDX element mapping for 100 cycles of ZnO-coated CuNi particles. (b) EDX spectra of pure ZnO-coated samples and ZnO-coated samples after 50 cycles and 100 cycles.*

5.3 The effect of single-kind oxides on TE performance

The XRD patterns of the as-sintered samples are presented in Figure 5-7. All the main diffraction peaks in the XRD patterns can be well indexed to $Cu_{0.6}Ni_{0.4}$ with an FCC (space group $Fm\bar{3}m$) structure, consistent with the ICP–OES results. In the XRD pattern of powder ALD-modified and sintered samples, the ZnO peaks cannot be detected if fewer than 50 ALD cycles are used, while they appear clearly in the Z100 sample. This indicates that the crystalline ZnO thin films were successfully deposited on the surface of the powders and were not decomposed or formed alloys with CuNi. Due to the amorphous nature of ALD-Al_2O_3[52], no diffraction peaks corresponding to Al_2O_3 were detected in the XRD patterns of ALD-Al_2O_3-modified samples.

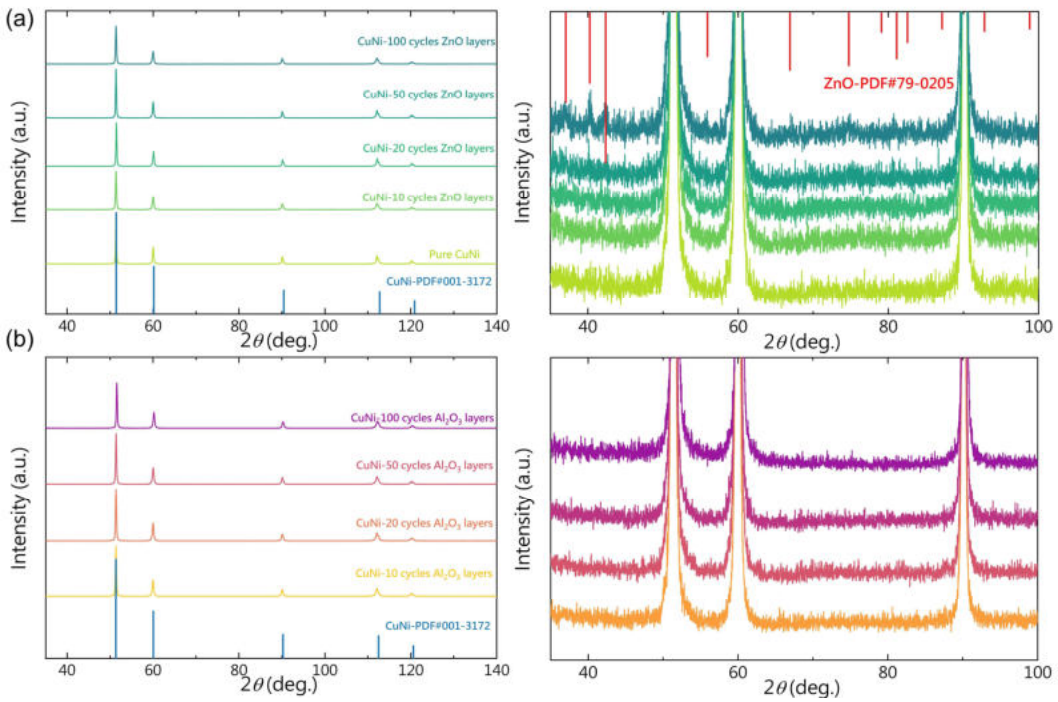

Figure 5-7 *The XRD patterns for the sintered ZnO- and Al_2O_3-coated samples with various cycle numbers.*

The effect of single ALD layers of ZnO and Al_2O_3 on the TE performance of CuNi was thoroughly investigated (see Figure Appendix B). Additionally, the ALD cycle number dependence of the TE parameters is summarized in Figure 5-8. As shown in Figure 5-8(a), ϱ exhibits a monotonously increasing trend with increasing cycle number at both 300 and 673 K measurement temperatures, indicating effective scattering of charge carriers at the energy barrier induced by the oxides. The ϱ of modified CuNi varied from 0.5 to 0.67 μm·Ω when ZnO was deposited, while that in Al_2O_3-coated CuNi rapidly increased and reached 2.07 μm·Ω as the number of ALD cycles increased. This indicates that the chemical composition, crystal structure, and thickness of oxides have different influences on ϱ. Figure 5-8(b) shows that S is significantly augmented by increasing the cycle numbers from -32 to -45 μV/K at 300 K and from -55 to -65 μV/K at 673 K. However, a further increase in the ALD cycle numbers (>50 cycles) of both oxides did not cause a further increase in S, similar to the S variation in our previous works where bismuth particles were coated with different oxides. In Z50 samples, the increment of S compensates for the degradation of ϱ, resulting in an increase of PF from 1.99 to 3.15 mW/m·K^2 at 300 K. However, due to stronger scattering in Al_2O_3-coated samples, the enhancement of PF only occurred in low cycle number coated samples (< 10 cycles) as higher cycle numbers deteriorate PF in Al_2O_3-coated samples.

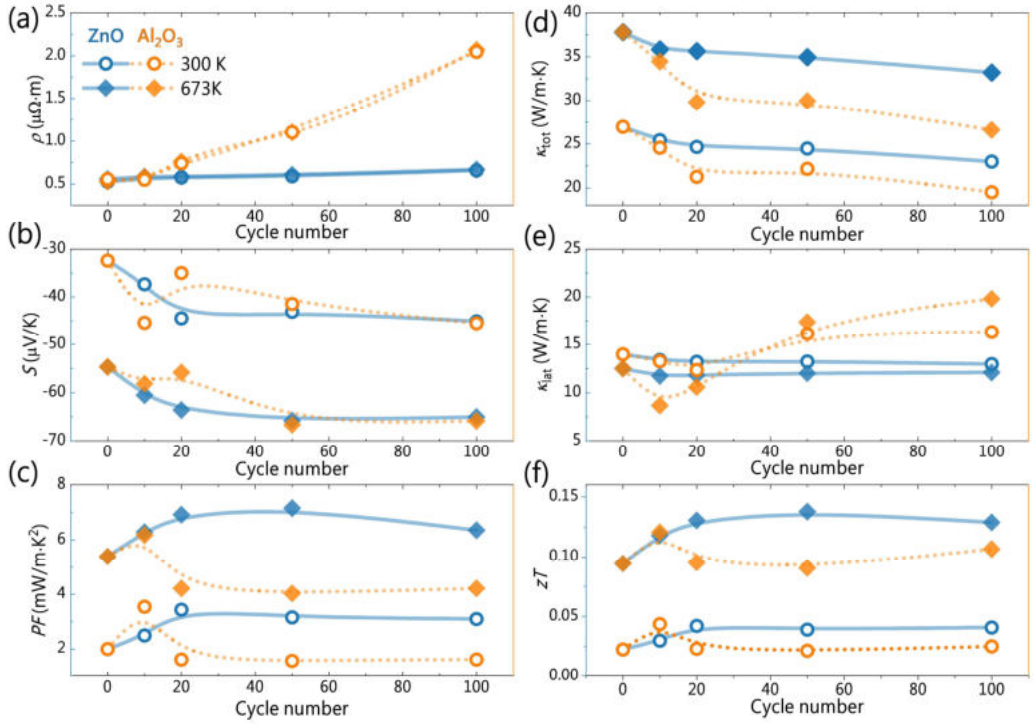

Figure 5-8 *Summary of the ZnO and Al_2O_3 cycle number dependence of (a) ϱ, (b) S, (c) PF, (d) $\varkappa_{tot}$, (e) $\varkappa_{lat}$ and (f) zT at 300 and 673 K.*

The cycle number dependence of $\varkappa_{tot}$ is shown in Figure 5-8(d) and shows a monotonous decreasing trend at both 300 and 673 K measuring temperatures. The $\varkappa_{tot}$ in the A100 sample decreases by 31.6%, while it decreases by only 10.5% in the Z100 sample, both measured at 673 K. Because $\varkappa_{tot}$ is the sum of the electronic ($\varkappa_{ele}$) and lattice ($\varkappa_{lat}$) constituents, the influence of oxide coating layers on phonon scattering should be evaluated in detail. As shown in Figure 5-8(e), the $\varkappa_{lat}$ of the ZnO-coated sample generally decreased with increasing cycle numbers. However, in Al_2O_3-modified samples, effective suppression of $\varkappa_{lat}$ was observed in the A10 sample, reducing the lattice thermal conductivity from 12.5 to 8.7 W/m·K at 673 K. Beyond 10 ALD cycles of Al_2O_3, $\varkappa_{lat}$ significantly increased to 19.8 W/m·K at 673 K in the A100 sample, which is even higher than that of pristine CuNi. The enormous enhancement of $\varkappa_{lat}$ might be a result of some characteristic changes in Al_2O_3 layers during the sintering process. According to previous studies[144], amorphous Al_2O_3 films deposited by ALD at 150 °C can be crystallized at temperatures above ~850 °C. It should be noted that Al_2O_3-coated CuNi in this study was pressed at 800 °C, and the Al_2O_3 films might be fully or partially crystallized. The ultrathin Al_2O_3 and ZnO layers deposited by a low number of ALD cycles can be embedded in CuNi as nanoinclusions, significantly enhancing phonon scattering. However, a thicker, more coalescent, and crystalline Al_2O_3 film deposited by the higher number of ALD cycles, as a well-known high $\varkappa$ material, may form the

thermal conduction path, leading to a tremendous increase in $\varkappa_{lat}$. Due to the enhancement of PF and suppression of $\varkappa_{lat}$, the zT values changed from 0.09 to 0.14 and 0.12 at 673 K in the Z50 and A10 samples, respectively.

5.4 The effect of multilayers on TE performance

Considering the results discussed for the CuNi modified with a single-layer oxide, it can be concluded that although ϱ is increasing constantly by increasing the ZnO and Al_2O_3 ALD cycle numbers, the significant augmentation of S occurs when just a few ALD cycles are performed (< 50 cycles). Additionally, from the variation in PF with the cycle number, it can be concluded that ZnO performs better than Al_2O_3 in optimizing the electrical properties. However, the reduction of $\varkappa_{lat}$ in all ZnO-coated samples is not as effective as that of the A10 sample, indicating strong phonon scattering by Al_2O_3 compared to ZnO. It should also be noted that due to the amorphous-to-crystalline transition, the thicker Al_2O_3 layer might form a thermal conduction path that is not favorable to $\varkappa_{lat}$ suppression.

Therefore, combining ZnO and Al_2O_3 as a multilayer structure might result in the decoupling of TE parameters. To prove this, an ultrathin Al_2O_3 layer was inserted into ZnO layers to construct the multilayer structure. It can be postulated that using this approach, due to the doping effect, the ϱ of multiple layers decreased compared to that of ZnO[142]; thus, less PF loss can be expected. Additionally, a lower ϱ allows for increasing the thickness of layers, which is beneficial for the suppression of $\varkappa_{lat}$. Note that the crystal complexity of multilayers due to the doping effect might cause stronger phonon scattering in the phase boundaries.

The present study opted for a ZnO:Al_2O_3 ratio of 8:1 to enhance electrical conductivity, as reported in reference[142]. The effect of multilayer structures with different thicknesses on the TE performance is presented in Figure 5-9. As shown in Figure 5-9(a), ϱ increased constantly with increasing ALD cycle numbers of multilayer constituents. Compared to the Z100 sample, the ϱ of the Z44/A11/Z44 sample decreased by 5% over the whole measured temperature range. Additionally, it was observed that the ϱ of the Z20/A5/Z20 sample was lower than that of the Z50 sample. This indicates the enhancement of electrical conductivity at phase boundaries after inserting Al_2O_3 layers. Figure 5-9(b) indicates that the thickest multilayer possesses a higher absolute S than the thin multilayer and single component layers. The more conductive phase boundaries result in an 11.7% enhancement in PF in the Z44/A11/Z44 sample at 673 K when compared to the Z100 sample. As shown in Figure 5-9(d) and (e), the hypothesis that a thicker multilayer might suppress $\varkappa_{lat}$ more effectively, decreasing to 9.5 W/m·K at

673 K in the Z44/A11/Z44 sample. The temperature-dependent zT of the optimum multilayer-coated samples is demonstrated in Figure 5-9(f). The zT value of the Z44/A11/Z44 sample increased by 128% compared to pure CuNi bulks.

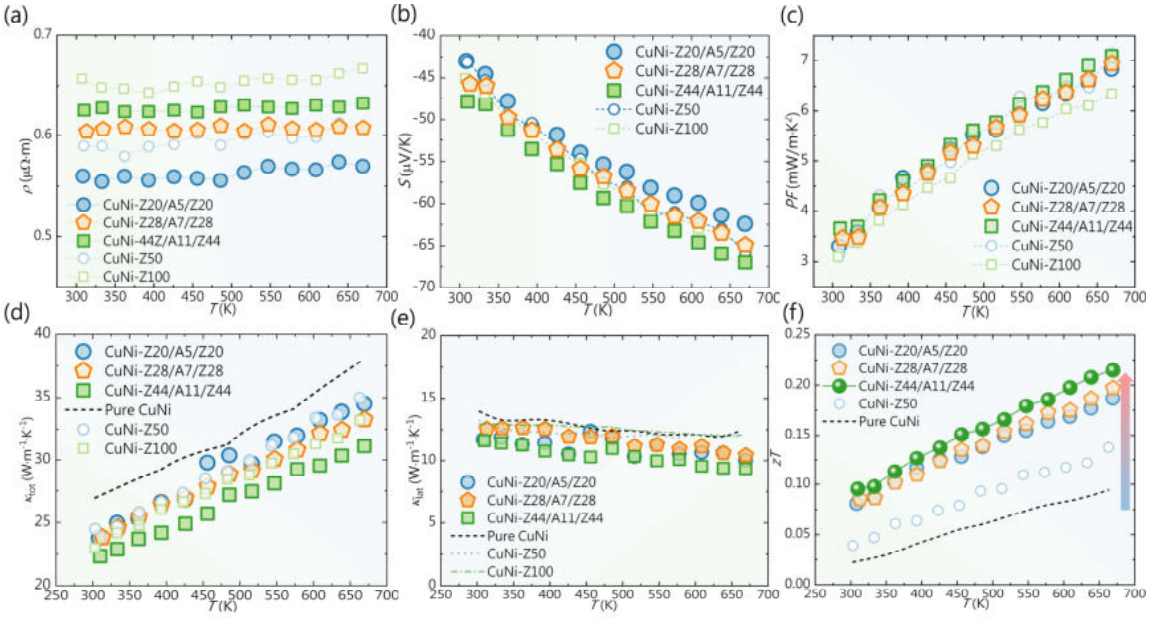

Figure 5-9 *Temperature dependence of (a) ϱ, (b) S, (c) PF, (d) κ_{tot}, (e) κ_{lat}, and (f) zT with the multiple-layer ZnO/Al_2O_3/ZnO structure.*

As previously discussed, the Al_2O_3 layers can be crystallized during the high-temperature sintering process. According to the literature[141,142], Al atoms can diffuse into the ZnO structure as a dopant, which might affect the multilayer structure after the sintering process. Figure 5-10(a) demonstrates the EDX-elemental mapping of the Z44/A11/Z44 bulk sample, confirming the homogeneous distribution of Zn and O in the particle boundaries and demonstrating the excellent conformality of films grown using the ALD technique on the surface of particles. The slight contrast of Al can also be observed, revealing that the 11 cycles of Al_2O_3 cause an even distribution of the phase on the surface of CuNi particles. To precisely analyze the content and distribution of multilayer constituent atoms, the mentioned sample was further studied using scanning transmission electron microscopy STEM-EDX and APT.

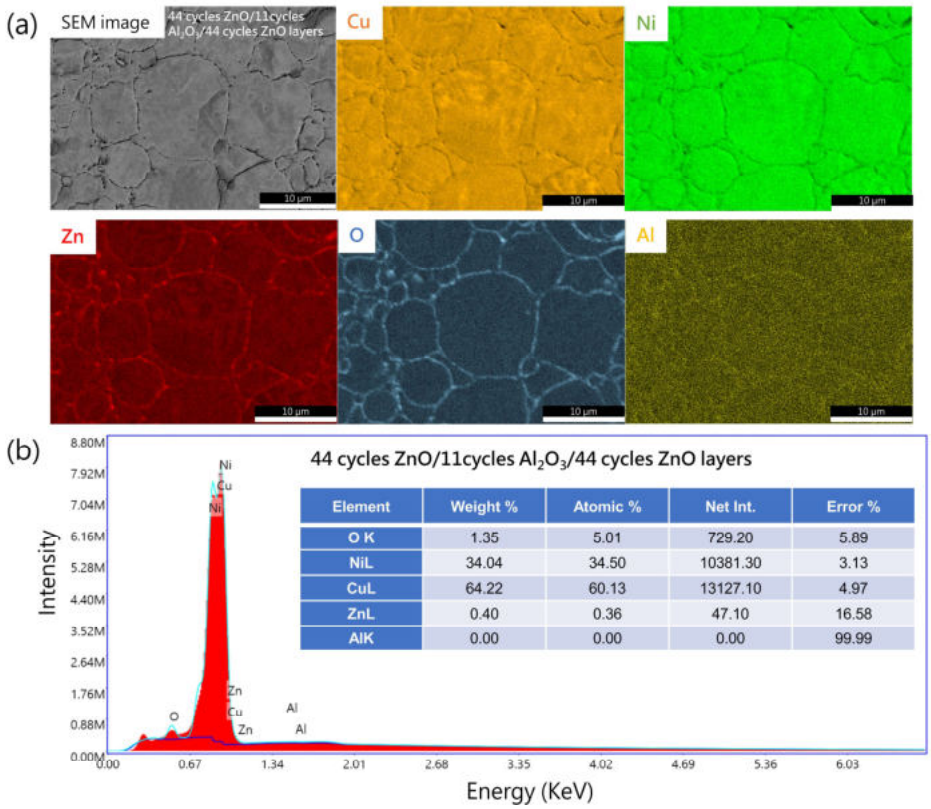

Figure 5-10 *EDX mapping (a) and spectrum (b) of the ZnO/11 cycles Al_2O_3/44 cycles ZnO layer-coated sample.*

The STEM-high angle annular dark field (HAADF) image shows dark contrast in the particle boundaries (Figure 5-11), as the oxide layers have lower atomic masses. The Al-rich oxide phase and a Zn-rich oxide phase (ZnO) are also clearly visualized in Figure 5-11, showing the different contrast and morphologies. Their compositions are indeed separated from STEM-EDX spectrum imaging (Figure 5-11(b)), with one phase enriched in Al (Al/Zn ratio: 0.29) and the other enriched in Zn (Al/Zn ratio: 0.01). The Al-rich oxide phase is thinner and continuously surrounds the CuNi matrix, whereas the Zn-rich oxide phase is more rounded and located between the matrix and the Al-rich oxide. The homogeneous coverage of the Al-rich oxide phase confirms the successful deposition of Al_2O_3 ALD layers within the ZnO layers. Furthermore, the Zn-rich oxide phase was captured in our APT analysis, where it is confirmed to be mostly ZnO with less than 1% Cu, Ni, and Al (Figure 5-11(d)). However, the diffusion of Al atoms results in the doping effect and causes higher electrical conductivity of the multilayer. The atomic-scale microstructural analyses confirm that using ALD to accurately regulate the intrinsic characteristics of the modifying layer is possible, resulting in a considerable TE performance enhancement of the CuNi thermoelectric material. In addition, this powder ALD method could be widely used in other TE materials and provide a new dimension to optimize the properties of phase

boundaries. Thus, the present work provides insight into the structural design and synthesis of broadly functional hybrid TE material systems.

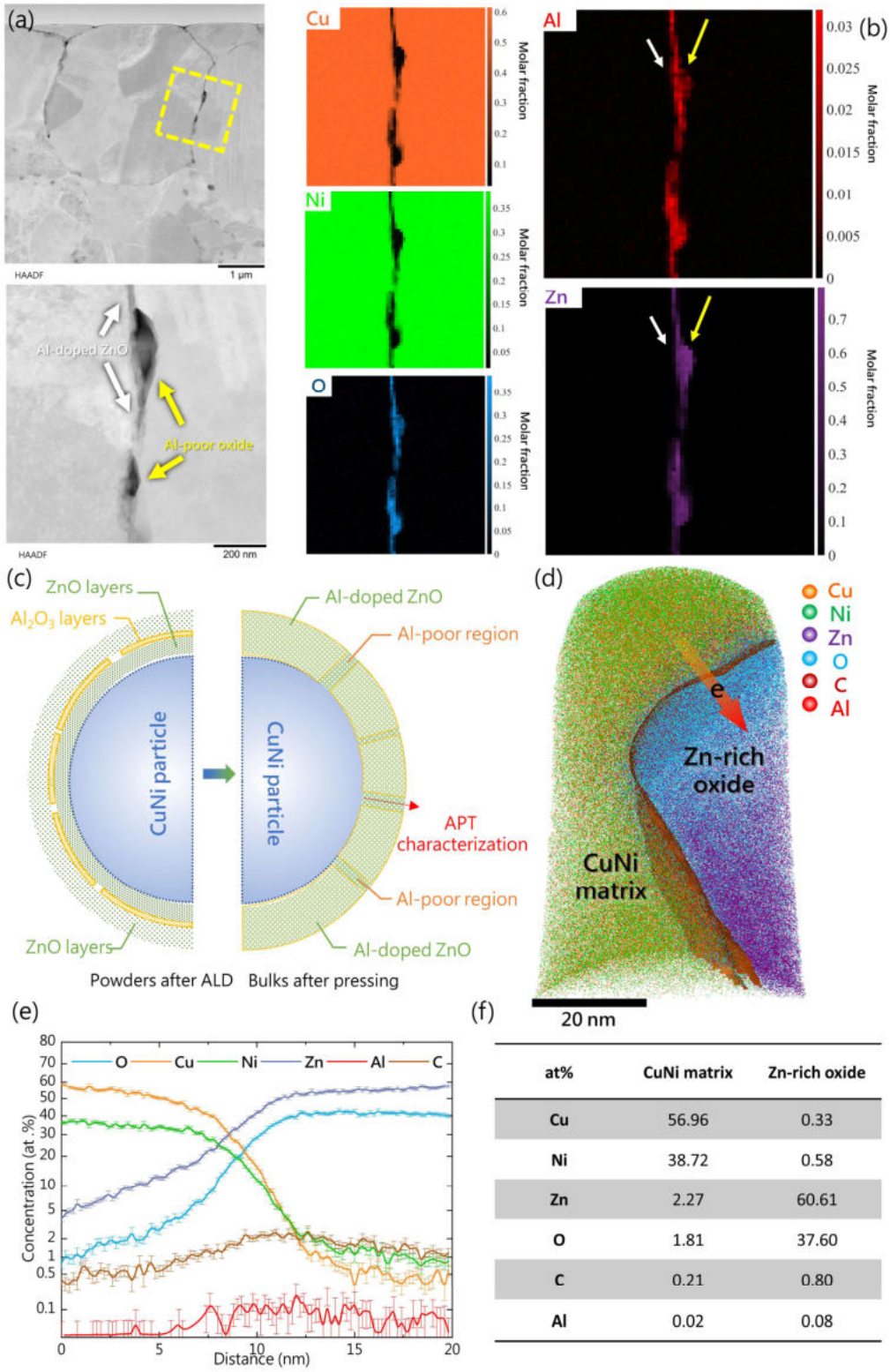

at%	CuNi matrix	Zn-rich oxide
Cu	56.96	0.33
Ni	38.72	0.58
Zn	2.27	60.61
O	1.81	37.60
C	0.21	0.80
Al	0.02	0.08

Figure 5-11 *(a) HAADF-STEM image of 44 cycles ZnO/11 cycles Al_2O_3/44 cycles ZnO layers coated on a CuNi specimen and HAADF-STEM image focused on the boundary with (b) EDX elemental maps. (d) Schematic illustrations of the diffusion of Al. (e) 3D atom map of 44 cycles of ZnO/11 cycles of*

Al_2O_3/44 cycles of ZnO layer-coated bulk. (e) 1D concentration profile along the d direction in (d) and the elemental concentrations from different areas.

5.5 Summary

In summary, ALD-based interface modification has been employed to improve the performance of CuNi alloys by decoupling and optimizing the TE parameters. First, the influence of a single kind of oxide coating (ZnO and Al_2O_3) was thoroughly investigated. The EDX mapping results confirmed the uniform coating on the CuNi powders by ZnO and Al_2O_3 layers. Additionally, a standard model is designed to obtain the relationship between *wt* % of Zn/Al and oxide cycle numbers, and the experimental results from ICP–OES fit well with the simulation data. This model can be used to estimate the actual composition of coating layers and can easily be adapted to other powder ALD processes. For the as-prepared ZnO-coated sample, because of the energy filtering effect, considerable enhancement of S compensates for the electrical loss, resulting in improved PF values in all ZnO-coated samples. Combined with slight suppression of $\varkappa_{\mathrm{lat}}$, a 55.5% enhancement of zT was realized in the Z50 sample. For the as-prepared Al_2O_3-coated sample, Al_2O_3 is detrimental to electrical conduction at the boundaries and the PF of the A10 sample. The significant suppression of $\varkappa_{\mathrm{lat}}$ only obtained in low cycle numbers and thicker Al_2O_3 layers provides the thermal conduction path due to the amorphous-to-crystalline transition of Al_2O_3. To reduce the ϱ of the coating layers, the Al_2O_3 layers were inserted into ZnO layers to construct "multiple layers". The APT results confirmed the existence of ZnO layers. Element scanning proved that the Al atoms diffused into the ZnO layers and that the Al doping effect may benefit the increase in electrical conduction in the phase boundaries. In this approach, higher cycle numbers of ZnO are used to suppress $\varkappa_{\mathrm{lat}}$ and maintain the PF. As a result, the zT value of the Z44/A11/Z44 sample increased by 128% compared with pure CuNi bulks, which is nearly the highest zT value among other CuNi works. The study shows that ALD-based interface modification could be a general route to decouple the strongly interrelated parameters and precisely modify the properties of phase boundaries, which is effective for other thermoelectric materials beyond CuNi alloys.

6

Chapter 6 Blocking ion migration in Zn_4Sb_3 by powder ALD

The majority of the presented results in this chapter have been prepared in the following article:

Shiyang He, Amin Bahrami, Chanwon Jung, Xiang Zhang, Ran He, Siyuan Zhang, Kornelius Nielsch*, Blocking the Ion Immigration in Zn_4Sb_3 with Oxide Coating by Powder ALD. (***Under preparation***)

6.1 Introduction

Stability and reliability are important requirements for a candidate TE material for practical applications. However, the thermal stability of β-Zn_4Sb_3 with interstitial Zn ions could degrade under a large temperature difference and current bias. The temperature gradient and current drive the migration of interstitial ions along the direction of the temperature gradient/current, which depends on the majority carrier in materials. Due to Zn atom immigration, the part near the hot side exhibits larger S values. Zn migrates from the hot to the cold side of the sample to be expelled from the structure as Zn whiskers. After several heat cycles, the loss of Zn significantly deteriorates the TE properties (Figure 6-1).

Therefore, it is important to improve the stability of the β-Zn_4Sb_3 compound while retaining its high TE performance. The enhanced thermal stability is beneficial for a large-scale TE generator using β-Zn_4Sb_3 as the *p*-type legs. To solve the problem of material stability, several strategies have been applied to Zn_4Sb_3 to explore the blocking effect, as mentioned in previous chapters.

In this work, using powder ALD, the coating layers can be deposited on the surfaces of different particles. Using this approach, millions of phase boundaries can be formed between ZnO and Zn_4Sb_3 (Figure 6-1). As ZnO layers are deposited on the surface of powders, 100 cycles of ZnO coating layers can act as barriers to block Zn atom migration under the temperature difference and current bias (Figure 6-2). By controlling the cycle numbers in ALD, the thickness of the coating layers can be precisely modified, which allows us to balance the TE performance and blocking effect.

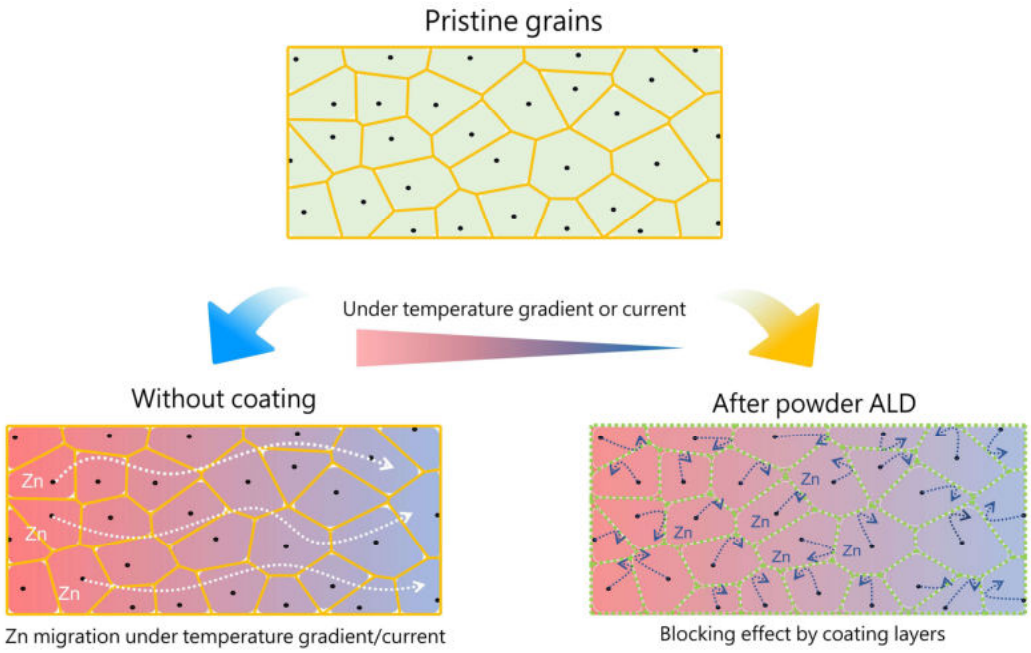

Figure 6-1 *Blocking effect on Zn ions by powder ALD. Under the temperature gradient of the current bias, the Zn ions may migrate from the hot side to the cold side. However, the oxide layer deposited by powder ALD may act as an energy barrier and block the movement of Zn ions.*

With increasing ZnO layer cycle numbers, the layer thickness can be precisely tuned to balance the thermal stability and TE performance. In the 100 cycle ZnO-coated sample, although there was little deterioration of PF due to increasing resistivity, the total thermal conductivity resulted in similar zT values compared with pure Zn_4Sb_3, indicating that the TE performance of the 100 cycle ZnO layer-coated sample did not degrade. However, 100 cycles of ZnO layers result in significantly enhanced thermal stability and effectively block Zn ion movement even after 10 thermal cycling tests.

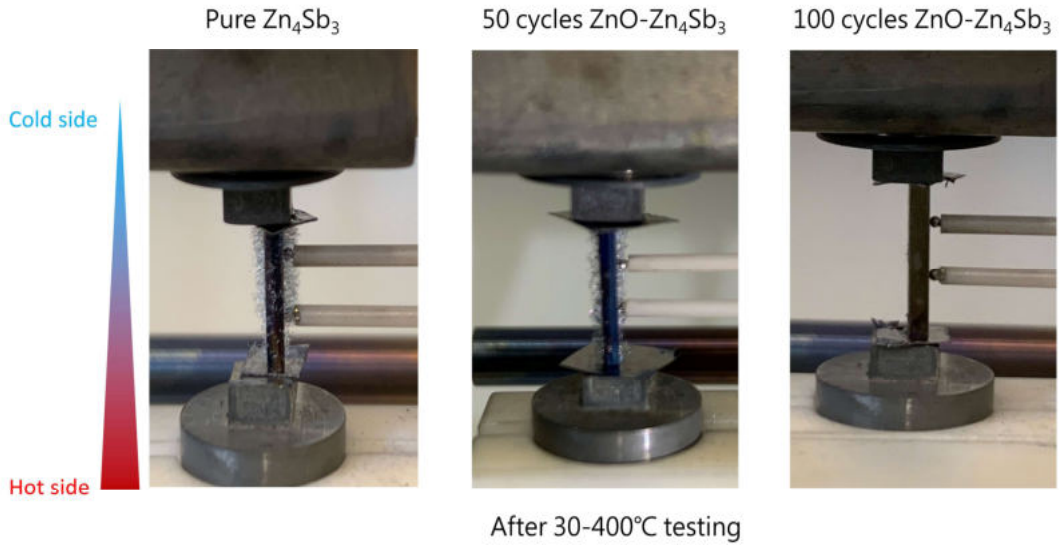

Figure 6-2 *Optical images for pure, 50 cycle, and 100 cycle ZnO layer-coated Zn_4Sb_3 samples after 300–673 K testing. The cold side of the sample shows more Zn whiskers than the hot side.*

6.2 Zn ion migration analysis in pure Zn_4Sb_3

As previously mentioned, the powder size and the potential energy barrier must be specifically designed to satisfy the relationship that τ_p (phonon momentum relaxation length) $<$ d (particle size) $<$ τ_e (electron momentum relaxation length), which results in a substantial net improvement of PF due to enhancement of S. Thus, it is necessary to investigate the minimum ball-milling time to form the Zn_4Sb_3 phase and to obtain the smallest particle size simultaneously.

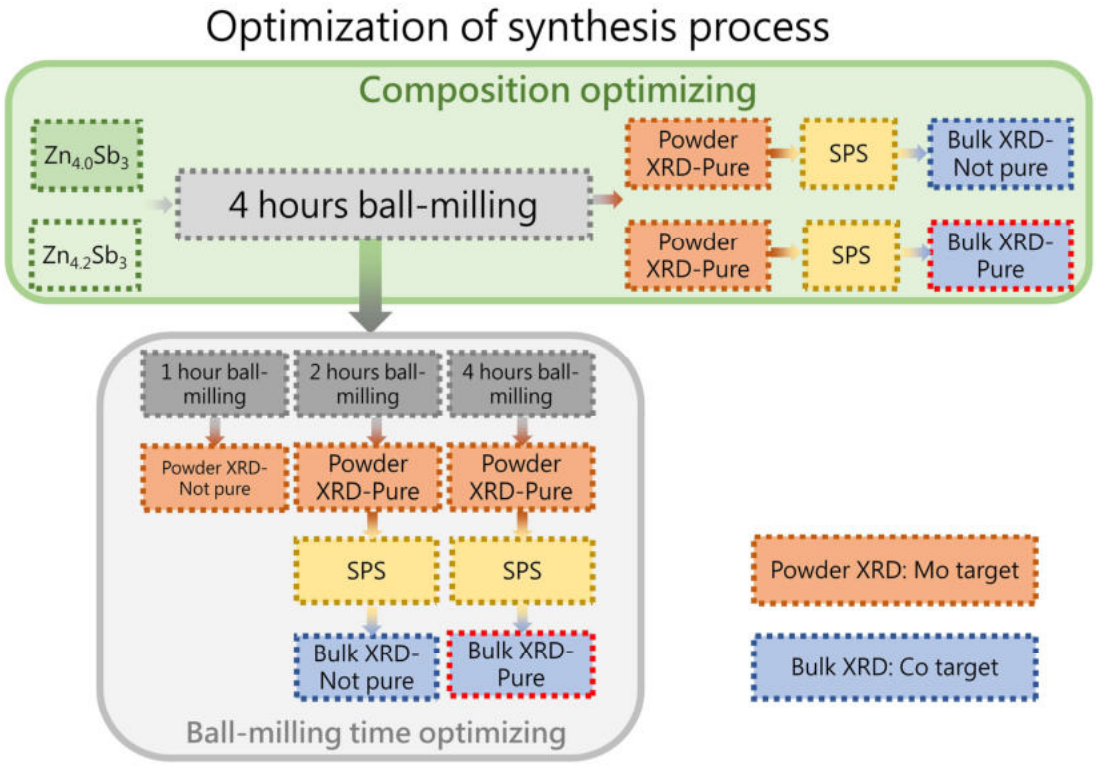

Figure 6-3 *Optimization of the synthesis process of Zn_4Sb_3.*

It is well known that Zn possesses low vapor pressure. According to the reference, the Zn-rich composition in Zn_4Sb_3 benefits the suppression of the second phase forming during the high-temperature pressing process (Figure 6-3). As shown in the powder XRD patterns of Figure 6-4(a), the phase of Zn_4Sb_3 is formed after 4 hours of ball milling, and there is no extra Zn peak in the composition of $Zn_{4.2}Sb_3$. However, after the SPS process, the impurities of ZnSb can be detected in the composition of Zn_4Sb_3, but the XRD pattern can be indexed well to the single phase when the Zn content increased to 4.2 (Figure 6-4(b)). The loss of Zn may be attributed to the evaporation of Zn during the pressing process, indicating that extra Zn is necessary for obtaining a single phase of Zn_4Sb_3. Additionally, an investigation on the minimum ball-milling time was carried out, as shown in Figure 6-4(c). The phase of Zn_4Sb_3 cannot be formed when

the ball-milling time is below two hours according to the powder XRD results. However, as presented in the bulk XRD patterns after sintering (Figure 6-4(d)), two hours of balling-milling was still enough to realize full reactions, but an impurity of Zn_3Sb_4 was detected. Therefore, four hours are the optimum parameters for ball-milling time and were selected for the following investigation.

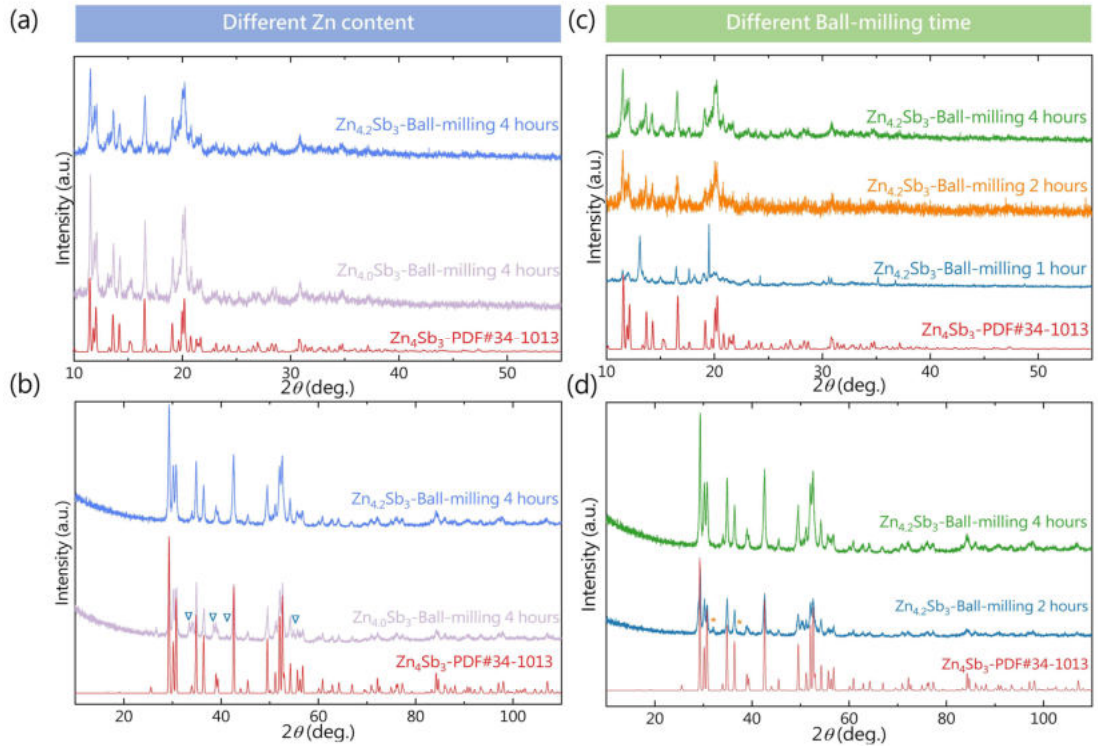

Figure 6-4 *(a) Powder XRD patterns of Zn_4Sb_3 with different Zn contents. (b) The bulk XRD patterns of Zn_4Sb_3 with different Zn contents (▼represents ZnSb). (c) The powder XRD patterns of Zn_4Sb_3 with different ball-milling times. (d) The bulk XRD patterns of Zn_4Sb_3 with different ball-milling times (* represents Zn_3Sb_2).*

After one thermal cycle at 300–673 K, the migration of Zn in the pure sample can be clearly observed in Figure 6-2. After electrical characterization in the range of 300–673 K, the Zn whiskers grew on the surface of the bulk sample and exhibited a graded distribution in which Zn whiskers were enriched on the hot side. This result indicated that the Zn ions moved from the hot side to the cold side even under a 30 K temperature difference (set by the LSR machine). The SEM images of the surface and fracture morphologies are presented in Figure 6-5(a). The Zn whiskers grew from the inside of the sample, and their diameter ranged from 10 nm–15 μm. Additionally, a strong Zn peak can be detected in the XRD pattern after just one thermal measurement (Figure 6-5(b)), implying the poor thermal stability of pure Zn_4Sb_3 due to the migration of Zn.

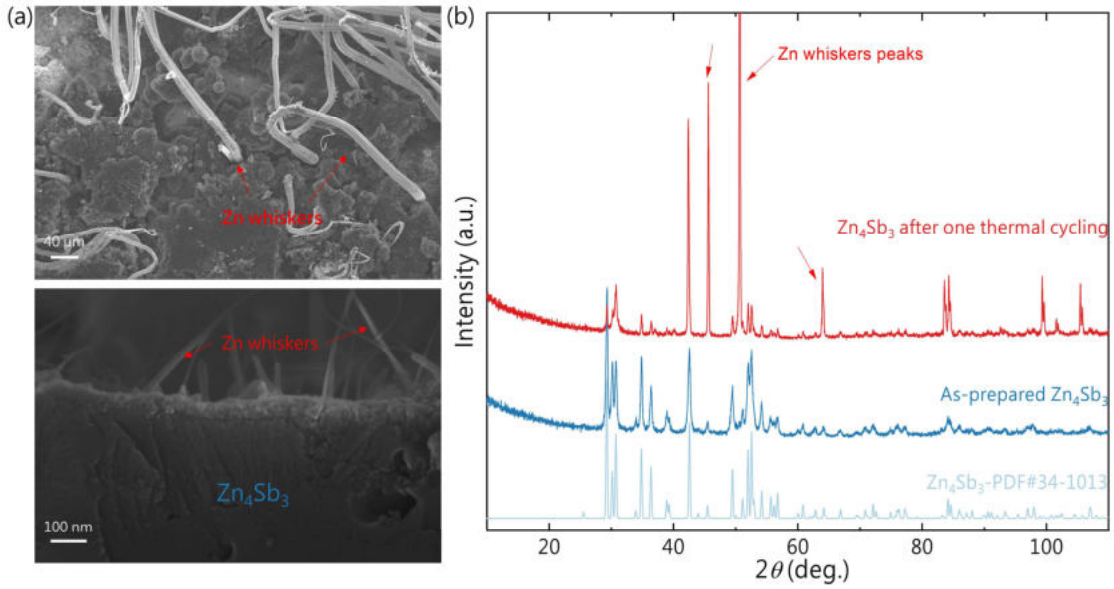

Figure 6-5 *(a) SEM images of the pure sample after one thermal cycle. (b) Comparison of XRD patterns between the as-prepared and measured samples.*

6.3 The powder ALD effect on microstructure and thermoelectric properties

ZnO films are deposited using the powder ALD method in specified cycles (50–200 cycles) to systematically examine the influence of various oxide coatings on the microstructure, stability, and TE performance of Zn_4Sb_3. The SEM images of the fractured surfaces of various sintered Zn_4Sb_3 samples are shown in Figure 6-6. It is noted that the fractured surface for single-phase bulk Zn_4Sb_3 showed a typical coarse and anisotropic structure without apparent preferential orientation for grains. Additionally, the nanopores observed in pure Zn_4Sb_3 indicate that the elemental Zn may evaporate during the pressing process.

As shown in Figure 6-6, the phase boundaries between ZnO and Zn_4Sb_3 can be clearly observed, indicating that the ZnO layers were successfully deposited on Zn_4Sb_3 and did not react with the matrix. With increasing ZnO cycle number, the thickness of the ZnO layers increased. In the 200 cycle ZnO-coated sample, as shown in Figure 6-6(e), a uniform coating layer existed on the boundaries of the three particles, and a layer thickness of ~72 nm was measured, which is consistent with the GPC of ZnO layers on the Si substrate.

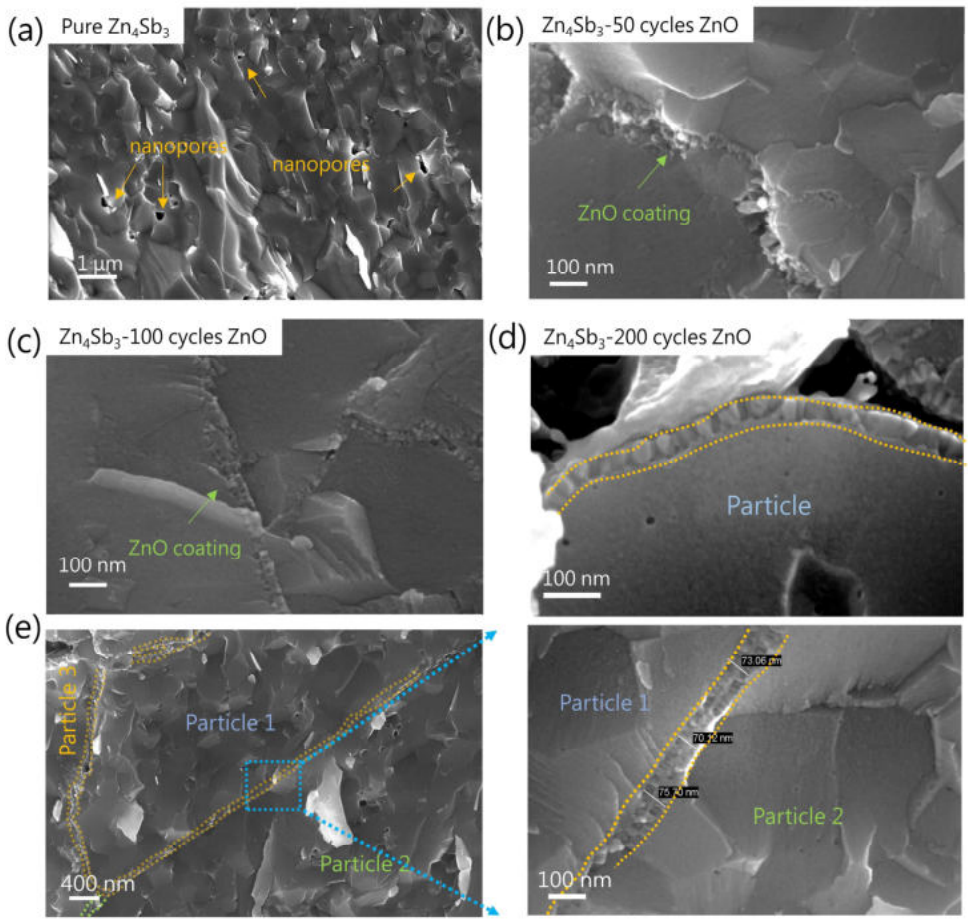

Figure 6-6 *SEM images of the fracture surface of (a) pure Zn_4Sb_3, (b) ZnO-coated Zn_4Sb_3 after 50 cycles (c) ZnO-coated Zn_4Sb_3 after 100 cycles, and (d) ZnO-coated Zn_4Sb_3 after 200 cycles. (e) Higher-resolution SEM image of ZnO-coated Zn_4Sb_3 after 200 cycles.*

The effect of ZnO layers on TE performance has been thoroughly investigated, as shown in Figure 6-7. The deposition of oxide layers on the surface of Zn_4Sb_3 has a significant effect on electrical transport. The temperature-dependent S, ϱ, and PF of the ZnO-coated samples are shown in Figure 6-7(a)–(c). Increasing the number of ZnO cycles monotonically promoted ϱ from 30 to 42 μΩm at 623 K, but S showed slight changes, indicating that the ZnO layers mainly substantially suppressed the carrier mobility. Owing to the deterioration of electrical conduction, the overall PF of the ZnO-coated samples decreased by 25% at 573 K after 100 cycles compared with pristine Zn_4Sb_3. However, the ZnO layers can effectively enhance phonon scattering, and $\varkappa_{lat}$ can be reduced. As shown in Figure 6-7(d)–(e), $\varkappa_{tot}$ decreased from 1.0 to 0.85 W/m·K after 100 cycles of ZnO coating, and a 21.4% reduction in $\varkappa_{lat}$ was realized at 623 K. Benefiting from the decrease in $\varkappa_{tot}$, zT was not degraded in the 100-cycle ZnO-coated sample, which indicated that adjusting the thickness of the ZnO layers could precisely modulate the TE properties.

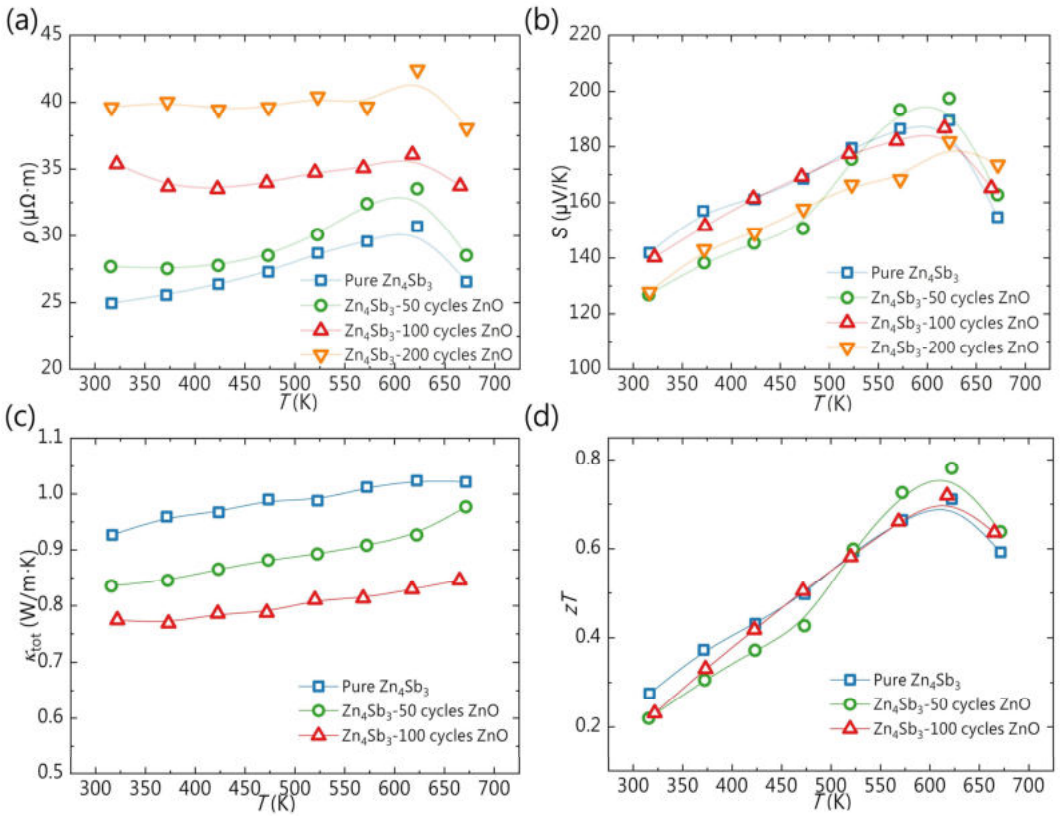

Figure 6-7 *Temperature dependence of (a) ϱ, (b) S, (c) PF, (d) $\varkappa_{tot}$, (e) $\varkappa_{lat}$, and (f) zT in pure Zn_4Sb_3 and ZnO-coated Zn_4Sb_3 samples.*

6.3 Stability testing on ZnO-coated samples

As shown in Figure 6-2, a decreasing amount of Zn whiskers after 50 cycles of ZnO coating can be observed, and Zn whiskers even diminished in 100 cycles of the ZnO-coated samples, indicating that 100 cycles of ZnO can effectively block Zn ion movement. To further verify the thermal stability, 10 thermal cycling tests were performed on the pure and 100-cycle ZnO-coated samples. As shown in Figure 6-8(a), ϱ first increased and then decreased with increasing thermal cycling number. It can be speculated that Zn_4Sb_3 first partly decomposed into ZnSb, which possesses a higher ϱ, and extra Zn just grew out along the temperature gradient. However, after 100 cycles of ZnO coating, the TE performance of the sample was stabilized, and prolonging the thermal cycling numbers did not result in a variation in the electrical properties (Figure 6-8(b)), implying that the 100 cycles of ZnO layers successfully blocked the migration of Zn ions and stabilized the TE performance. The XRD patterns, as shown in Figure 6-9, indicated that there was a decomposition process (from Zn_4Sb_3 to ZnSb) in 50 cycles of ZnO-coated samples with just one thermal cycle. In the 100-cycle ZnO-coated sample, almost no extra peak was detected after 10 thermal cycling tests, indicating that excellent thermal stability was realized.

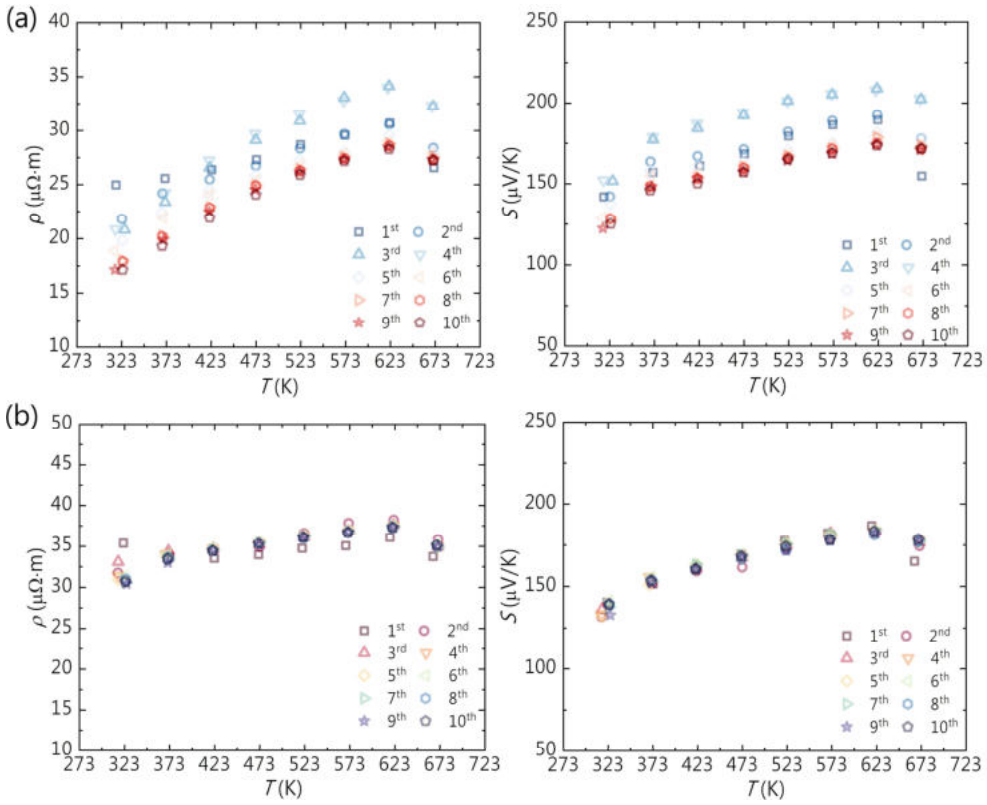

Figure 6-8 *Thermal cycling with electrical characterization for (a) pure Zn_4Sb_3 and (b) ZnO-coated Zn_4Sb_3 after 100 cycles.*

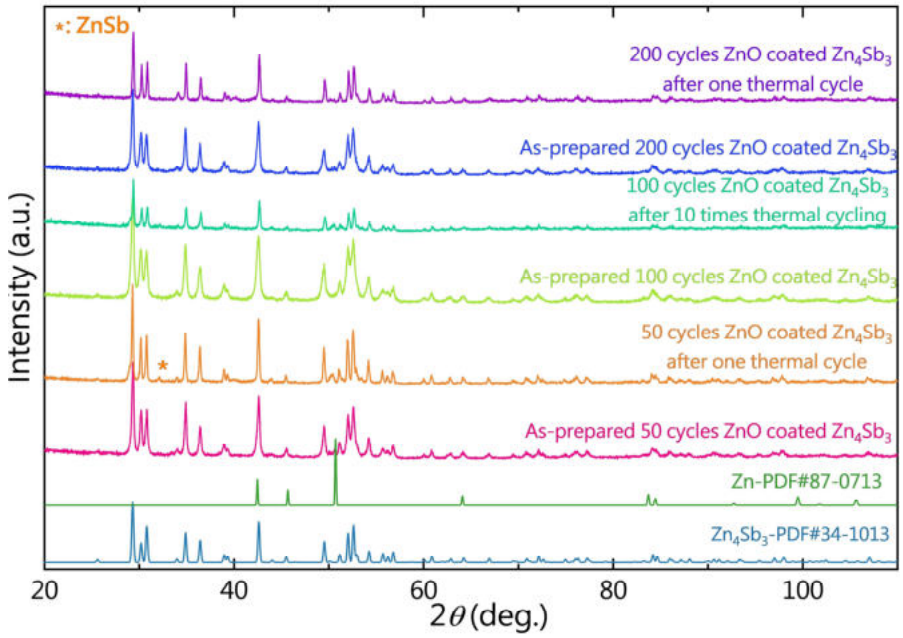

Figure 6-9 *The XRD patterns for ZnO-coated sample before and after thermal cycling tests.*

6.4 Summary

Herein, a powder atomic layer deposition strategy is introduced to accurately control and modify the phase boundaries of Zn_4Sb_3, which could block the migration of Zn ions and enhance thermal stability. To demonstrate the effectiveness of this strategy, ultrathin interlayers of oxides after typically 50–200 cycles are uniformly deposited at the phase boundary of Zn_4Sb_3. The deposition of ZnO coating layers and the formation of the ZnO/Zn_4Sb_3 interface create barriers for charge carriers and ions. Although there is little deterioration in electrical conductivity, the $\varkappa_{tot}$ suppression of ZnO-coated samples after 100 cycles compensated for the loss and resulted in almost the same zT values compared with the pristine sample. Additionally, the 100-cycle ZnO-coated samples show excellent thermal stability, and there is no deterioration in the TE performance after 10 thermal cycling tests, indicating an effective blocking effect on Zn ion migration. The blocking effect realized by powder ALD opens a new window of opportunity for stabilizing the TE performance of Zn_4Sb_3, and it can be easily adapted for other mixed ionic electronic conductors.

7

Chapter 7 Summary and outlook

7.1 Summary

The aim of this thesis is to investigate the effect of ALD coating layers on the transport of charge carriers, phonons, and ions. Owing to the layer-by-layer deposition, each particle of TE powders could be uniformly coated with specific compositions and thicknesses. This allows us to precisely tune the electrical/thermal transport at the boundaries and optimize TE performance. Additionally, using powder ALD, the barrier coating can be deposited on the surface of different thermoelectric particles. The coating will act as a barrier to effectively block atom migration under the temperature difference and current bias. From an industrial viewpoint, if the exposure time of precursors is long enough, the mass of powders can be scaled up to several kilograms, which could be beneficial for realizing industrial-scale leg fabrication.

The main conclusions of this thesis are summarized below:

For the first time, ultrathin layers of Al_2O_3, TiO_2, and ZnO are deposited on the surface of ball-milled Bi powders. The experimental results show that by tailoring the microstructure at the atomic scale, S can be improved from -68 to -79 μV/K after 5 cycles of the Al_2O_3 coating process. Microstructural analyses show that grain growth could be suppressed after the deposition of Al_2O_3, ZnO, and TiO_2 coatings during the sintering process. As a result of the reduction in the thermal conductivities, the zT values of all of the coated samples were enhanced, and the highest zT of ~0.15 was obtained for the Al_2O_3-coated sample after 5 cycles at 390 K (~0.13 at 300 K). Additionally, a Sb_2O_5 thin film was deposited for the first time utilizing ALD due to the reaction of $SbCl_5$ and H_2O_2 on Bi particles. The amorphous nature of Sb_2O_5 thin films before and after annealing validated the deposited oxide's thermal stability. Because of the high Kapitza resistance caused by Sb_2O_5 thin films, a 16% decrease in $\varkappa_{lat}$ was achieved even after a few ALD cycles of the coating layer, which is more than that of Al_2O_3, ZnO, and TiO_2 conventional oxide coatings. Despite a slight decline in PF, the considerable decrease in $\varkappa_{tot}$ resulted in a 12% increase in maximum zT values.

The effect of a single kind of oxide layer (ZnO and Al_2O_3) and multilayers ($ZnO/Al_2O_3/ZnO$) on TE properties has been thoroughly investigated in CuNi alloys. To demonstrate the effect of single-kind oxide layers, ultrathin interlayers of oxides (ZnO and Al_2O_3) are uniformly deposited on the phase boundary of CuNi alloys. With the ZnO and Al_2O_3 coating layers, these hierarchical interface modifications contribute to the creation of an energy barrier by the oxide layer, resulting in a significant increase in S. Although there is a small increase in ϱ, the enhanced S for 50 cycles of ZnO-coated samples compensated for the loss and resulted in an ~45% increase in PF compared with the pristine sample. In addition, a sandwich-like multilayer structure ($ZnO/Al_2O_3/ZnO$) was constructed on the powder surface to enhance electrical resistance at the phase boundaries. In the high cycle number coating (> 50 cycles), this multiple-layer coated structure sustained the increased PF while also yielding a significant decline in thermal conductivity. The APT results indicate that there is no obvious layered structure after high-temperature pressing and that the Al ions diffuse into the ZnO layers. In 44 cycles ZnO/11 cycles Al_2O_3/ 44 cycles ZnO multilayer coated samples, a maximum zT of 0.22 was achieved at 673 K. Due to decoupling TE parameters by ALD, the zT value increased 128% when compared to pristine CuNi and is nearly as high as previously reported.

Except for enhancing the TE performance, the ALD coating layers can stabilize the TE properties under a temperature gradient and current. Powder ALD is introduced to accurately control and modify the phase boundaries of Zn_4Sb_3, which could block the migration of Zn ions and enhance the thermal stability. To demonstrate the effectiveness of this strategy, ultrathin interlayers of ZnO after 10–100 cycles are uniformly deposited at the phase boundary of Zn_4Sb_3. With ZnO coating layers, these hierarchical interface modifications contribute to the creation of a barrier for charge carriers and ions by the oxide layer. Although there is little deterioration in electrical conductivity, the $\varkappa_{tot}$ suppression of the ZnO-coated samples after 100 cycles compensated for the loss and resulted in almost the same zT values compared with the pristine sample. Additionally, the ZnO-coated samples after 100 cycles show excellent thermal stability during thermal cycling, indicating an effective blocking effect on Zn ion movement.

Our findings demonstrate that powder ALD-based interface modification could be applied as a general route to decouple the strongly interrelated parameters and stabilize the TE performance, which might also be effective for other TE materials.

7.2 Outlook

To further improve the TE performance of materials and explore the underlying interesting phenomenon induced by powder ALD, the following are the major insights and perspectives derived from our work concerning the progress of interface modification of TE materials:

1. For interface modification, the homogeneous dispersion or coating of a second phase is needed. To ensure a reproducible stoichiometry, it is critical to optimize the coating process to achieve a uniform coating and avoid agglomeration during the fabrication process for TE particles with diameters in the nanometer range.
2. To enable the scattering of low-energy charge carriers, an appropriate interfacial barrier induced by the oxide coating layers is needed, indicating that appropriate oxides should be selected and new oxides should be developed. Furthermore, the barrier height should be properly tuned to maintain or improve mobility, and the work function of the incorporated phase should be close to that of the base material.
3. The metals of the coating layers, such as Cu, Ag, Pt, Sb, Ni, and Co, should be developed for low-σ materials. Metal layers could be used to provide conduction paths in the matrix and enhance the overall electrical conductivities of materials.
4. Semiconductors, such as BiSe, $(Bi, Sb)_2(S, Se, Te)_3$, and (Ge, Sn, Pb)(S, Se, Te), can be employed on the surface of TE particles, which can play a moderate role in manipulating TE properties. However, the solubility of one phase in the other should be carefully investigated. The constituent phases (TE matrix and second phase) should be chemically, environmentally, and thermally stable so that the microstructure is not altered during the synthesis and operation processes.
5. The approach of the blocking effect on Zn_3Sb_4 can also be applied to other unstable materials, such as $Cu_2(S, Se, Te)$, $Ag_2(S, Se, Te)$, Cu_7PSe_6, Ag_9GaSe_6, $Cu_{12}Sb_4S_{13}$ and MgAgSb.

We hope that this powder ALD technique will aid in the design of better and novel TE inorganic materials with enhanced performance via the interface/surface modification technique

Appendix

Appendix A: XRD patterns of Al_2O_3, TiO_2 and ZnO-coated Bi

There was no evidence of bismuth oxides in the XRD patterns of ALD-coated samples, showing that no significant oxidation occurred throughout the milling, coating, and sintering processes.

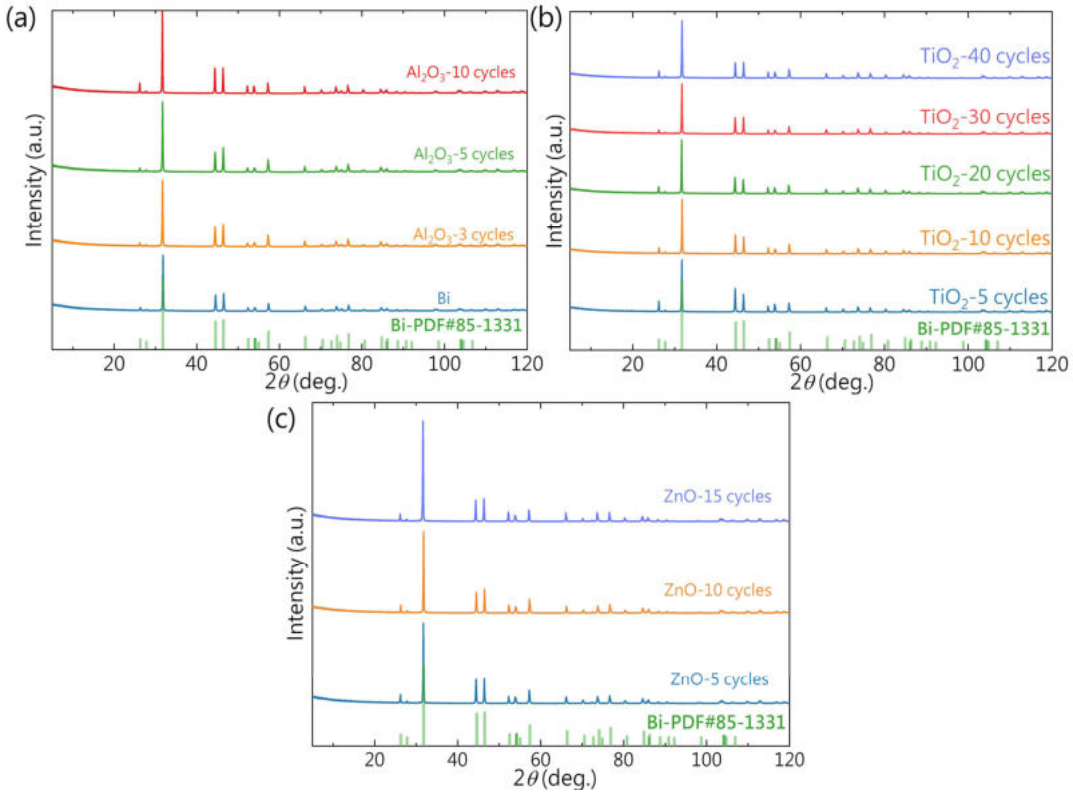

Figure Appendix A *The XRD patterns of (a) Al_2O_3, (b) TiO_2 and (c) ZnO-coated Bi.*

Appendix B: TE properties of Al_2O_3 and ZnO-coated CuNi alloys

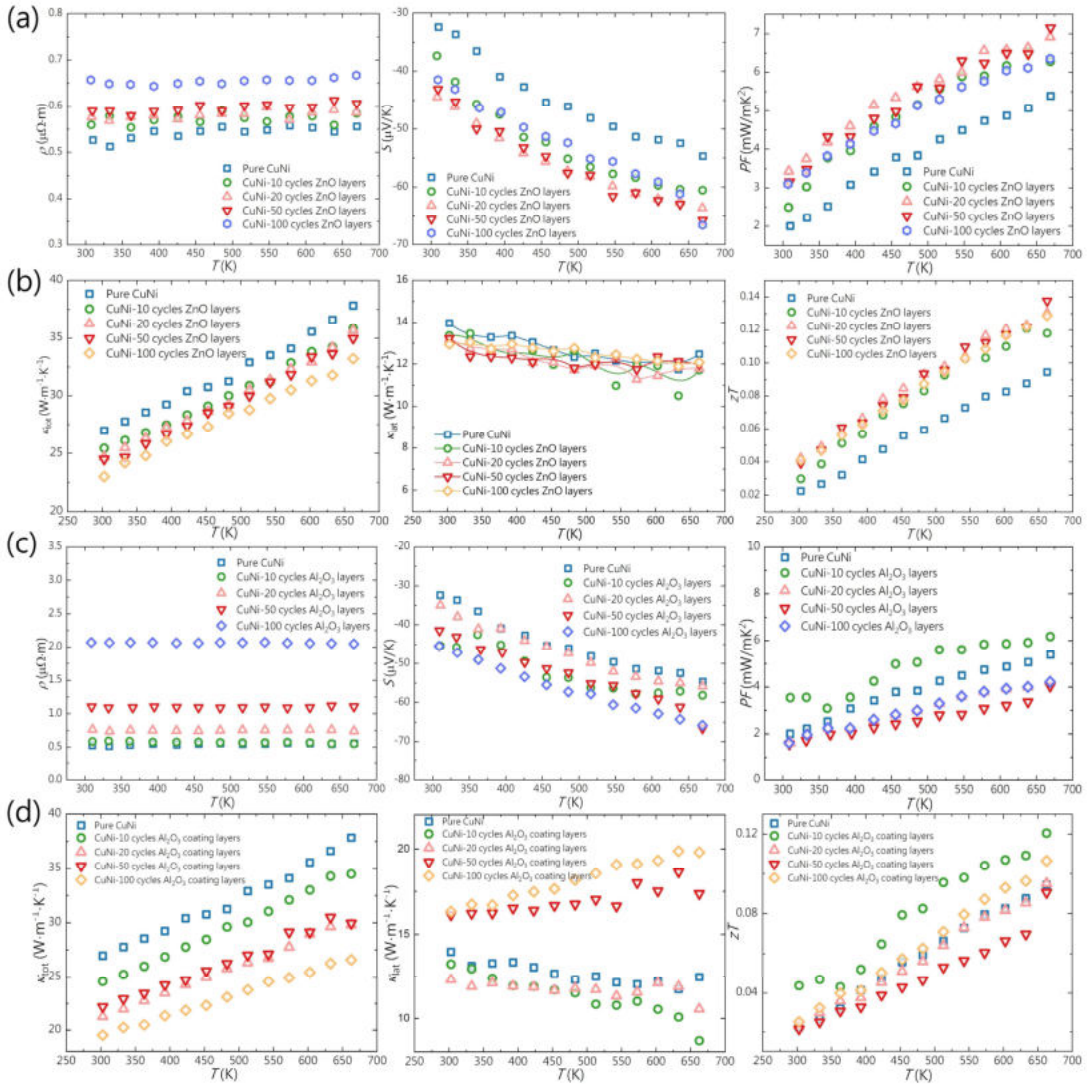

Figure Appendix B *The TE properties of ZnO and Al_2O_3-coated samples with various cycle numbers.*

References

1. Bahrami, A., Schierning, G. & Nielsch, K. Waste Recycling in Thermoelectric Materials. *Adv. Energy Mater.* **10**, 1904159 (2020).

2. Luo, J. *et al.* Progress on High-throughput Synthesis and Characterization Methods for Thermoelectric Materials. *J. Inorg. Mater.* **34**, 247 (2019).

3. Ding, D., Lu, C. & Tang, Z. Bottom Up Chalcogenide Thermoelectric Materials from Solution-Processed Nanostructures. *Adv. Mater. Interfaces* **4**, 1700517 (2017).

4. He, S. *et al.* A General Strategy for High-throughput Experimental Screening of Promising Bulk Thermoelectric Materials. *Sci. China Mater.* **64**, 1751–1760 (2021).

5. Zhu, T., Hu, L., Zhao, X. & He, J. New Insights into Intrinsic Point Defects in V_2VI_3 Thermoelectric Materials. *Adv. Sci.* **3**, 1600004 (2016).

6. Li, J. *et al.* Point Defect Engineering and Machinability in N-type Mg_3Sb_2-based Materials. *Mater. Today Phys.* **15**, 100269 (2020).

7. Hu, L., Zhu, T., Liu, X. & Zhao, X. Point Defect Engineering of High-Performance Bismuth-Telluride-Based Thermoelectric Materials. *Adv. Funct. Mater.* **24**, 5211–5218 (2014).

8. Jian, Z. *et al.* Significant Band Engineering Effect of YbTe for High Performance Thermoelectric PbTe. *J. Mater. Chem. C* **3**, 12410–12417 (2015).

9. Fu, C., Zhu, T., Liu, Y., Xie, H. & Zhao, X. Band Engineering of High performance P-type FeNbSb based half-Heusler Thermoelectric Materials for Figure of Merit zT $>$ 1. *Energy Environ. Sci.* **8**, 216–220 (2015).

10. Pei, Y., Wang, H. & Snyder, G. J. Band Engineering of Thermoelectric Materials. *Adv. Mater.* **24**, 6125–6135 (2012).

11. Jiang, J., Chen, L., Bai, S., Yao, Q. & Wang, Q. Fabrication and Thermoelectric Performance of Textured N-type $Bi_2(Te,Se)_3$ by Spark Plasma Sintering. *Mater. Sci. Eng. B* **117**, 334–338 (2005).

12. Qiu, J. *et al.* 3D Printing of Highly Textured Bulk Thermoelectric Materials: Mechanically Robust BiSbTe Alloys with Superior Performance. *Energy Environ. Sci.* **12**, 3106–3117 (2019).

13. Popuri, S. R. *et al.* Large Thermoelectric Power Factors and Impact of Texturing on the Thermal Conductivity in Polycrystalline SnSe. *J. Mater. Chem. C* **4**, 1685–1691 (2016).

14. Liang, Z., Boland, M. J., Butrouna, K., Strachan, D. R. & Graham, K. R. Increased Power Factors of Organic–inorganic Nanocomposite Thermoelectric Materials and the Role of Energy Filtering. *J. Mater. Chem. A* **5**, 15891–15900 (2017).

15. Soni, A. *et al.* Interface Driven Energy Filtering of Thermoelectric Power in Spark Plasma Sintered $Bi_2Te_{2.7}Se_{0.3}$ Nanoplatelet Composites. *Nano Lett.* **12**, 4305–4310 (2012).

16. Pakdel, A., Guo, Q., Nicolosi, V. & Mori, T. Enhanced Thermoelectric Performance of Bi–Sb–Te/Sb_2O_3 nanocomposites by Energy Filtering Effect. *J. Mater. Chem. A* **6**, 21341–21349 (2018).

17. Lan, Y., Minnich, A. J., Chen, G. & Ren, Z. Enhancement of Thermoelectric Figure-of-Merit by a Bulk Nanostructuring Approach. *Adv. Funct. Mater.* **20**, 357–376 (2010).

18. Bux, S. K. *et al.* Nanostructured Bulk Silicon as an Effective Thermoelectric Material. *Adv. Funct. Mater.* **19**, 2445–2452 (2009).

19. Tan, G. *et al.* High Thermoelectric Performance of P-type SnTe via a Synergistic Band Engineering and Nanostructuring Approach. *J. Am. Chem. Soc.* **136**, 7006–7017 (2014).

20. Liu, H. *et al.* Band and Phonon Engineering for Thermoelectric Enhancements of Rhombohedral GeTe. *ACS Appl. Mater. Interfaces* **11**, 30756–30762 (2019).

21. Wang, H. *et al.* Phonon Engineering for Thermoelectric Enhancement of p-Type Bismuth Telluride by a Hot-Pressing Texture Method. *ACS Appl. Mater. Interfaces* **12**, 31612–31618 (2020).

22. Yoon, J. S. *et al.* High Thermoelectric Performance of Melt-spun $Cu_xBi_{0.5}Sb_{1.5}Te_3$ by Synergetic Effect of Carrier Tuning and Phonon Engineering. *Acta Mater.* **158**, 289–296 (2018).

23. Ahmad, K., Wan, C. & Zong, P. Thermoelectric Properties of BiSbTe/Graphene Nanocomposites. *J. Mater. Sci. Mater. Electron.* **30**, 11923–11930 (2019).

24. Ji, X., He, J., Su, Z., Gothard, N. & Tritt, T. M. Improved Thermoelectric Performance in Polycrystalline P-type Bi_2Te_3 via an Alkali Metal Salt Hydrothermal Nanocoating Treatment Approach. *J. Appl. Phys.* **104**, 034907 (2008).

25. Ibáñez, M. *et al.* Tuning Transport Properties in Thermoelectric Nanocomposites through Inorganic Ligands and Heterostructured Building Blocks. *ACS Nano* **13**, 6572–6580 (2019).

26. Li, W. *et al.* Low Sound Velocity Contributing to the High Thermoelectric Performance of Ag_8SnSe_6. *Adv. Sci.* **3**, 1600196 (2016).

27. Jiang, B. *et al.* Cu_8GeSe_6-based Thermoelectric Materials with an Argyrodite structure. *J. Mater. Chem. C* **5**, 943–952 (2017).

28. Jiang, B. *et al.* An Argyrodite-type Ag_9GaSe_6 Liquid-like Material with Ultralow Thermal Conductivity and High Thermoelectric Performance. *Chem. Commun.* **53**, 11658–11661 (2017).

29. Zhu, T. *et al.* Compromise and Synergy in High-Efficiency Thermoelectric Materials. *Adv. Mater.* **29**, 1605884 (2017).

30. Hu, C., Xia, K., Fu, C., Zhao, X. & Zhu, T. Carrier Grain Boundary Scattering in Thermoelectric Materials. *Energy Environ. Sci.* **15**, 1406–1422 (2022).

31. You, L. *et al.* High Thermoelectric Performance of Cu-Doped PbSe-PbS System Enabled by High-Throughput Experimental Screening. *Research* **2020**, 1–8 (2020).

32. Luo, T. *et al.* Dopant-segregation to Grain Boundaries Controls Electrical Conductivity of N-type NbCo(Pt)Sn half-Heusler Alloy Mediating Thermoelectric Performance. *Acta Mater.* **217**, 117147 (2021).

33. Li, S. *et al.* Highly Distorted Grain Boundary with an Enhanced Carrier/Phonon Segregation Effect Facilitates High-performance Thermoelectric Materials. *ACS Appl. Mater. Interfaces* **13**, 51018–51027 (2021).

34. Li, S. *et al.* Rare Earth Element Doping Introduces Pores to Improve Thermoelectric Properties of P-type $Bi_{0.46}Sb_{1.54}Te_3$. *ACS Appl. Energy Mater.* **4**, 9751–9757 (2021).

35. He, S., Lehmann, S., Bahrami, A. & Nielsch, K. Current State-of-the-art in the Interface/Surface Modification of Thermoelectric Materials. *Adv. Energy Mater.* **11**, 2101877 (2021).

36. Chen, W. Y., Shi, X. L., Zou, J. & Chen, Z. G. Thermoelectric Coolers: Progress, Challenges, and Opportunities. *Small Methods* **6**, 1–21 (2022).

37. Chen, Z., Zhang, X. & Pei, Y. Manipulation of Phonon Transport in Thermoelectrics. *Adv. Mater.* **30**, 1–12 (2018).

38. Weimer, A. W. Particle Atomic Layer Deposition. *J. Nanoparticle Res.* **21**, 9 (2019).

39. Marichy, C., Bechelany, M. & Pinna, N. Atomic Layer Deposition of Nanostructured Materials for Energy and Environmental Applications. *Adv. Mater.* **24**, 1017–1032 (2012).

40. Zhao, X. Y. *et al.* Synthesis of $Yb_yCo_4Sb_{12}/Yb_2O_3$ Composites and Their Thermoelectric Properties. *Appl. Phys. Lett.* **89**, 092121 (2006).

41. Ito, M., Tanaka, T. & Hara, S. Thermoelectric Properties of β-$FeSi_2$ with Electrically Insulating SiO_2 and Conductive TiO Dispersion by Mechanical Alloying. *J. Appl. Phys.* **95**, 6209–6215 (2004).

42. Xie, M. *et al.* Amorphous Ultrathin TiO_2 Atomic Layer Deposition Films on Carbon Nanotubes as Anodes for Lithium Ion Batteries. *J. Electrochem. Soc.* **162**, A974–A981 (2015).

43. Xiong, Z. *et al.* Effects of Nano-TiO_2 Dispersion on the Thermoelectric Properties Offilled-skutterudite $Ba_{0.22}Co_4Sb_{12}$. *Solid State Sci.* **11**, 1612–1616 (2009).

44. Wang, X. Atomic Layer Deposition of Iron, Cobalt, and Nickel Chalcogenides: Progress and Outlook. *Chem. Mater.* **33**, 6251–6268 (2021).

45. Hagen, D. J., Pemble, M. E. & Karppinen, M. Atomic Layer Deposition of Metals: Precursors and Film Growth. *Appl. Phys. Rev.* **6**, 041309 (2019).

46. Kim, Y. *et al.* Atomic-layer-deposition-Based 2D Transition Metal Chalcogenides: Synthesis, Modulation, and Applications. *Adv. Mater.* **2005907**, 2005907 (2021).

47. Shen, C., Yin, Z., Collins, F. & Pinna, N. Atomic Layer Deposition of Metal Oxides and Chalcogenides for High Performance Transistors. *Adv. Sci.* **2104599**, 2104599 (2022).

48. Miikkulainen, V., Leskelä, M., Ritala, M. & Puurunen, R. L. Crystallinity of Inorganic Films Grown by Atomic Layer Deposition: Overview and General trends. *J. Appl. Phys.* **113**, 021301 (2013).

49. Hu, Y., Lu, J. & Feng, H. Surface Modification and Functionalization of Powder Materials by Atomic Layer Deposition: a Review. *RSC Adv.* **11**, 11918–11942 (2021).

50. Oh, I. K., Sandoval, T. E., Liu, T.L., Richey, N. E. & Bent, S. F. Role of Precursor Choice on Area-Selective Atomic Layer Deposition. *Chem. Mater.* **33**, 3926–3935 (2021).

51. He, S. *et al.* Surface Modification of Bismuth by ALD of Antimony Oxide for Suppressing Lattice Thermal Conductivity. *ACS Appl. Energy Mater.* **5**, 4041–4046 (2022).

52. He, S. *et al.* Effect of Powder ALD Interface Modification on the Thermoelectric Performance of Bismuth. *Adv. Mater. Technol.* **2100953**, 2100953 (2021).

53. Lim, S. S. *et al.* Carrier Modulation in Bi_2Te_3-Based Alloys via Interfacial Doping with Atomic Layer Deposition. *Coatings* **10**, 572 (2020).

54. Li, S. *et al.* Effective Atomic Interface Engineering in $Bi_2Te_{2.7}Se_{0.3}$ Thermoelectric Material by Atomic-layer-deposition Approach. *Nano Energy* **49**, 257–266 (2018).

55. Kim, S. *et al.* Effect of ZnO and SnO_2 Nanolayers at Grain Boundaries on Thermoelectric Properties of Polycrystalline Skutterudites. *Nanomaterials* **10**, 2270 (2020).

56. Zhang, Y. *et al.* Zr Vacancy Interfaces: an Effective Strategy for Collaborative Optimization of ZrNiSn-based Thermoelectric Performance. *J. Mater. Chem. A* **7**, 26053–26061 (2019).

57. Li, S. *et al.* Precision Grain Boundary Engineering in Commercial $Bi_2Te_{2.7}Se_{0.3}$ Thermoelectric Materials Towards High Performance. *J. Mater. Chem. A* **9**, 11442–11449 (2021).

58. Shi, X. L., Zou, J. & Chen, Z. G. Advanced Thermoelectric Design: From Materials and Structures to Devices. *Chem. Rev.* **120**, 7399–7515 (2020).

59. Mao, J., Chen, G. & Ren, Z. Thermoelectric Cooling Materials. *Nat. Mater.* **20**, 454–461 (2021).

60. Jia, N. *et al.* Thermoelectric Materials and Transport Physics. *Mater. Today Phys.* **21**, 100519 (2021).

61. He, R., Schierning, G. & Nielsch, K. Thermoelectric Devices: A Review of Devices, Architectures, and Contact Optimization. *Adv. Mater. Technol.* **3**, 1700256 (2018).

62. Jaziri, N. *et al.* A Comprehensive Review of Thermoelectric Generators: Technologies and Common Applications. *Energy Reports* **6**, 264–287 (2020).

63. Carson, J. K., Lovatt, S. J., Tanner, D. J. & Cleland, A. C. Thermal Conductivity Bounds for Isotropic, Porous Materials. *Int. J. Heat Mass Transf.* **48**, 2150–2158 (2005).

64. Chen, Z. G., Shi, X., Zhao, L. D. & Zou, J. High-performance SnSe Thermoelectric Materials: Progress and Future Challenge. *Prog. Mater. Sci.* **97**, 283–346 (2018).

65. Yang, J. *et al.* On the Tuning of Electrical and Thermal Transport in Thermoelectrics: an Integrated Theory–experiment Perspective. *npj Comput. Mater.* **2**, 15015 (2016).

66. Gayner, C. & Amouyal, Y. Energy Filtering of Charge Carriers: Current Trends, Challenges, and Prospects for Thermoelectric Materials. *Adv. Funct. Mater.* **30**, 1901789 (2020).

67. Zaferani, S. H., Ghomashchi, R. & Vashaee, D. Assessment of Thermoelectric, Mechanical, and Microstructural Reinforcement Properties of Graphene-mixed Heterostructures. *ACS Appl. Energy Mater.* **4**, 3573–3583 (2021).

68. Ko, D. K., Kang, Y. & Murray, C. B. Enhanced Thermopower via Carrier Energy Filtering in Solution-processable Pt–Sb_2Te_3 Nanocomposites. *Nano Lett.* **11**, 2841–2844 (2011).

69. Zou, T. H. *et al.* Enhanced Thermoelectric Performance via Carrier Energy Filtering Effect in β-Zn_4Sb_3 alloy bulk embedded with $(Bi_2Te_3)_{0.2}(Sb_2Te_3)_{0.8}$. *J. Appl. Phys.* **115**, 053710 (2014).

70. Lin, Y. *et al.* Expression of Interfacial Seebeck Coefficient Through Grain Boundary Engineering with Multi-layer Graphene Nanoplatelets. *Energy Environ. Sci.* **13**, 4114–4121 (2020).

71. Zhang, A. *et al.* Twin Engineering in Solution-Synthesized Nonstoichiometric Cu_5FeS_4 Icosahedral Nanoparticles for Enhanced Thermoelectric Performance. *Adv. Funct. Mater.* **28**, 1705117 (2018).

72. Ibáñez, M. *et al.* Core–shell Nanoparticles as Building Blocks for the Bottom-

Up Production of Functional Nanocomposites: PbTe–PbS Thermoelectric Properties. *ACS Nano* **7**, 2573–2586 (2013).

73. Scheele, M. *et al.* Synthesis and Thermoelectric Characterization of Bi_2Te_3 Nanoparticles. *Adv. Funct. Mater.* **19**, 3476–3483 (2009).

74. Lauth, J. *et al.* Solution-processed Two-dimensional Ultrathin InSe Nanosheets. *Chem. Mater.* **28**, 1728–1736 (2016).

75. Min, Y. *et al.* Synthesis of Multishell Nanoplates by Consecutive Epitaxial Growth of Bi_2Se_3 and Bi_2Te_3 Nanoplates and Enhanced Thermoelectric Properties. *ACS Nano* **9**, 6843–6853 (2015).

76. Sahu, A. *et al.* Bottom-up Design of de novo Thermoelectric Hybrid Materials Using Chalcogenide Resurfacing. *J. Mater. Chem. A* **5**, 3346–3357 (2017).

77. Xia, J. *et al.* Epitaxy of Layered Orthorhombic SnS-$SnS_xSe_{(1-x)}$ Core-shell Heterostructures with Anisotropic Photoresponse. *Adv. Funct. Mater.* **26**, 4673–4679 (2016).

78. Jin, Q. *et al.* Flexible Layer-structured Bi_2Te_3 Thermoelectric on a Carbon Nanotube Scaffold. *Nat. Mater.* **18**, 62–68 (2019).

79. Wingert, M. C. *et al.* Thermal Conductivity of Ge and Ge–Si Core–shell Nanowires in the Phonon Confinement Regime. *Nano Lett.* **11**, 5507–5513 (2011).

80. Zhuge, F. *et al.* Modulation of Thermoelectric Power Factor via Radial Dopant Inhomogeneity in B-doped Si Nanowires. *J. Am. Chem. Soc.* **136**, 14100–14106 (2014).

81. Mattox, D. M. Vacuum Evaporation and Vacuum Deposition. Handbook of Physical Vapor Deposition (PVD) Processing 195–235 (Elsevier, 2010).

82. Baptista, A., Silva, F., Porteiro, J., Míguez, J. & Pinto, G. Sputtering Physical Vapour Deposition (PVD) Coatings: A Critical Review on Process Improvement and Market Trend Demands. *Coatings* **8**, 402 (2018).

83. Qi, Y., Wang, Z., Zhang, M., Yang, F. & Wang, X. Thermoelectric Devices Based on One-dimensional Nanostructures. *J. Mater. Chem. A* **1**, 6110 (2013).

84. DeCoster, M. E. *et al.* Thermal Conductivity and Phonon Scattering Processes of ALD Grown PbTe–PbSe Thermoelectric Thin Films. *Adv. Funct. Mater.* **29**, 1904073 (2019).

85. Chen, J. *et al.* Enhanced Thermoelectric Efficiency in Topological Insulator Bi_2Te_3 Nanoplates via Atomic Layer Deposition-based Surface Passivation. *Appl. Phys. Lett.* **113**, 083904 (2018).

86. Adhikari, S., Selvaraj, S. & Kim, D. H. Progress in Powder Coating Technology Using Atomic Layer Deposition. *Adv. Mater. Interfaces* **5**, 1800581 (2018).

87. Li, S., Zhu, W., Xiao, Y. & Pan, F. Improving the Performance of Thermoelectric Materials by Atomic Layer Deposition-based Grain Boundary Engineering.

Chinese J. Struct. Chem. **39**, 831–837 (2020).

88. Kim, K. C. *et al.* Precision Interface Engineering of an Atomic Layer in Bulk Bi_2Te_3 Alloys for High Thermoelectric Performance. *ACS Nano* **13**, 7146–7154 (2019).

89. Li, S. *et al.* Atomic-scale Tuning of Oxygen-doped $Bi_2Te_{2.7}Se_{0.3}$ to Simultaneously Enhance the Seebeck coefficient and Electrical Conductivity. *Nanoscale* **12**, 1580–1588 (2020).

90. García-García, S. *et al.* Ligand-induced Reduction Concerted with Coating by Atomic Layer Deposition on the Example of TiO_2-coated Magnetite Nanoparticles. *Chem. Sci.* **10**, 2171–2178 (2019).

91. Yamamoto, A., Obara, H. & Ueno, K. Optimization of Thermoelectric Properties of Ni-Cu Based Alloy Through Combinatorial Approach. *Mater. Res. Soc. Symp. Proc.* **1044**, 273–278 (2008).

92. Kang, H. *et al.* Preparing Bulk Cu-Ni-Mn Based Thermoelectric Alloys and Synergistically Improving their Thermoelectric and Mechanical Properties Using Nanotwins and Nanoprecipitates. *Mater. Today Phys.* **17**, 100332 (2021).

93. Yuan, M., Sun, L., Lu, X. W., Jiang, P. & Bao, X. H. Enhancing the Thermoelectric Performance of Cu–Ni Alloys by Introducing Carbon Nanotubes. *Mater. Today Phys.* **16**, 100311 (2021).

94. Guo, K. *et al.* Minimizing Thermal Conductivity for Boosting Thermoelectric Properties of Cu–Ni-Based Alloys through All-Scale Hierarchical Architectures. *ACS Appl. Energy Mater.* **4**, 5015–5023 (2021).

95. Zou, T., Xie, W., Feng, J., Qin, X. & Weidenkaff, A. Recent Developments in β -Zn_4Sb_3 Based Thermoelectric Compounds. *J. Nanomater.* **2015**, 1–15 (2015).

96. Fischer, K. F. F., Bjerg, J. H., Jørgensen, L. R. & Iversen, B. B. Stability and Thermoelectric Properties of Zn_4Sb_3 with TiO_2 Nanoparticle Inclusions. *ACS Appl. Mater. Interfaces* **13**, 45708–45716 (2021).

97. Hung, L. T. *et al.* In Operando Study of High-Performance Thermoelectric Materials for Power Generation: A Case Study of β-Zn_4Sb_3. *Adv. Electron. Mater.* **3**, 1700223 (2017).

98. Song, L., Blichfeld, A. B., Zhang, J., Kasai, H. & Iversen, B. B. Enhanced thermoelectric Performance and High-temperature Thermal Stability of P-type Ag-doped β-Zn_4Sb_3. *J. Mater. Chem. A* **6**, 4079–4087 (2018).

99. Wang, S. Y. *et al.* Enhanced Thermoelectric Performance and Thermal Stability in β-Zn_4Sb_3 by Slight Pb-Doping. *J. Electron. Mater.* **41**, 1091–1099 (2012).

100. Thorup, P. S., Zeuthen, C. M., Borup, K. A. & Iversen, B. B. Improving the Operational Stability of Thermoelectric Zn_4Sb_3 by Segmentation. *Chem. Mater.* **34**, 5206–5214 (2022).

101. Tang, D. *et al.* Preparation and Properties of $Zn_4Sb_{2.94}In_{0.06}$/ZnO Composite

Thermoelectric Materials. *J. Electron. Mater.* **44**, 1902–1908 (2015).

102. Zou, T. H. *et al.* Simultaneous Enhancement in Thermoelectric Power Factor and Phonon Blocking in Hierarchical Nanostructured β-Zn_4Sb_3-Cu_3SbSe_4. *Appl. Phys. Lett.* **104**, 013904 (2014).

103. Tak, J. Y. *et al.* Significantly Enhanced Chemical Stability in Interface-controlled $Cu_{2+x}Se$-reduced Graphene Oxide Composites and Related Thermoelectric Performances. *J. Eur. Ceram. Soc.* **41**, 459–465 (2021).

104. Hosseinzadegan, S., Nischkauer, W., Bica, K. & Limbeck, A. FI-ICP-OES Determination of Pb in Drinking Water After Pre-concentration Using Magnetic Nanoparticles Coated with Ionic Liquid. *Microchem. J.* **146**, 339–344 (2019).

105. Kelly, T. F. & Miller, M. K. Atom Probe Tomography. *Rev. Sci. Instrum.* **78**, 031101 (2007).

106. Borup, K. A. *et al.* Measuring Thermoelectric Transport Properties of Materials. *Energy Environ. Sci.* **8**, 423–435 (2015).

107. Simeone, D., Baldinozzi, G., Gosset, D., Le Caer, S. & Bérar, J. F. Grazing Incidence X-ray Diffraction for the Study of Polycrystalline Layers. *Thin Solid Films* **530**, 9–13 (2013).

108. Greczynski, G. & Hultman, L. X-ray Photoelectron Spectroscopy: Towards Reliable Binding Energy Referencing. *Prog. Mater. Sci.* **107**, 100591 (2020).

109. Puneet, P. *et al.* Enhancement of Thermoelectric Performance of Ball-Milled Bismuth Due to Spark-plasma-sintering-induced Interface Modifications. *Adv. Mater.* **25**, 1033–1037 (2013).

110. Lenoir, B., Cassart, M., Michenaud, J. P., Scherrer, H. & Scherrer, S. Transport properties of Bi-rich Bi-Sb alloys. *J. Phys. Chem. Solids* **57**, 89–99 (1996).

111. Gallo, C. F., Chandrasekhar, B. S. & Sutter, P. H. Transport Properties of Bismuth Single Crystals. *J. Appl. Phys.* **34**, 144–152 (1963).

112. Ibrahim, A. M. & Thompson, D. A. Thermoelectric Properties of BiSb Alloys. *Mater. Chem. Phys.* **12**, 29–36 (1985).

113. Lenoir, B., Dauscher, A., Cassart, M., Ravich, Y. I. & Scherrer, H. Effect of Antimony Content on the Thermoelectric Figure of Merit of $Bi_{1-x}Sb_x$ Alloys. *J. Phys. Chem. Solids* **59**, 129–134 (1998).

114. Bradley, C. C. The Experimental Determination of the Thermoelectric Power in Liquid Metals and Alloys. *Philos. Mag.* **7**, 1337–1347 (1962).

115. Blatt, F. J., Schroeder, P. A., Foiles, C. L. & Greig, D. Thermoelectric Power of Metals. Thermoelectric Power of Metals (Springer US, 1976).

116. O. Madelung, U. Rössler, M. Schulz Non-Tetrahedrally Bonded Elements and Binary Compounds I. Non-Tetrahedrally Bonded Elements and Binary Compounds I vol. 41C (Springer-Verlag, 1998).

117. Mahan, G., Sales, B. & Sharp, J. Thermoelectric Materials: New Approaches to an Old Problem. *Phys. Today* **50**, 42–47 (1997).

118. Sussardi, A., Tanaka, T., Khan, A. U., Schlapbach, L. & Mori, T. Enhanced Thermoelectric Properties of Samarium Boride. *J. Mater.* **1**, 196–204 (2015).

119. Xu, Q. *et al.* Thermoelectric Properties of Phosphorus-doped Van Der Waals crystal Ta_4SiTe_4. *Mater. Today Phys.* **19**, 100417 (2021).

120. Min, B. D., Lee, J. S. & Kim, S. S. Al_2O_3 Nano-coating by Atomic Layer Deposition. *Trans. Electr. Electron. Mater.* **4**, 15–18 (2003).

121. Aarik, J., Aidla, A., Mändar, H. & Uustare, T. Atomic Layer Deposition of Titanium Dioxide from $TiCl_4$ and H_2O: Investigation of Growth Mechanism. *Appl. Surf. Sci.* **172**, 148–158 (2001).

122. Elam, J. W. & George, S. M. Growth of ZnO/Al_2O_3 Alloy Films Using Atomic Layer Deposition Techniques. *Chem. Mater.* **15**, 1020–1028 (2003).

123. Kim, S. K., Hoffmann-Eifert, S., Reiners, M. & Waser, R. Relation Between Enhancement in Growth and Thickness-Dependent Crystallization in ALD TiO_2 Thin Films. *J. Electrochem. Soc.* **158**, D6 (2011).

124. Malm, J., Sahramo, E., Perälä, J., Sajavaara, T. & Karppinen, M. Low-temperature Atomic Layer Deposition of ZnO Thin Films: Control of Crystallinity and Orientation. *Thin Solid Films* **519**, 5319–5322 (2011).

125. Water, W. & Chu, S.Y. Physical and Structural Properties of ZnO Sputtered films. *Mater. Lett.* **55**, 67–72 (2002).

126. Hanada, T., Soga, N. & Ohkawa, M. Thermal Expansion and Coordination State of Cations in Amorphous Films in the System Al_2O_3-TiO_2. *J. Non. Cryst. Solids* **88**, 236–241 (1986).

127. Cave, E. F. & Holroyd, L. V. Thermal Expansion Coefficients of Bismuth. *J. Appl. Phys.* **31**, 1357–1358 (1960).

128. Arisaka, T., Otsuka, M., Tokitani, M. & Hasegawa, Y. Temperature Dependence of Carrier Scattering in Polycrystalline Bismuth. *J. Appl. Phys.* **126**, 085101 (2019).

129. Lenoir, B. *et al.* Bi-Sb alloys: an update. in *Fifteenth International Conference on Thermoelectrics. Proceedings ICT '96* 1–13 (IEEE, 1996).

130. de Boor, J. *et al.* Microstructural Effects on Thermoelectric Efficiency: A case Study on Magnesium Silicide. *Acta Mater.* **77**, 68–75 (2014).

131. Imasato, K. *et al.* Metallic N-type Mg_3Sb_2 Single Crystals Demonstrate the Absence of Ionized Impurity Scattering and Enhanced Thermoelectric Performance. *Adv. Mater.* **32**, 1908218 (2020).

132. Kuo, J. J. *et al.* Grain Boundary Dominated Charge Transport in Mg_3Sb_2-based Compounds. *Energy Environ. Sci.* **11**, 429–434 (2018).

133. Yang, R. Bin *et al.* Atomic Layer Deposition of Antimony Oxide and Antimony sulfide. *Chem. Mater.* **21**, 2586–2588 (2009).

134. Viirola, H. & Niinistö, L. Controlled Growth of Antimony-doped Tin Dioxide thin Films by Atomic Layer Epitaxy. *Thin Solid Films* **251**, 127–135 (1994).

135. Martin-Lopez, R. *et al.* Thermoelectric Properties of Mechanically Alloyed Bi-Sb Alloys. *Appl. Phys. A Mater. Sci. Process.* **68**, 597–602 (1999).

136. Yim, W. M. & Amith, A. Bi-Sb Alloys for Magneto-thermoelectric and Thermomagnetic Cooling. *Solid. State. Electron.* **15**, 1141–1165 (1972).

137. Grabov, V. M., Uryupin, O. N. & Komarov, V. A. Thermoelectric Properties of Polycrystalline Bismuth and Bismuth-antimony Alloys. in *Seventeenth International Conference on Thermoelectrics. Proceedings ICT98,* 138–140 (IEEE, 1998).

138. Martin-Lopez, R. *et al.* Bi-Sb Semiconductor Alloy Synthesized by Mechanical Alloying. *Scr. Mater.* **37**, 219–226 (1997).

139. Kitagawa, H., Noguchi, H., Kiyabu, T., Itoh, M. & Noda, Y. Thermoelectric properties of Bi–Sb Semiconducting Alloys Prepared by Quenching and Annealing. *J. Phys. Chem. Solids* **65**, 1223–1227 (2004).

140. Li, S. *et al.* Optimized Hetero-interfaces by Tuning 2D SnS_2 Thickness in $Bi_2Te_{2.7}Se_{0.3}/SnS_2$ Nanocomposites to Enhance Thermoelectric Performance. *Nano Energy* **39**, 297–305 (2017).

141. Felizco, J. *et al.* Enhanced Thermoelectric Transport and Stability in Atomic Layer Deposited-HfO_2/ZnO and TiO_2/ZnO-sandwiched Multilayer Thin Films. *ACS Appl. Mater. Interfaces* **12**, 49210–49218 (2020).

142. Banerjee, P., Lee, W. J., Bae, K. R., Lee, S. B. & Rubloff, G. W. Structural, Electrical, and Optical Properties of Atomic Layer Deposition Al-doped ZnO films. *J. Appl. Phys.* **108**, 043504 (2010).

143. Mao, J. *et al.* High Thermoelectric Power Factor in Cu-Ni Alloy Originate from Potential Barrier Scattering of Twin Boundaries. *Nano Energy* **17**, 279–289 (2015).

144. Jakschik, S. *et al.* Crystallization Behavior of Thin ALD-Al_2O_3 Films. *Thin Solid Films* **425**, 216–220 (2003).

Abbreviations and symbols

TE	Thermoelectric
ALD	Atomic layer deposition
SWCNT	Single-wall carbon nanotube
GPC	Growth per cycle
TMA	Trimethylaluminum
DEZ	Diethylzinc
rpm	Revolutions per minute
EDX	Energy dispersive X-ray
SEM	Scanning electron microscopy
SPS	Spark plasma sintering
TMA	Trimethylaluminum
DEZ	Diethylzinc
ICP–OES	Inductively coupled plasma-optical emission spectrometry
XRD	X-ray powder diffraction
HAADF-STEM	High-angle annular dark-field scanning transmission electron microscopy
APT	Atom Probe Tomography
XRR	X-ray reflectivity
XPS	X-ray photoelectron spectroscopy
GIXRD	Grazing Incidence X-ray Diffraction
CTE	Coefficients of thermal expansion
SPB	Single parabolic band
ϱ	Resistivity
S	Seebeck coefficient
PF	Power factor
$\varkappa_{\mathrm{tot}}$	Total thermal conductivity
$\varkappa_{\mathrm{ele}}$	Electronic thermal conductivity
$\varkappa_{\mathrm{lat}}$	Lattice thermal conductivity
zT	Figure of merit
n	Carrier concentration
μ_{H}	Hall mobility
L	Lorenz number
λ	Thermal diffusivity
C_{p}	Heat capacity
D	Density
R_{K}	Kapitza resistance
m^*	Effective mass
wt %	Weight percentage
C_{layer}	Cycle numbers

m_{layer}	Mass of coating layers
m_{CuNi}	Mass of one particle of CuNi
ϱ_{layer}	Density of coating layers
ϱ_{CuNi}	Density of CuNi
x_{layer}	Thickness of coating layers

Acknowledgments

I would like to express my deepest gratitude to Prof. Dr. Kornelius Nielsch for his invaluable guidance, unwavering support, and mentorship throughout the entire research process.

I extend my appreciation to my colleagues and friends (Dr. Amin Bahrami, Dr. Sebastian Lehmann, Dr. Ran He, Jun Yang, Dongho Shin, Irene G., and Jun Li) for their stimulating discussions and collaborative spirit.

I am indebted to my father, my mother and Ruitao for their supporting, encouragement, and belief in my abilities. Their unwavering support has been my pillar of strength.

In addition, I want to thank:

- Dr. Sebastian Lehmann and Mrs. Christiane Kranz for their technical support and maintenance of ALD devices.
- Dr. Chanwon Jung and Dr. Siyuan Zhang at Max-Planck-Institut für Eisenforschung for the help of APT and TEM characterizations.
- Dr. Lars Giebeler for the XRD refinement and the useful discussions of the XRD results.
- Mrs. Andrea Voβ for the ICP measurements.
- Dr. Martin Hantusch and Ms. Sandra Schiemenz for XPS and Raman measurements.
- Prof. Zhifeng Ren at the University of Houston for fruitful discussions.

I also thank the Program of Collaborative Research Centers in Germany (Grant No. SFB 1415), the European Union's Horizon 2020 Research and Innovation Program under grant agreement No 958174, and Deutsche Forschungsgemeinschaft DFG (Project No SCHU1069/25-1).

List of publications

i) Publications related to the Thesis

1. ***Shiyang He***, Sebastian Lehmann, Amin Bahrami*, Kornelius Nielsch*. Current State-of-the-art in the Interface/surface Modification of Thermoelectric Materials (2021). ***Advanced Energy Materials***, 11(37), 2101877.

2. ***Shiyang He***, Amin Bahrami*, Xiang Zhang, Ignacio González Martínez, Sebastian Lehmann, Kornelius Nielsch* (2022). Effect of Powder ALD Interface Modification on the Thermoelectric Performance of Bismuth. ***Advanced Materials Technologies***, 7(5), 2100953.

3. ***Shiyang He***, Jun Yang, Amin Bahrami*, Xiang Zhang, Ran He, Martin Hantusch, Sebastian Lehmann, and Kornelius Nielsch* (2022). Surface Modification of Bismuth by ALD of Antimony Oxide for Suppressing Lattice Thermal Conductivity. ***ACS Applied Energy Materials***, 5(4), 4041-4046.

4. ***Shiyang He***, Amin Bahrami*, Chanwon Jung, Xiang Zhang, Ran He, Zhifeng Ren, Siyuan Zhang, Kornelius Nielsch* (2023), Precision Interface Engineering of CuNi Alloys by Powder ALD Toward High Thermoelectric Performance. ***Advanced Functional Materials*** **(*Under reviewed*)**

5. ***Shiyang He***, Amin Bahrami*, Chanwon Jung, Xiang Zhang, Ran He, Siyuan Zhang, Kornelius Nielsch* (2023), Blocking the Ion Immigration in Zn_4Sb_3 with Oxide Coating by Powder ALD. **(*Under preparation*)**

ii) Publications related to other research during Ph.D. study

6. ***Shiyang He***, Amin Bahrami*, Pingjun Ying, Lars Giebeler, Xiang Zhang, Kornelius Nielsch and Ran He* (2022). Improving the Thermoelectric Performance of ZrNi (In, Sb)-based Double half-Heusler Compounds. ***Journal of Materials Chemistry A***, 10(25), 13476-13483.

7. ***Shiyang He***, Amin Bahrami*, Xiang Zhang, Magdalena Ola Cichocka, Jun Yang, Jaroslav Charvot, Filip Bureš, Alla Heckel, Stephan Schulz, Kornelius Nielsch* (2023). Atomic Layer Deposition and Characterization of Bi_1Se_1 Thin Films, ***Journal of the European Ceramic Society***, 43(11), 4808-4813.

8. ***Shiyang He***, Amin Bahrami*, Xiang Zhang, Jaakko Julin, Mikko Laitinen, Kornelius Nielsch* (2023). Low-temperature ALD of Highly Conductive Antimony Films Through the Reaction of Silylamide with Alkoxide and Alkylamide Precursors (2023). ***Materials Today Chemistry,*** 32, 101650.

iii) Publications originated from collaborations during Ph.D. study

9. Jun Yang, Amin Bahrami*, Xingwei Ding, Sebastian Lehmann, Nadine Kruse, ***Shiyang He***, Bowen Wang, Martin Hantusch, Kornelius Nielsch* (2022). Characteristics of ALD-ZnO Thin Film Transistor Using H_2O and H_2O_2 as Oxygen Sources. ***Advanced Materials Interfaces***, 9(15), 2101953.

10. Jun Yang, Amin Bahrami*, Xingwei Ding, Panpan Zhao, ***Shiyang He***,

Sebastian Lehmann, Mikko Laitinen, Jaakko Julin, Mikko Kivekäs, Timo Sajavaara, Kornelius Nielsch* (2022). Low-temperature Atomic Layer Deposition of High-k SbO_x for Thin Film Transistors. ***Advanced Electronic Materials***, 8(7), 2101334.

11. Sebastian Lehmann, Fanny Mitzscherling, ***Shiyang He***, Jun Yang, Martin Hantusch, Kornelius Nielsch, Amin Bahrami* (2023). Water-free SbO_x ALD Process for Coating Bi_2Te_3 Particles. ***Coatings***, 13(3), 641.

iv) Publications related to other TE research during M.Sc study

12. ***Shiyang He***, Yongbo Li, Lu Liu, Ying Jiang, Jing Feng, Wei Zhu, Jiye Zhang, Zirui Dong, Yuan Deng, Jun Luo*, Wenqing Zhang*, Gang Chen* (2020). Semiconductor Glass with Superior Flexibility and High Room Temperature Thermoelectric Performance. ***Science Advances***, 6, eaaz8423.

13. ***Shiyang He***, Yang Yang, Zhili Li, Jiye Zhang, Chenyang Wang, Wenqing Zhang, J. Luo* (2021). A General Strategy for High-throughput Experimental Screening of Promising Bulk Thermoelectric Materials. ***Science China Materials***, 64, 1751–1760.

List of awards

- **Nachwuchspreis der DTG 2023,** October 28, 2023, Deutsche Thermoelektrik-Gesellschaft e.V.
- **ITS Graduate Student Awards 2022,** October 28, 2022, International Thermoelectric Society.
- **The Best Oral Presentation Award,** Symposium EQ01 Progress in Thermoelectrics - From Traditional to Novel Materials，MRS Fall 2022, Boston, November 27–December 2, 2022, Materials Research Society USA.

List of attending conferences

1. ALPIN Kick Off & Workshop 2021, Dresden, Germany, September 21–22, 2021 **(Poster presentation)**

2. Virtual Conference on Thermoelectrics 2021, Online, July 20–22, 2021 **(Oral presentation)**

3. AVS 21st International Conference on Atomic Layer Deposition, Online, June 27–30, 2021 **(Poster presentation)**

4. ALD for Industry 2022, Dresden, Germany March 29–30, 2022

5. AVS 22nd International Conference on Atomic Layer Deposition, Gent, Belgium, June 27–30, 2022 **(Poster presentation)**

6. Virtual Conference on Thermoelectrics 2022, Online, July 20–22, 2022 **(Oral presentation)**

7. ALPIN Kick Off & Workshop 2022, Duisburg, Germany, September 12–13, 2022 **(Poster presentation)**

8. Materials Science and Engineering Congress 2022, Darmstadt, Germany, September 27–29, 2022 **(Oral presentation)**

9. MRS Fall Meeting 2022, Boston, USA, November 27–December 2, 2022 **(Oral presentation)**